The role of control network in the accuracy of underground laser scanning surveys

Christopher Page

A thesis submitted for the degree of Master of Surveying

School of Surveying/Te Kura Kaikuri

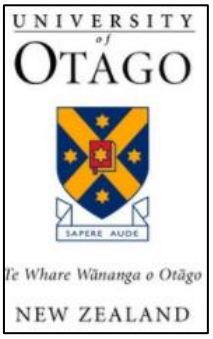

University of Otago/ Te Whare Wānanga o Otāgo

June 2017

Abstract

Terrestrial laser scanning is used in various fields with numerous applications, one being the documentation of heritage sites. Often scans will be georeferenced with respect to a real-world coordinate system. This is done using either direct or indirect georeferencing techniques. The indirect georeferencing method was used in this research, which uses coordinated targets, referred to as Ground Control Points (GCPs), that are captured in the scan scene. Manufacturers suggest a minimum of three GCPs are used, should the z-axis not be vertical, with additional GCPs for redundancy. Ideally GCPs should be placed evenly around the extent of the scan scene. For heritage site documentation, this is not always feasible given the unique and complex nature of each site. This research investigates the quantity and spatial variability of GCPs used in a scan scene, and the subsequent effect on the point cloud accuracy. A control test network was established at the School of Surveying (SoS), where variations of GCP scenarios were investigated, which was then applied to a case study in Arras, France. The case study being a network of underground World War One tunnels that were excavated by the New Zealand Engineering Tunnelling Company (NZETC), known as the Ronville Tunnels. The results from the SoS test network show, in this particular instance, that there is little benefit in using additional GCPs in a scan scene, should the minimum (three) be placed evenly around the extent of the area being captured. Low redundancy solutions may reduce the accuracy and robustness of georeferencing solutions, as seen with the case where large errors were present where the minimum number of GCPs were used. Geometrically poor placement of GCPs shows an increased correlation between the check points root mean square errors and range from the GCP centroid. The case study results, where the scan scene extents were hundreds of metres long, showed that it is necessary to supplement the minimum number of GCPs to mitigate uncertainties in the point cloud dataset. Similar to a least squares estimation adjustment where there are less fixed stations, there is more uncertainty for an unknown position. GCPs should therefore, be placed spatially around the extents of the scan scene and where scan scene extents increase so should the number of GCPs.

Acknowledgements

Many thanks must be given to the following people, without whom this research would not have been possible.

Pascal Sirguey, thank you for your continuous support throughout this research. Having started in 2015, the project and the research has had some challenges along the way, however, there have been countless more rewards. Thank you for involving me in such a historic project.

I must thank Richard Hemi, who allowed me such freedom with all the laser scanning fieldwork. The research and project would not have been possible without you and I am grateful for all the experiences shared along this journey.

The New Zealand Institute of Surveyors and the School of Surveying graciously provided financial support while the research was undertaken. I am incredibly grateful for all the support provided by both institutes.

My colleagues at ESGT in France, Damien Houvet, Ghyslain Ferré, Christophe Charlet, and Elisabeth Simonetto, thank you for all the help and support provided during the fieldwork in France. I am deeply thankful and believe that the project would not have been as enriching without all your hard work.

Lastly, thank you to my family for their everlasting support and love.

Table of Contents

List of Figures

List of Tables

Chapter 1 Introduction

1.1 Background

Terrestrial Laser Scanning (TLS) can produce precise point cloud data for a given surface at up to one million points per second. Each point that makes up the point cloud has X, Y, and Z coordinates and an intensity value, which may be supplemented with an RGB value via internal or external camera imagery. The precision, density, and speed of data capture means TLS is recognised in a wide range of industries and has numerous applications. TLS is applied to medicine, where it has been used for reconstructive surgery applications (O'Grady and Antonyshyn, 1999); forestry as a quantitative measurement system for tree analysis (Watt and Donoghue, 2005); evaluating rock mass stability in underground tunnels (Fekete and Diederichs, 2013); as well as documentation and management planning of heritage sites (Geymen, 2009). The collected 3-dimensional (3D) data generated is coordinated in a local coordinate system relative to the instrument, known as the Intrinsic Reference System (IRS). In the case of multi-station scanning, a registration phase is required whereby all scans are coordinated relative to a single scan, treated as the "reference scan" (Scaioni, 2012). This process involves the assembly of scans based on common points used to establish a rigid body transformation (RBT) between each overlapping scan (Figure 1.1). The IRS can then be transformed to a Ground Reference System (GRS) suitable to the area being surveyed (Alba and Scaioni, 2007; Argüelles-Fraga *et al.*, 2013). Transforming the IRS into the GRS is what is known as georeferencing (Figure 2.11).

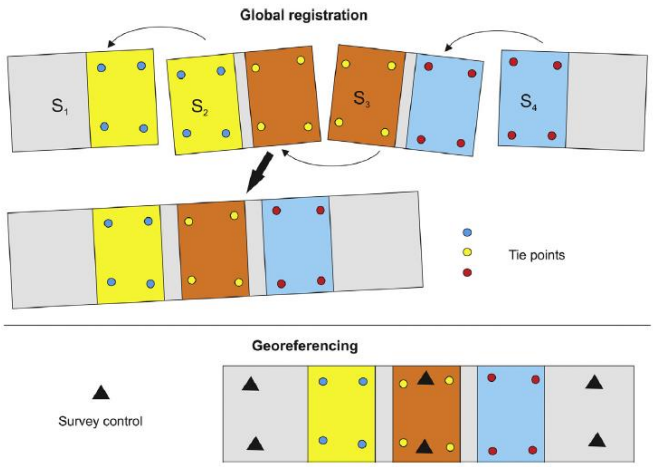

Figure 1.1.The assembly of scans, showing RBT of individual scans using tie points (top and middle) and the final RBT into a georeferenced network using survey control points (bottom). S_1, S_2, S_{n+1} represent each subsequent scan. Tie points are common features in each subsequent scan that are used to register scans together. Tie points can consist of artificial targets or existing surface features of structures. Source: Pejic, 2013.

TLS does allow for precise (millimetre-level) point data to be acquired, however, the accuracy of the data is influenced by the technique used to register and georeference the point cloud. Noted techniques are the direct, indirect, and arbitrary georeferencing methods. The direct georeferencing technique requires the scanner to be positioned over a mark with known coordinates and height. Orientating the scanner is performed with respect to another known mark (Paffenholz *et al.*, 2010). This is a similar procedure to that which is used to orientate and coordinate positions using a total station. The indirect georeferencing approach uses post processing to reconstruct the scanner positions and point clouds using control points. The arbitrary method of georeferencing is a combination of both above-mentioned techniques (Pejic, 2013). Each of these georeferencing techniques are discussed in the Chapter 2.

A heritage site project, termed LiDARRAS, was undertaken in the town of Arras, France. The LiDARRAS case study was a project that looked at accurately documenting, in 3D, a substantial network of underground tunnels. The tunnels were excavated by the New Zealand Engineering Tunnelling Company (NZETC) during the First World War and highlights the significant contribution made by New Zealand during the War. With the tunnels deteriorating over decades and being previously unmapped in 3D, this project was a noteworthy opportunity to record a key piece of New Zealand's history using TLS.

1.2 Rationale for the research and merit

In this thesis scan registration and subsequent georeferencing involve different surveying scenarios:

1. A network of common targets (e.g., spheres and/or checkboard patterns) are placed throughout the scan scene with at least three common targets in each overlapping scan supporting RBTs between subsequent scans. The georeferencing is obtained via Least Square Estimation (LSE) adjustment of the final point cloud RBT parameters using targets of known coordinates in the GRS. Traditional surveying techniques involving Global Navigation Satellite System (GNSS) and Total Station (TS), supports the centimetre-level accuracy coordinates of such targets. Additional target coordinates in the GRS can however support redundancies and a LSE adjustment allowing errors to be more evenly distributed.
2. All scans are registered using surface to surface algorithms (no common targets) and the final point cloud is georeferenced based on a reduced network of Ground Control Points (GCPs).

These scenarios will result in contrasting error budget/propagation, as well as different cost and time commitment. Manufacturers provide general guidelines to setting up and conducting TLS surveys, however, no specific quantification of errors associated with the different methodologies have been conducted. "*To reduce the georeferencing/registration error, targets should be arranged in such a way that they can cover the full volume of a scan scene'* (Fan *et al*., 2015). There is little existing research that quantifies this statement and states, more specifically, how many targets should be used and what the consequences will be on the accuracy of the point cloud. This is particularly important when time is a limiting factor and there are no opportunities to revisit a site to record more data (Theiler, 2015; Becerik-Gerber *et al*., 2011). In the case of heritage site documentation, there is often a single opportunity to capture the entire scan scene. Hence, to maximise TLS data capture time, a control network of GCPs should be established efficiently, minimising time and maximising accuracy. Given the unique nature of each heritage site (size, shape, condition etc.) it is not always possible to place GCPs throughout the site. This research aims to contribute to this gap in the literature and present an evaluation of varying georeferencing scenarios and apply the results to the LiDARRAS case study.

1.3 Research objectives

This research focuses on the indirect georeferencing method, which uses artificial targets in the scan scene to georeference point cloud data. To the best of our knowledge, there is no literature at present that defines possible outcomes for which unfavourable spatial distribution or quantity of GCPs used affects the accuracy of point cloud data. This thesis evaluates varying GCP scenarios and their effects on the point cloud accuracy. This will be applied to the LiDARRAS case study in the north of France, whereby a significant heritage site was subject to such survey. The time available for data capture in France was limited, making it imperative that correct methodologies be implemented from the outset to make use of the time available for TLS data capture. Therefore, this research aims to quantitatively characterize TLS scenarios on the error being committed based on the choice of methodology implemented, the overarching research question of this study being:

What is the effect of the quantity and spatial variability of GCPs used on the accuracy of TLS surveys?

It is hypothesised that similarly to a constrained LSE adjustment, the ensuing result be more precise with an increased number of fixed stations (Ghilani, 2010). Other goals include:

1. Establishing a TLS documentation framework by which future heritage sites can be modelled and applying it to the LiDARRAS case study.
2. Providing quantitative analysis of point cloud data based on varying GCP scenarios for a significant underground heritage site.

1.4 Thesis structure

Chapter 2 reviews terrestrial laser scanning technologies. It describes the available types of laser scanners and their respective measurement principles. The chapter considers errors sources present in TLS measurements and their influence on point cloud data. Registration and georeferencing techniques are discussed, with the application to heritage site documentation completing the chapter. Chapter 3 describes the methodology and results of a customised TLS control network, the network being established to quantitatively assess the outcomes of various GCP scenarios and the resulting point cloud accuracy. Chapter 4 applies the results from Chapter 3 to the LiDARRAS heritage site case study. Finally, Chapter 5 summarises the research findings and makes recommendations regarding the direction of future research.

Chapter 2 Terrestrial laser scanning: a review

2.1 Introduction

Chapter 1 briefly introduced Terrestrial Laser Scanning (TLS) and outlined the research objectives and questions, and mentioned the thesis aims and structure. This chapter will focus on the technique of TLS, with attention given to the registration and georeferencing of point cloud data. Applications of TLS will be discussed, focussing on heritage site documentation.

Laser scanning is referred to as Light Detection and Ranging (LiDAR), which can be either dynamic or static. Dynamic laser scanning is associated with the movement of a LiDAR platform, such as an airplane, boat, or moving car. Static laser scanning refers to a LiDAR platform remaining in a static position (Pfeifer and Briese, 2007a). The technique considered in this study is solely static LiDAR, or terrestrial laser scanning as it will be referred to here. For more information on dynamic LiDAR systems, see Vosselman and Maas (2010) and Shan and Toth (2008).

TLS instruments are active sensors that emit a laser beam and record x, y, and z coordinates (Cartesian coordinates) for a given point, as well as measure an intensity value of a given point. The point cloud data can be supplemented with RGB via an internal or external camera. The Cartesian coordinates are determined in the following way:

$$\begin{bmatrix} x \\ y \\ z \end{bmatrix} = \rho \begin{bmatrix} \cos\alpha \cos\beta \\ \sin\alpha \cos\beta \\ \sin\beta \end{bmatrix}, \quad (1)$$

where x, y, and z are the measured Cartesian coordinates, ρ is the range, and α and β are measured horizontal and vertical angles respectively. The x, y, and z coordinates are referenced with respect to the scanner's IRS (Alba and Scaioni, 2007). With advancements in TLS technology, up to a million points can be collected per second depending on the resolution predefined by the user. This chapter presents a review of current TLS instruments, errors present in the point cloud measurements, registration, georeferencing, and TLS applied to heritage site documentation.

2.2 Types of LIDAR

2.2.1 Time of flight scanners

A time of flight, or pulsed, laser scanner uses the speed of light and the time taken for a signal to leave and return to the TLS to determine range. The following equation is used to determine range (ρ):

$$\rho = {}^{1}/_{2}\, c\Delta t, \tag{2}$$

where ρ is the measured range, c is the speed of light constant, and Δt is the two-way travel time of the emitted and received laser pulse (Lichti and Harvey, 2002a).

2.2.2 Phase based scanners

Phase based scanners use the difference between a transmitted modulated phase signal and a measured received modulated phase signal (phase-shift) to measure a range (ρ) (Lemmens, 2011). The signal is modulated with short and long wavelengths that assist with precision and range ambiguity respectively. The range (ρ) measurement equation is as follows:

$$\rho = \lambda_m . \frac{\varphi_d}{4\pi}, \tag{3}$$

where ρ is the measured range, λ_m is the signal wavelength and φ_d is phase shift between the emitted and returned signal. An illustration for the time of flight and phase based range methods is shown in Figure 2.1.

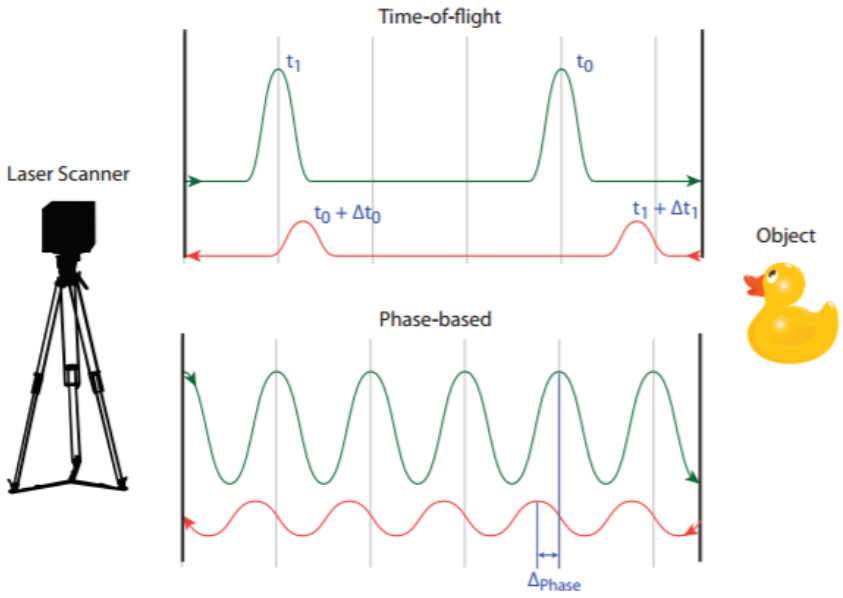

Figure 2.1. An illustration of the time of flight (top) and phase-based (bottom) scanning principles. Top, t_1 and t_0 represent time intervals for a released pulsed laser and Δt_1 and Δt_0 are time differences respectively. Bottom, Δ_{Phase} represents a difference between the emitted phase wavelength and the returned phase wavelength, known as a phase shift. Source: Soudarissanane, 2016

2.2.3 Triangulation scanners

The measurement principles of triangulation scanners use multiple points upon a plane that sweep through a scan scene. The technique utilises a laser emitter, laser line, and camera to create a triangle, thus allowing principles of trigonometry to measure distances. This type of scanning is mostly used for close range scanning (up to a few metres) as the precision of the

intersection is reduced with an increase in range (Figure 2.2) (Boehler and Marb, 2002). This type of scanning principle is common with handheld laser scanners. The range (ρ) equation is expressed as:

$$\rho = \frac{fd}{a}\cos\theta + d\sin\theta, \quad (4)$$

where f is the camera lens focal length, d is the triangulation base, θ is the deflection angle following the x-axis, and a is the position of the imaged laser spot of the position sensor (Blais *et al.*, 2000).

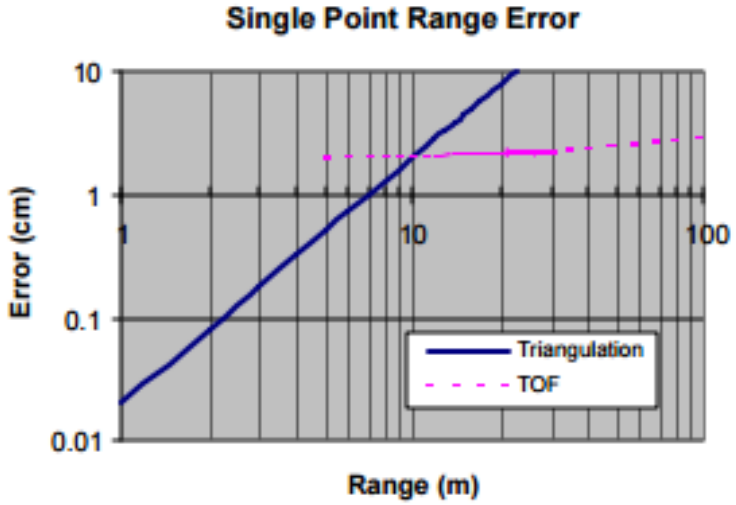

Figure 2.2. Blais et al. (2000) showing the relationship of range and error between triangulation (blue) and time of flight (magenta) laser scanners.

2.2.4 LIDAR summary

Three TLS ranging modes have been presented; time of flight, phase based, and triangulation scanners. Time of flight laser scanners have longer range acquisition compared to phase based scanners. The phase based scanning solution tends to be more accurate at range of up to 50 metres with faster data acquisition rates. The advancement in TLS technologies now means that time of flight and phase based scanners have similar acquisition rates and share similar accuracies. (See TX8 and TX5 datasheets in Appendix B; time of flight and phase based instruments, respectively). The triangulation scanner has limited applications based on the range, however at close ranges is capable of capturing sub-millimetre data.

2.3 Errors influencing the quality of point cloud data

Several error sources are present in point cloud data. Factors include scanning geometry, object properties, scanner mechanism, atmospheric conditions, and methodological errors (Boehler *et al.*, 2003; Van Genechten *et al.*, 2008; Soudarissanane *et al.*, 2011).

2.3.1 Scanning geometry

The scanning geometry relates the orientation and positioning of the scanning instrument with respect to the measured surface. The incidence angle, range, and point cloud density is determined by the placement of the scanner (Soudarissanane *et al.*, 2011). The incidence angle is the angle (α) between the laser beam vector (*p)* and the normal vector (*d)* of the measured surface (Figure 2.3) (Soudarissanane *et al*., 2011). In Figure 2.3 TLS_1 has an incidence angle of zero as the laser beam vector coincides with the normal vector of the measured surface, whereas TLS_2 has a laser beam that does not coincide with the normal vector of the measured surface. The angle of incidence will be larger for TLS_2 than TLS_1. The returned intensity from TLS_2 will represent a reduced Signal to Noise Ratio (SNR), which has been shown to affect the range determination in TLS (Soudarissanane *et al.*, 2011). This phenomenon is explained with the following equation, that assumes the reflected laser beam upon a measured surface is behaving as a Lambertian scatterer:

$$P_r = kP_t \cos \alpha, \tag{3}$$

where P_r is the power returned and detected by the scanner, k is a constant that depends on range, surface reflectivity, the aperture diameter of the receiver, as well as atmospheric and systematic effects. P_t represents the transmitted signal power, which leaves $\cos \alpha$ proving that the SNR ratio deteriorates with an increase in incidence angle α. An additional effect of an increased angle of incidence is the laser beam footprint on a measured surface, that will elongate and reduce the scanners ability to resolve finer details upon the measured surface (Soudarissanane *et al*., 2011).

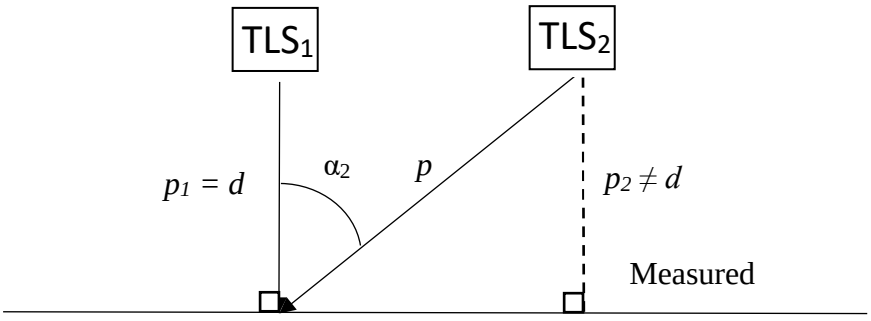

Figure 2.3. The schematic showing the relationship between the laser beam vector and the normal vector of the measured surface. TLS_1 has a laser beam vector (p_1) that coincides with the normal vector (d) of the measured surface, thus the incidence angle (α_1) is zero. TLS_2 has a laser beam vector (p_2) that does not coincide with the normal vector (d) of the measured surface, and therefore the incidence angle (α_2) is larger than the incidence angle for TLS_1. Adapted from Soudarissanane *et al.*, 2011

2.3.2 Object properties

The properties of a measured surface will determine the path of a reflected TLS signal, as well as the returned signal intensity; one such property is the surface reflectivity (Zámečníková *et al*., 2014). As noted by Zámečníková *et al.* (2014), TLS has the same basic principles of measurement as a total station and is subsequently susceptible to similar errors. The major difference is that the Electronic Distance Measurement (EDM) of a total station has been well investigated with respect to reflector-based measurement to a prism (Zámečníková *et al*., 2014). Being a reflector-less measurement system, the TLS returned signal is influenced by, but not limited to, the measured surface properties, such as colour, surface roughness, and the surface and subsurface material mineral compositions (Lichti and Harvey, 2002a; Delaloye *et al*., 2011; Zámečníková *et al*., 2014).

Properties of a measured surface will affect the scatter of a returned signal of a laser beam, for which there are six common types of scattering (Figure 2.4). They include specular, quasi-specular Lambertian, Minnaert, Henyey-Greenstein, and backscatter Henyey-Greenstein. All of these deflect light with different characteristics, influencing the signal strength for a given measurement (Rees, 2013).

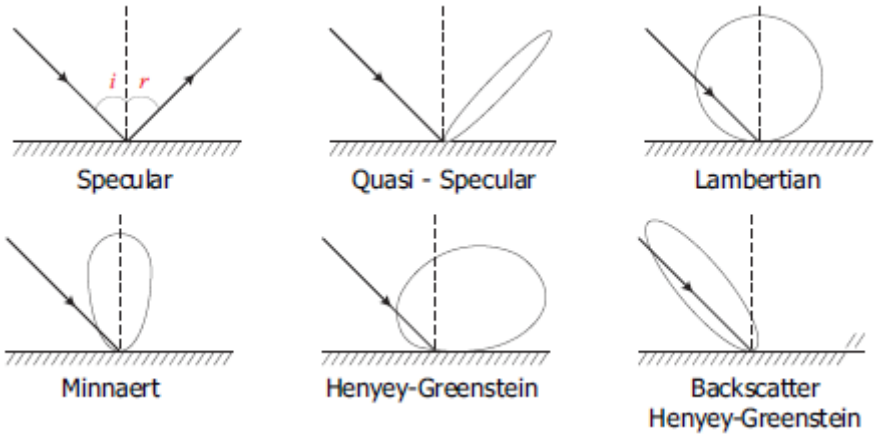

Figure 2.4. Six common types of scattering model. Source: Rees, 2013.

Investigations into various surface types; wood, concrete, metal, marble, and light-transmissive slides to various colours palettes, show that each surface has a slightly different effect on the way a laser beam is returned to the instrument. While most of these surface property types appear to have less of an effect on the range measurement, the reflected intensities vary with each surface and noticeable variation occurs between wet and dry surfaces (Lichti and Harvey, 2002a; Voegtle *et al*., 2008; Delaloye *et al*., 2011).

Voegtle *et al.* (2008) show how time of flight laser scanner measurements are influenced by various surface material properties. An interesting conclusion found in this paper suggested that measurements on bright materials made at night yielded a factor of 2 improvement in the measurement accuracy (Figure 2.5).

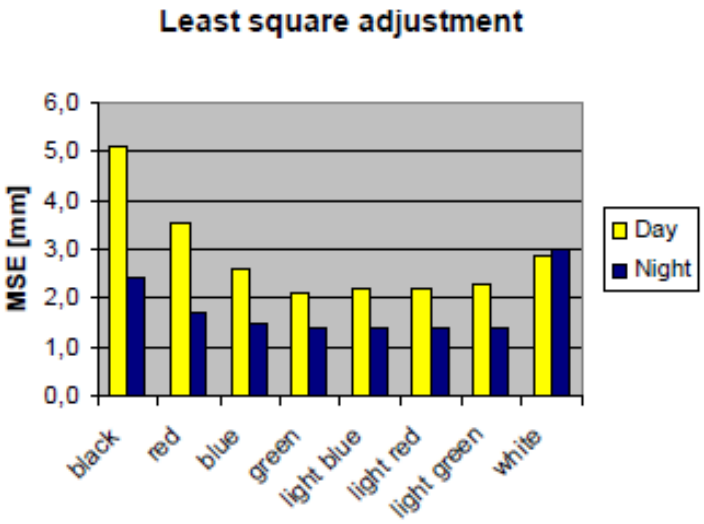

Figure 2.5. Range accuracy differences between day and night. Source: Voegtle *et al.*, 2008.

For more information on object property surface materials, the readers are referred to Lichti and Harvey (2002b) and Gordon *et al.* (2001).

2.3.3 Instrument hardware

The instrument hardware relates to the physical hardware design and calibration of the scanner. This is made up of, but not limited to, the scanner mechanism (axes), laser beam and footprint, and scanner beam width detection unit.

To cover a scan scene, the TLS instrument must rotate vertically and horizontally. TLS instruments, like total stations, have three axes; vertical, horizontal, and collimation. The vertical axis allows horizontal movement of the laser beam; it is the axis around which the TLS instrument rotates. The TLS mirror rotates vertically about the horizontal axis, and the direction of the laser beam is defined by the collimation axis (Van Genechten *et al*., 2008).

Typically, rotating mirrors are used to rotate the laser beam 180 degrees around the horizontal axis, while the TLS instrument rotates 180 degrees around the instrument's vertical axis. An oscillating mirror is another method of beam dispersion, where a mirror oscillates back and forth emitting a laser beam. Any errors related to the physical moving parts of the TLS instrument will influence the angular accuracy (Boehler and Marbs, 2002). Schulz (2007) discusses the calibration of TLS instruments in more detail, where the angular accuracy is

considered. The angular accuracy is considered as the deviations of the measured angles with respect to nominal angles resulting from a reference system. The angular accuracy is a nominated value specified by the manufacturer, with the Trimble TX8 being 80 µrad. Over short ranges this is considered negligible, however, this error source increases to about 9 mm at 120 m; the optimal scanning range of the TX8. Schulz (2007) concludes that the range measurement system is more important when considering the error model of a TLS instrument.

How much detail of a measured surface will be recorded by a TLS instrument is largely influenced by the laser beam and footprint. The width of the laser beam that is emitted from the instrument is termed the minimum beam width (Laefer *et al*., 2009). The radius of the emitted laser beam will, with diffraction, diverge from its minimum beam width. This is shown by the following equation:

$$\omega(z) = w_0\sqrt{1 + (\frac{\lambda z}{\pi\omega_0^2})^2}, \tag{5}$$

where $\omega(z)$ is the laser beam radius after emission, w_0 is the minimum beam width, λ is the laser light wavelength, and z is the distance propagated from beam waist location (Lichti *et al*., 2005). Over longer ranges the laser beam radius will increase, reducing the amount of detail recorded for a measured surface. The laser beam divergence affects the position of the measured point, where Lichti *et al*. (2005) show that the location of the actual point is somewhere within the laser footprint. This is considered the laser beam uncertainty, and is quantified as roughly equal to one-half of the laser beam radius. The instrument cannot record finer details than that of the laser footprint, thus keeping the size of the laser beam close to the minimum beam width (w_0) is desirable. The measured surface topography and scanning geometry will influence the laser footprint size. These two factors determine the angle of intersection between the laser beam and the measured surface. Deviating from the normal of a measured surface causes the laser footprint to elongate, as seen in Figure 2.6 (Sheng, 2008).

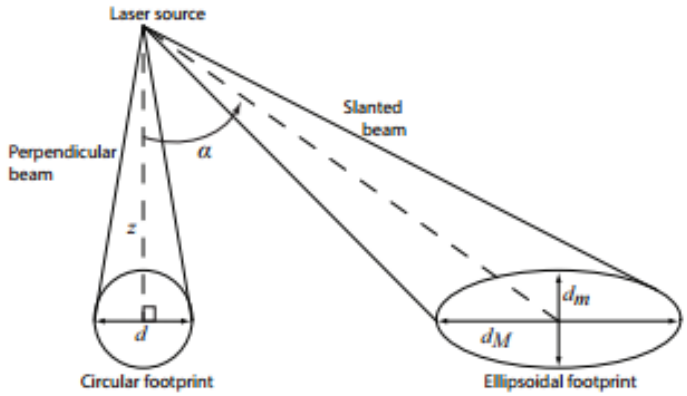

Figure 2.6. Laser footprint elongates with an increase of incidence angle (α) when compared to a laser perpendicular to the normal of a surface at the same distance (*z*). The elongated laser footprint is represented by a semi-axis major and minor, d_M and d_m respectively. Source: Soudarissanane, 2016.

An artefact of an elongated laser footprint is the possibility of recording two surfaces with a single measurement. This is termed, the mixed edge or edge effect. The phenomenon occurs when a laser footprint hits a surface edge and, due to the laser footprint being enlarged, returns signals from other surfaces (Figure 2.7) (Van Genechten *et al*., 2008). Edge effect returned signals result in points representing surfaces that may not exist. These points are considered gross errors and can either be removed from the dataset through user intervention or median filter (Lichti *et al*., 2005).

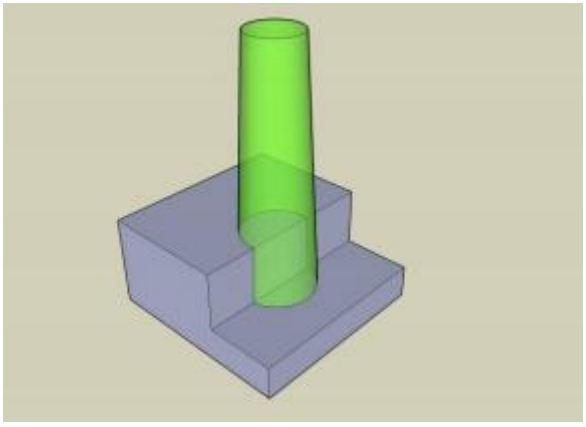

Figure 2.7. The mixed edge effect. The laser footprint will return a signal off two measured surfaces creating a point artefact. Source: Van Genechten *et al*. 2008.

2.3.4 Atmospheric conditions

TLS shares similar measurement principles to total station observations and is therefore subject to atmospheric errors. The atmosphere is a combination of temperature, humidity, and pressure, all of which affect the refraction value index and the length of the emitted laser beam wavelength. This means that a laser's travel speed and direction will vary in different atmospheric conditions affecting the range determination. The temperature of the TLS

instrument and measured surface need to be considered when scanning. The heating of the instrument may cause expansion in the scanner or tripod, which may result in expansion and distortion in the data (Van Genechten *et al*., 2008). Warm surfaces will influence the SNR, effecting the precision of range measurements (Van Genechten *et al*., 2008; Jafaar *et al*., 2017). In general, TLS instruments will allow users to enter values for temperature and pressure that allow for the necessary atmospheric corrections to be made. Exposure to interfering radiation may also influence the range measurement precision, due to the narrow frequency band that TLS instruments operate in. External radiation sources may include the sun or strong illumination sources from lights (Van Genechten *et al*., 2008).

2.3.5 Methodological errors

Methodological errors are described by Van Genechten *et al*. (2008) as, "errors due to the chosen survey method or the users experience with this technology", the result of choosing an incorrect resolution setting being an oversampled point cloud. The detail recorded by the instrument will be influenced by the laser footprint, and therefore having a finer resolution than the laser footprint size results in an oversampled point cloud (Licthi and Jamtsho, 2006). Additional points from the oversampling increases noise and processing times. Incorrect TLS instrument choice for the object being measured can result in a reduction of precision for a measured surface. Choice of registration and georeferencing techniques can also be considered methodological errors, which will be considered subsequently.

2.4 Registration

When undertaking a TLS survey, it is often found that multiple scans need to be completed to spatially cover the area of interest. Each scan will be referenced with respect to the instrument coordinate system. These individual scans must be aligned to a single reference system to make use of all the collected point cloud data. The process of aligning all scans into a common reference system is known as registration. The common reference system, aligned relative to a single scan station, is referred to as the Intrinsic Reference System (IRS) or local coordinate system (*See* Figure 1.1 *in Chapter 1*) (Alba and Scaioni, 2007). In TLS, there are two methods of doing this; using common targets in each scan or using automatic cloud registration methods, which rely on overlap between adjacent scans to complete registration.

Each scan has a 3D rigid-body transformation applied relative to a single reference station with six parameters; namely three rotations and three translations. A scale parameter is not included, given that the scanning instrument measures "absolute" distances. Therefore, to determine the

transformation parameters between stations, a minimum of three non-collinear points is required. Using three points assumes that the TLS instrument has not been levelled. Should the instrument be levelled, only two coincidental points are required (Lichti and Skaloud, 2010). In tunnel surveys where a long linear chain of registered scans is expected, additional points should be used to reduce registration inaccuracies. Low redundancy registration solutions may provide poorer accuracies than what might be expected from the adjustment precisions.

2.4.1 Target based registration

Target based registration is the practice of registering successive scans together via the use of common markers. This type of registration technique has been the traditional way of registering scans together using various target markers (Fan *et al*., 2015). These markers can be in the form of spheres, cylinders, or checkered targets; paddle board or paper target (Figure 2.8 and Figure 2.9) (Reshetyuk, 2009; Becerik-Gerber *et al*., 2011). The process of completing target based registration using common markers requires sufficient markers to be seen in successive scans. The following are things to consider when completing target based registration:

1. When completing a TLS survey for an area with a relatively small number of scans (five to ten), the position of the markers may not need to be changed, however when completing large TLS surveys with upwards of 100 scans, the placement of the markers can become cumbersome and time consuming (Pfeifer and Briese, 2007b; Theiler *et al*., 2014).
2. Additionally, this method requires these markers not to move. Should markers move, the registration may be compromised.
3. The targets are artefacts that require the user to remove them manually before modelling.
4. Targets may obstruct lines of sight between the TLS instrument and the measured surfaces, causing occlusions in the point cloud data (Theiler *et al.*, 2014).

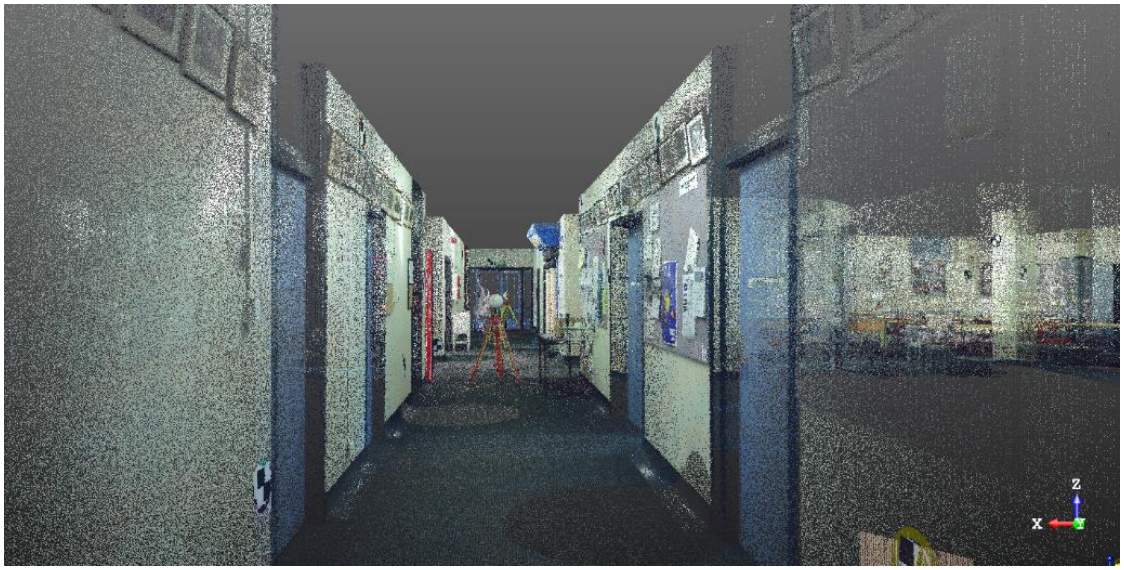

Figure 2.8. A typical example of common markers, showing checkered targets on the walls and a sphere on a tripod.

2.4.1.1 Accuracies of various target types and layouts

Target types and layouts play a role in the accuracy of the registration process. Becerik-Gerber *et al.*, (2011) shows that for the best results for target based registration, spheres have the highest accuracies. The other targets used for this research included checkered paddle board and paper targets (Figure 2.9). Spheres have the advantage of being symmetrical, thus in any direction the errors are based predominantly on the range between the instrument and target. Due to its symmetrical nature, the target does not require manual rotation in order to reduce the incidence angle. The paddle board is a TLS target that has the advantage of rotating around a central axis, allowing the target to be rotated perpendicular to the line of sight of the scanning instrument. Reducing the incidence angle has been shown to reduce errors in the point cloud dataset, making this target more desirable than a fixed paper target. Fixed checkered targets, if possible, should be placed in such a way that minimises the incidence angle (Soudarissanane *et al*., 2011). Alternatively, the instrument should be placed whereby this angle is reduced to mitigate any errors in the point cloud dataset. The checkered targets do have the advantage of having a high contrast and allow users to pick the discrete points with more certainty (Becerik-Gerber *et al*., 2011).

Figure 2.9. Target types used by Becerik-Gerber *et al.* (2011) for the investigation into various accuracies achievable using the above targets.

An investigation by Kersten *et al.*, (2005) show that systematic errors are present in the measurement of targets. At fixed range intervals, spheres render measurements longer than retro-reflective targets, which tend to be shorter than the reference range (Figure 2.10). Spheres had corrections of -3mm applied to measured ranges and the retro-reflective targets a correction of +12mm. This supports the conclusions made by Becerik-Gerber *et al.*, (2011), suggesting that spheres have higher accuracies than flat targets. Understanding target accuracies is important, as target identification error can directly influence the quality of the target-based registration process (Ge and Wunderlich, 2015).

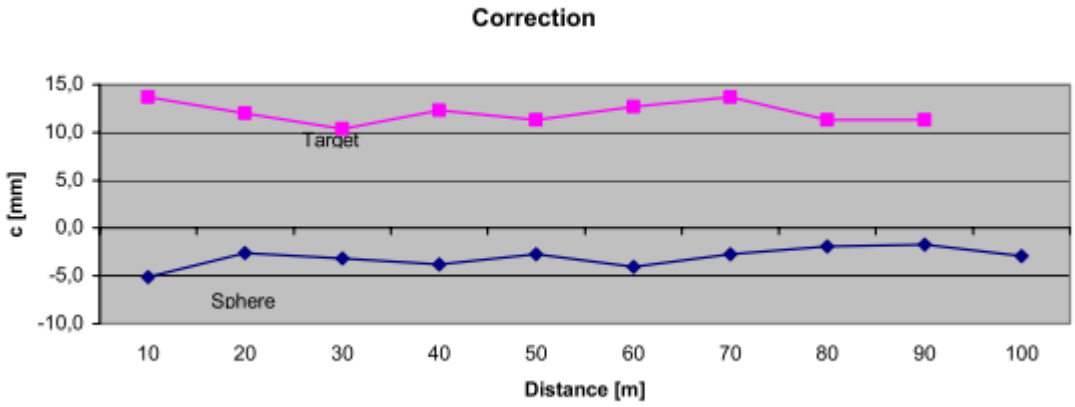

Figure 2.10. Retro-reflective (top) and sphere (bottom) comparisons to reference distances. Source: Kersten *et al.*, 2005.

2.4.2 Surface to surface registration

The surface to surface, or marker-less registration method relies on sufficient overlap between adjacent scans (Bornaz *et al.*, 2003). The technique is broadly based on the Iterative Closest Point (ICP) method. The ICP algorithm was first proposed by Besl and McKay (1992) whereby the rough alignment between scans is refined iteratively to minimise the average distance between points. Several adjustments have been made to improve the success rates of the algorithm (Chen and Medioni, 1992; Masuda and Yokoya, 1995; Bae and Lichti, 2008, Theiler

and Schindler, 2012). The automatic registration process is comparable with photogrammetry tie point adjustment that uses common features to join subsequent images together (Gruen and Akca, 2005).

The surface to surface registration technique is reliant on sufficient overlap between scan stations. Should there be an insufficient amount of overlap, the surface to surface registration may fail and manual user intervention is necessary. This may require the user to identify common features between the scan stations that will allow the registration process to be completed. Bornaz *et al.* (2003) suggest that discrepancies between common points in subsequent scans can be up to 180mm without sufficient overlap.

Table 2.1. Comparison between the target-based registration method and the surface to surface registration method.

Registration Technique	Method	Advantages	Disadvantages
Common Markers or Target-based	3 or more common markers seen in subsequent scans. (In the form of spheres, checkered, or cylindrical targets).	Can pick discrete points between scans.	Increased time required placing markers. Stability of markers. Post-processing segmentation.
Surface to Surface	Point cloud overlap (30%+ recommended Bornaz, 2003).	Reduced fieldwork time. No need for 3 markers to be seen per scan.	Potential for failed registration without enough overlap.

2.5 Georeferencing

Georeferencing is the process of taking the registered IRS point cloud and aligning it with a real work coordinate system or Ground Reference System (GRS) (Figure 2.11). Georeferencing is useful when combining multi-temporal datasets for deformation purposes, and combining datasets from diverse data capture techniques (Fan *et al.*, 2015). The two common ways of georeferencing point cloud data are the direct and indirect methods. Modifications have been made to these methods that use other instrumentation to do this or a combination of both techniques to reduce errors inherent in both the direct and indirect georeferencing methods (Lichti *et al.*, 2005; Pejic, 2013).

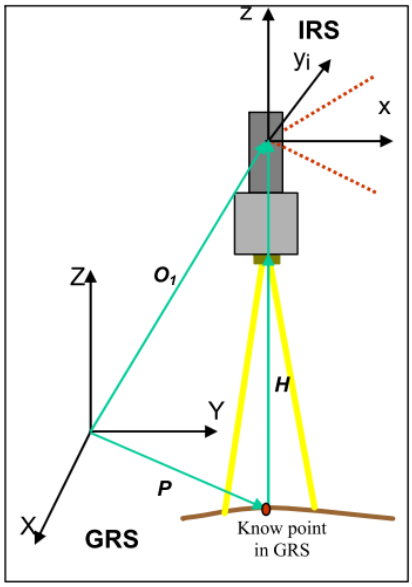

Figure 2.11. The principle of transforming the point cloud data from the Intrinsic Reference System to the Ground Reference System. Source: Alba and Scaioni, 2007.

2.5.1 Direct georeferencing

Direct georeferencing is the technique of taking the point cloud data from an IRS into a GRS by assigning a scan station with real world coordinates. The scanner is placed over a series of points with known coordinates from which the rest of the point cloud data will be coordinated (Alba and Scaioni, 2007). The points can be coordinated using traditional survey techniques such as a total station or GNSS. Using a total station, common practice is to perform a closed loop traverse that starts and ends on a mark with known coordinates. The advantage of using a total station over a GNSS unit is the fact that the control can be taken into buildings and underground, while maintaining survey grade accuracies. The use of GNSS is favourable in situations where no existing control is in the nearby vicinity of the area of interest (Fan *et al.*, 2015). If a TLS instrument be equipped with a telescope, it may be used similarly to a total station. The TLS instrument is set over a known position and can be oriented toward a backsight target similarly to a total station (Alba and Scaioni, 2007).

Other research includes combining the TLS instrument with a GNSS receiver and base then coordinates of the scanners position are post-processed (Figure 2.12). Assuming the scanner will rotate evenly around its vertical axis, the positional centre of the scanner can be determined in a Real-Time Kinematic (RTK) manner using a weighted mean of the observations (Figure 2.13) (Reshetyuk, 2010; Paffenholz *et al.*, 2010).

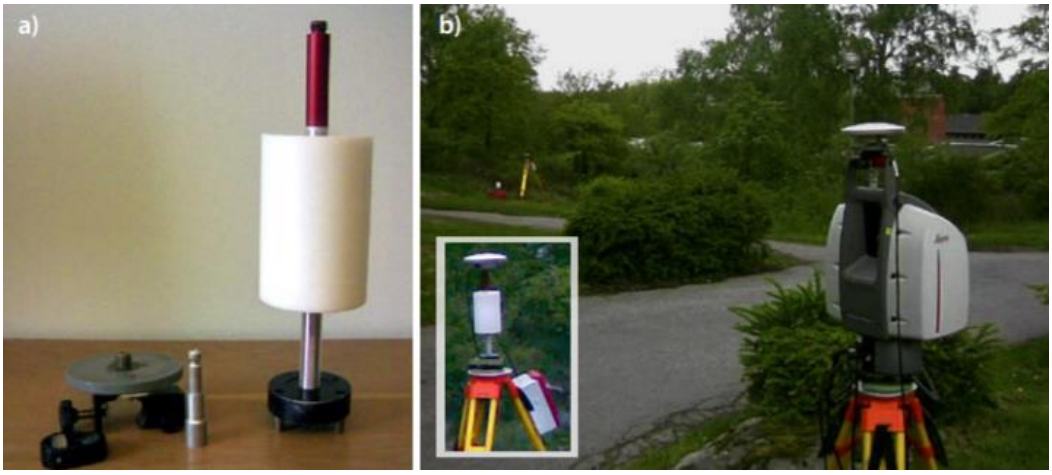

Figure 2.12. a) Shows an adapter for mounting the GNSS antenna onto the laser scanner (left) and a target with a mount for a GNSS antenna, used for scanner orientation (right). b) Shows the GNSS antenna mounted on top of a laser scanner (right) and the GNSS antenna mounted on top of the cylindrical target that is used for orientating the laser scanner. Source: Reshetyuk, 2010.

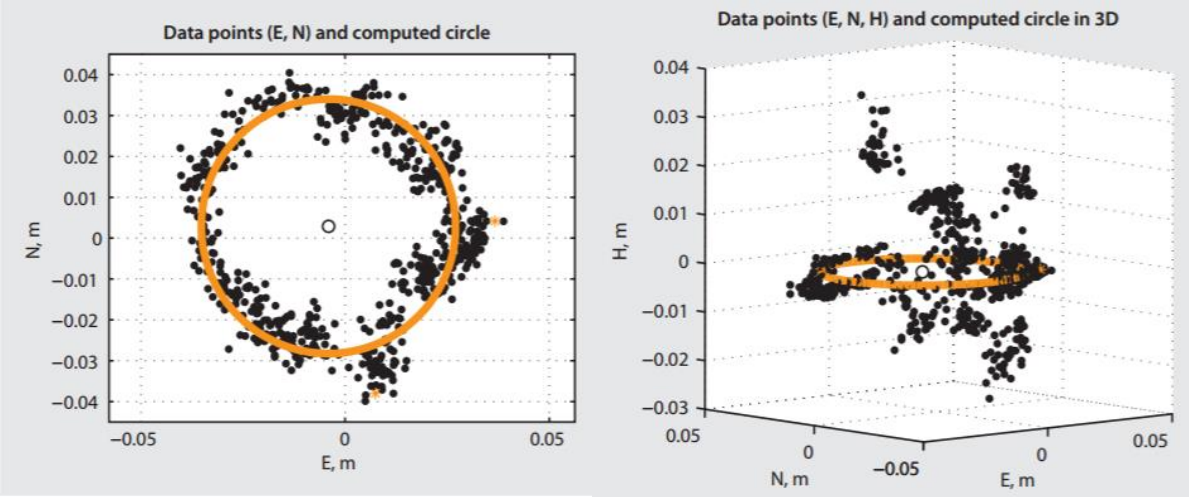

Figure 2.13. Reshetyuk (2010) shows results of combining GNSS with a laser scanner and how the centroid is determined for horizontal (left) and vertical (right) positions. Source: Reshetyuk, 2010.

2.5.2 Indirect georeferencing

Indirect georeferencing uses coordinated common markers to georeference point cloud data. This process uses established controlled points, placing common markers over these points, and capturing it with a TLS instrument. The marks are coordinated in the same manner as direct georeferencing, but the common markers are set up above a mark with known coordinates, rather than the instrument. The use of common markers is time consuming and appropriate configurations are not always possible, which may result in reduced point cloud accuracies (Reshetyuk, 2010; Dos Santos *et al.*, 2013). Reshetyuk (2010) and Becerik-Gerber *et al.* (2011) argued that the placement of markers can significantly affect the accuracy of the georeferencing

process, highlighting the importance of recognising “strong” and “weak” target geometries in a scan scene.

2.5.3 Arbitrary georeferencing

A hybrid approach for georeferencing tunnels is presented by Pejic (2013), known as the arbitrary georeferencing approach. The approach is an adaptation of the indirect and direct georeferencing techniques. Figure 2.14 depicts the optimal distance between scans and the position of the control points throughout the tunnel, which has been designed in such a way that maximises the distance between scans, control points, and angle of incidence with the scan surface (Pejic, 2013).

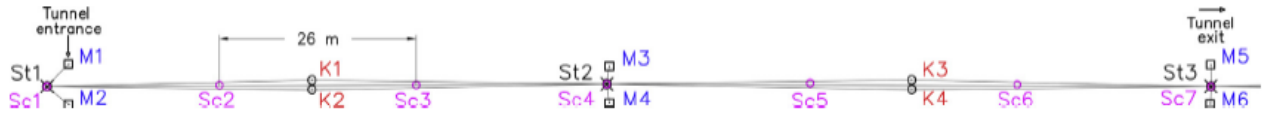

Figure 2.14. Arbitrary georeferencing approach adopted from the indirect georeferencing approach. Where St, M, and K are the position of control points and Sc are the relative scanner positions. St1, St2…, Stn are the forced centred total station positions. M1, M2, …., Mn are the scanner target control points on the walls, and K1, K2, …., Kn are the scanner target control points on the rail bolts. Source: Pejic, 2013

The arbitrary method is designed in a way that at every third scanning position the scanner will be forced centred on a total station control point, i.e. Sc1 and St1 will coincide and will increment every three scans and Sc4 and St4 will coincide and so on. As well as being forced centred at every third position, the scanner has perpendicular control points (M1, M2..., Mn) at each of these positions. At half the distance of the scanner positions (13m) additional control points are positioned to improve the reliability of the measurements as well as providing checks for the georeferencing quality (Pejic, 2013).

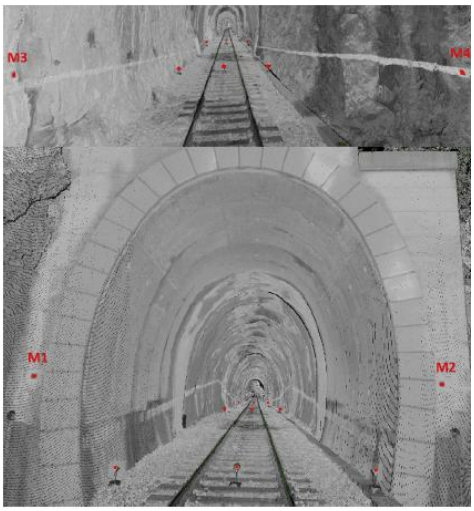

Figure 2.15. Point cloud output showing the arbitrary georeferencing control points in red. Source: Pejic, 2013.

Figure 2.15 shows a point cloud output from the arbitrary georeferencing approach with all the control points shown in red. The accuracy achieved from this approach was in the order of 1-2cm, which, compared to the indirect georeferencing technique that has errors in the order of 60cm, is of significantly higher quality. The two georeferencing approaches were used for the same tunnel, for which the histogram results are seen in Figure 2.16.

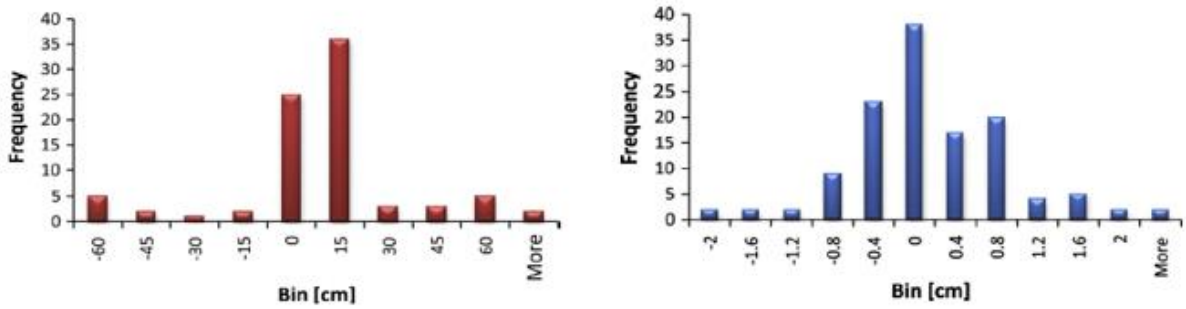

Figure 2.16. Histograms showing the difference between the indirect georeferencing approach (left) and the arbitrary georeferencing approach (right). Source: Pejic, 2013.

The histograms show how the arbitrary georeferencing approach allows the geometric distortions to be controlled to given limits of 2cm. This method highlights the importance of mitigating incidence angles to a measured surface, maintaining optimal distances between scan stations, and having GCPs placed evenly throughout the scan scene. When georeferencing and modelling, it is necessary to specify the limits of accuracy required. This will determine the appropriate georeferencing method that should be used to acquire the desired accuracies.

2.5.4 Errors present in georeferencing

Lichti and Gordon (2004) confirm that to quantify the error budget of the point cloud dataset, all random error sources need to be considered. They define these errors as from internal and external sources. Internal sources are comprised of and not limited to noise in an observation and beamwidth uncertainty, while external sources are made up of and not limited to TLS instrument setup errors and the survey points used for registration. The research presented by Lichti and Gordon (2004) is related to errors present in directly georeferenced point clouds. Figure 2.17 shows simulated error propagation results for 0° and 40° elevation angles. The results show that with an increase in the angular component, the errors (95% C.I.) reach nearly 300mm at 80m from the scanner. The basis for the results is an error budget, based predominantly on the manufacturer's specifications. Prevailing angular error sources were the beamwidth error and the vertical and horizontal angular observation noise. The results from this also highlight range as a significant error source, and where possible should be reduced to mitigate the error propagation.

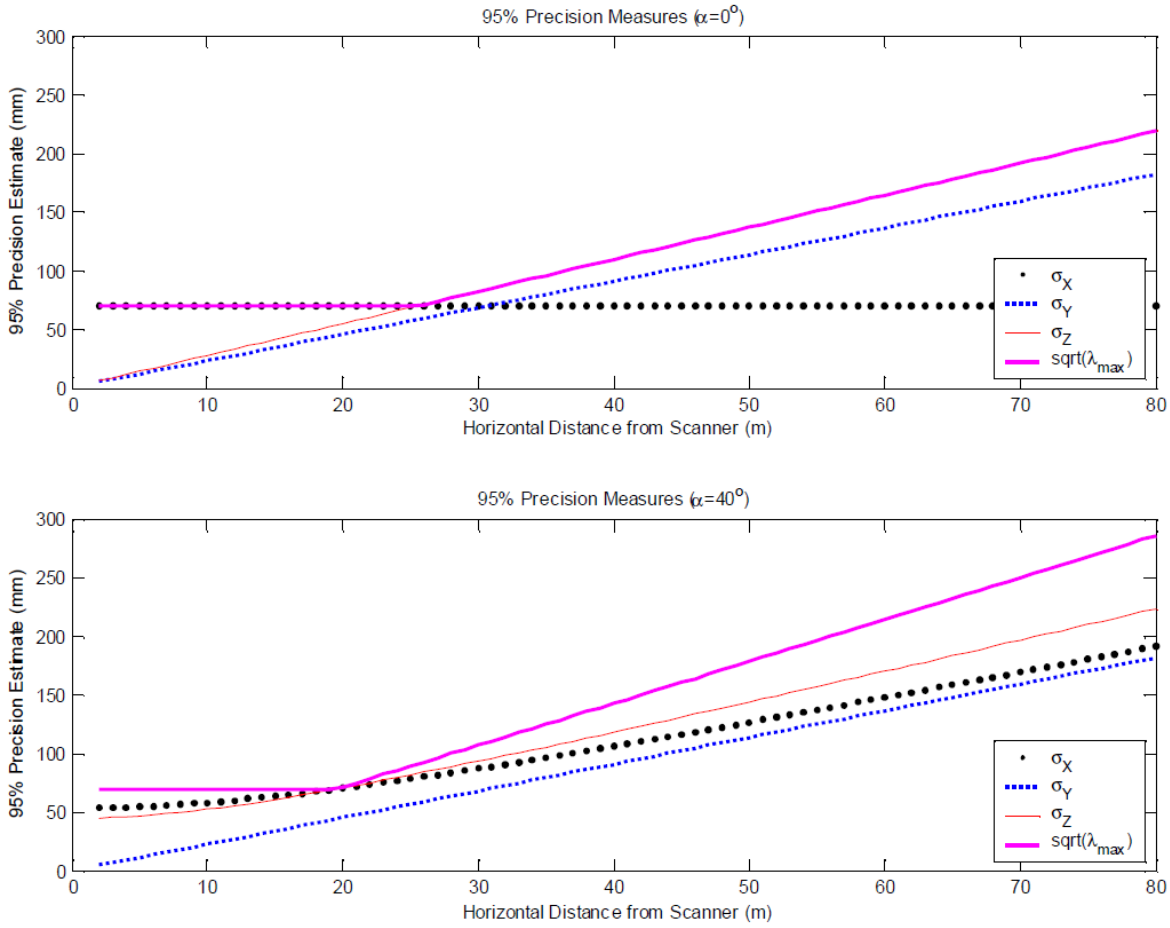

Figure 2.17. Results for a simulated error propagation analysis. Top is a 0º elevation angle, and bottom is a 40º elevation angle. Source: Lichti and Gordon, 2004.

2.6 TLS for heritage site capture and modelling

Terrestrial laser scanning has grown in popularity for heritage site capture and modelling, with applications ranging from mapping of archaeological tunnels, to scanning structures with historic significance (Lichti and Gordon, 2004; Rodríguez *et al.*, 2015). The benefit of a TLS instrument for the purposes of heritage site documentation is the use of non-contact measurement, preserving the natural state of the heritage site (Lambers *et al.*, 2007; Lai *et al.*, 2015). A precise 3D digital record allows the preservation, restoration, and management of historic sites (El-Hakim *et al.*, 2003; Geyman, 2009). Numerous individual scans, up to thousands, can be taken to document and record heritage sites, and a clear understanding of the deliverables is desired. Inexperienced operators may find themselves collecting too much or too little data resulting in gaps in the scan scene or unmanageable datasets (Grussenmeyer *et al.*, 2008; Rüther *et al.*, 2011; Barsanti *et al.*, 2012). A typical workflow for heritage site documentation is shown in Figure 2.18.

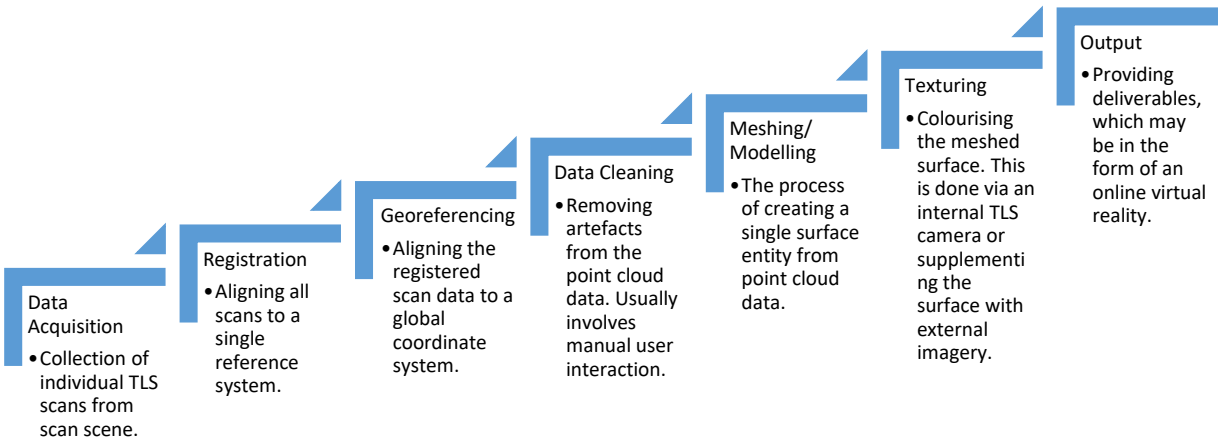

Figure 2.18. Typical workflow for TLS heritage documentation.

Fine surfaces details that need to be recorded for heritage sites mean that it is imperative to correctly manage certain aspects of the workflow. Things to consider are the instrument resolution, range, laser footprint upon a measured surface, and the post-processing of the large point cloud dataset. The larger the laser beam footprint, the less detail of a surface will be captured (Lichti and Gordon, 2004; Van Genechten *et al.*, 2008; Soudarissanane *et al.*, 2011; Rüther *et al.*, 2011). Data fusion between photogrammetry and TLS point cloud data has been shown to reduce mesh triangles by nearly 60 percent, while still preserving details (Figure 2.19). El-Hakim *et* al., 2004 used the two data capture approaches to model aboriginal rock art. Photogrammetry was used to model the general shape of rocks, while a TLS instrument was used to capture the finer art details. The two techniques were combined into a single reference

system using defined survey points, visual in both data. No technique is more suitable than the other to capture a heritage site; they are case dependent (Grussenmeyer *et al.*, 2012; Guidi *et al.*, 2002). Combining techniques allows for a manageable dataset, which is still seen as a limitation when recording heritage sites with TLS instruments, due to hardware post-processing capabilities. (El-Hakim *et al.*, 2004; Lambers *et al.*, 2007; Remondino, 2011; Lai and Sordini, 2013).

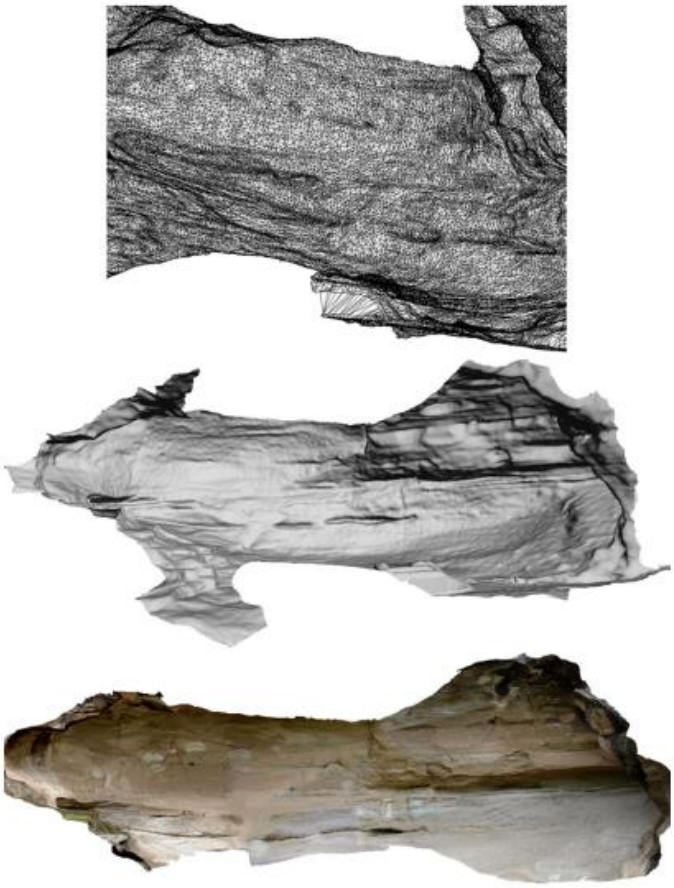

Figure 2.19. Top: a wire frame (TIN). Middle: un-textured mesh. Bottom: mesh with texturing. Source: El-Hakim *et al.*, 2004.

The data can be used to create virtual reality models, allowing for larger audiences to experience and visualise a heritage site without having to physically access the site (Nettley *et al.*, 2011). For several reasons, this can be beneficial, and may include preservation of the heritage site with less foot traffic causing less physical damage, access for all persons to sites which are restricted from the public, or alternatively access to remote sites that people would otherwise not be able to reach. Other benefits of TLS for heritage site capture and modelling include restoration, planning and appropriate management of these sites (El-Hakim *et al.*, 2003; Rüther *et al.*, 2011).

2.7 Chapter summary

TLS principles were considered in this chapter with attention being given to heritage applications. To note, the factors influencing the quality of point cloud data, registration and georeferencing techniques, and typical TLS workflows for heritage site documentation were discussed. A typical point cloud dataset may be subject to errors based on scanning geometry, scanner mechanism, object properties of a measured surface, and atmospheric conditions. Research shows that these factors all influence the quality of the point cloud data, and various attempts as means of mitigating these error sources. The registration and georeferencing processes can be completed in various ways, all with their individual time constraints, accuracies, advantages, and disadvantages. TLS heritage documentation and modelling survey applications have also been reported, with a typical workflow being presented. TLS has proved to be a useful tool for the capture and documentation of heritage sites with various case studies being presented above. Chapter 3 will discuss the methodologies implemented for the establishment of the control network and the undertaking of the TLS survey. The TLS survey applies registration and georeferencing scenarios investigated in this research, with the automatic surface to surface registration and indirect georeferencing techniques being utilised.

Chapter 3 Testing ground control point configurations

The previous chapter outlined TLS principles, namely registration and georeferencing principles, as well as its application to heritage site documentation. This chapter outlines the methodologies implemented in this research. Such methodologies include, establishing a control network using traditional surveying techniques (total station), the undertaking of the TLS data capture, and the processing of the TLS data, all of which are typical workflows for heritage site documentation.

The purpose of the research in this chapter was to establish appropriate methodologies for the case study in Arras, as time was limited and the extent of the fieldwork significant while in France. One of the LiDARRAS project objectives was to capture an accurate point cloud. Therefore, as a preamble to the LiDARRAS case study in Arras, a test survey was established within the School of Surveying (SoS) building to investigate various indirect georeferencing scenarios. Georeferencing is the process of taking the point cloud from the IRS to the GRS. The indirect georeferencing technique uses coordinated common markers throughout the scan scene that are measured in overlapping scans. These coordinates common markers are used to georeference the point cloud data.

This chapter is structured as the following; the methodologies for the established survey control network and the TLS registration and georeferencing techniques are presented. The results of the survey control network and TLS survey are then presented, with the chapter summary following.

3.1 Method

3.1.1 Context of the test survey

The purpose of the test survey network was to create a control network of coordinated points to be used for the TLS survey, with the objective of testing various georeferencing scenarios that fixed more, less, and spatially variable Ground Control Points (GCPs). The outcomes of the TLS survey being used to inform the fieldwork process for the LiDARRAS heritage site where time was a limiting factor. The test was conducted on the ground floor of the School of Surveying building.

3.1.2 Control network

An initial control network was established as a means of testing the various georeferencing scenarios. The control network was established using a Trimble M3 Total Station (TS) and was

completed in two steps. The first step was to create a closed loop traverse of points that were used to establish coordinated TLS control points. (Figure 3.1). All “NAL” positions shown in Figure 3.1 are on the ground floor of the SoS building while an existing control point (BYKH) was used to create the closed loop traverse throughout the test area. Point coordinates were extracted from the Land Information New Zealand (LINZ) geodatabase website (LINZ, 2016). The software package 12d v.11 was used to complete the coordination of the new survey control. The Bowditch method was used to distribute the misclose, where the misclose is distributed as a ratio of the length of traverse line, i.e. for a total traverse misclose of 0.01 m over a 100 m traverse, for a line of 50 m, 0.005 m of error would be distributed to the line. The second step was to coordinate a network of TLS targets from the closed loop traverse points (Figure 3.2). Under various TLS georeferencing scenarios these targets were used either as fixed GCPs or used as Check Points (CPs). The reflectorless measurement mode was used to perform this task with a total of 173 observations being made. Two points, 0001 and 0034, had a single observation each, with all other points being observed by two or more independent station setups. A LSE adjustment was performed in the software package Survey Network Adjustment Package (SNAP). A network of marks made of 5 spheres (NAL6 was not used for the TLS survey) and 36 photogrammetric patterns placed on walls at various heights was designed (Figure 3.4). Figure 3.3 is an extract of point cloud data showing an example of the targets used for this assessment.

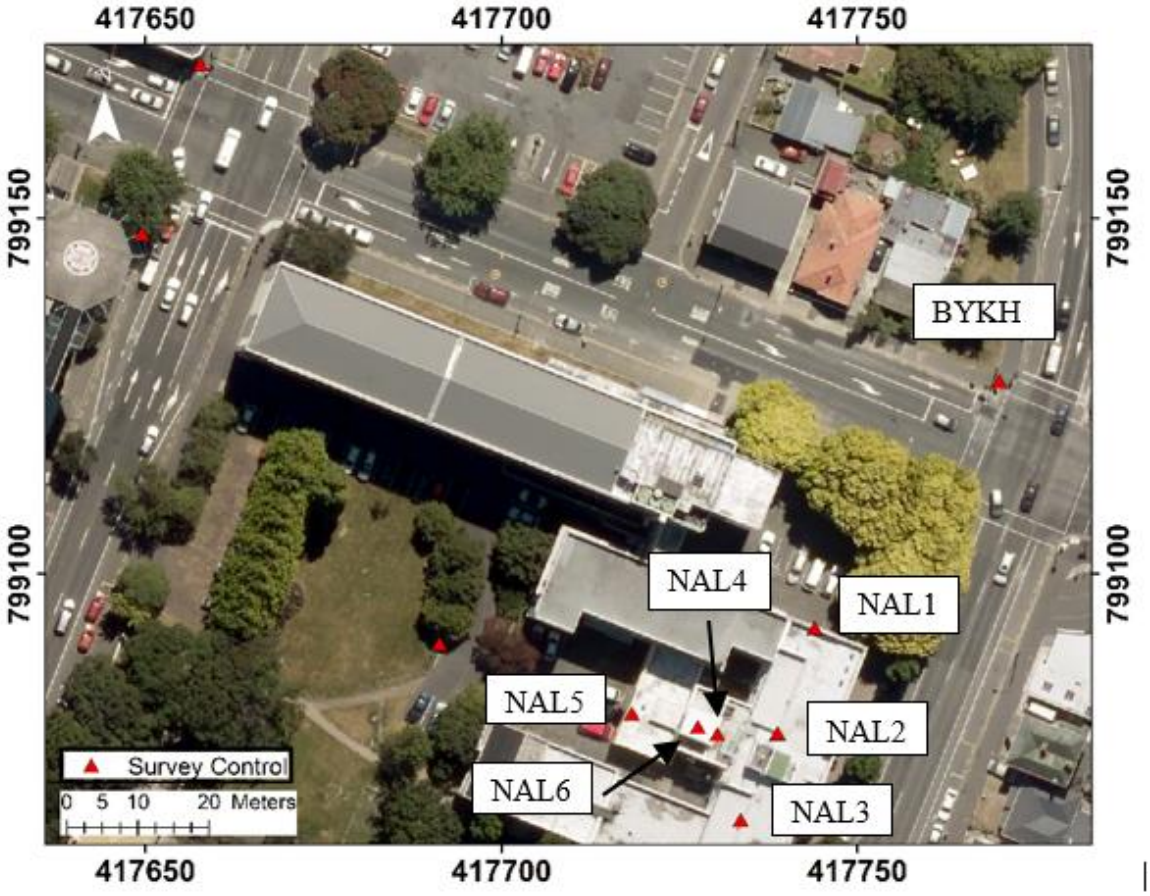

Figure 3.1. Aerial view showing the initial traverse that was completed prior to coordinating the remaining TLS targets. Axes represent planimetric coordinates in metres according to NZGD 2000, North Taieri Circuit.

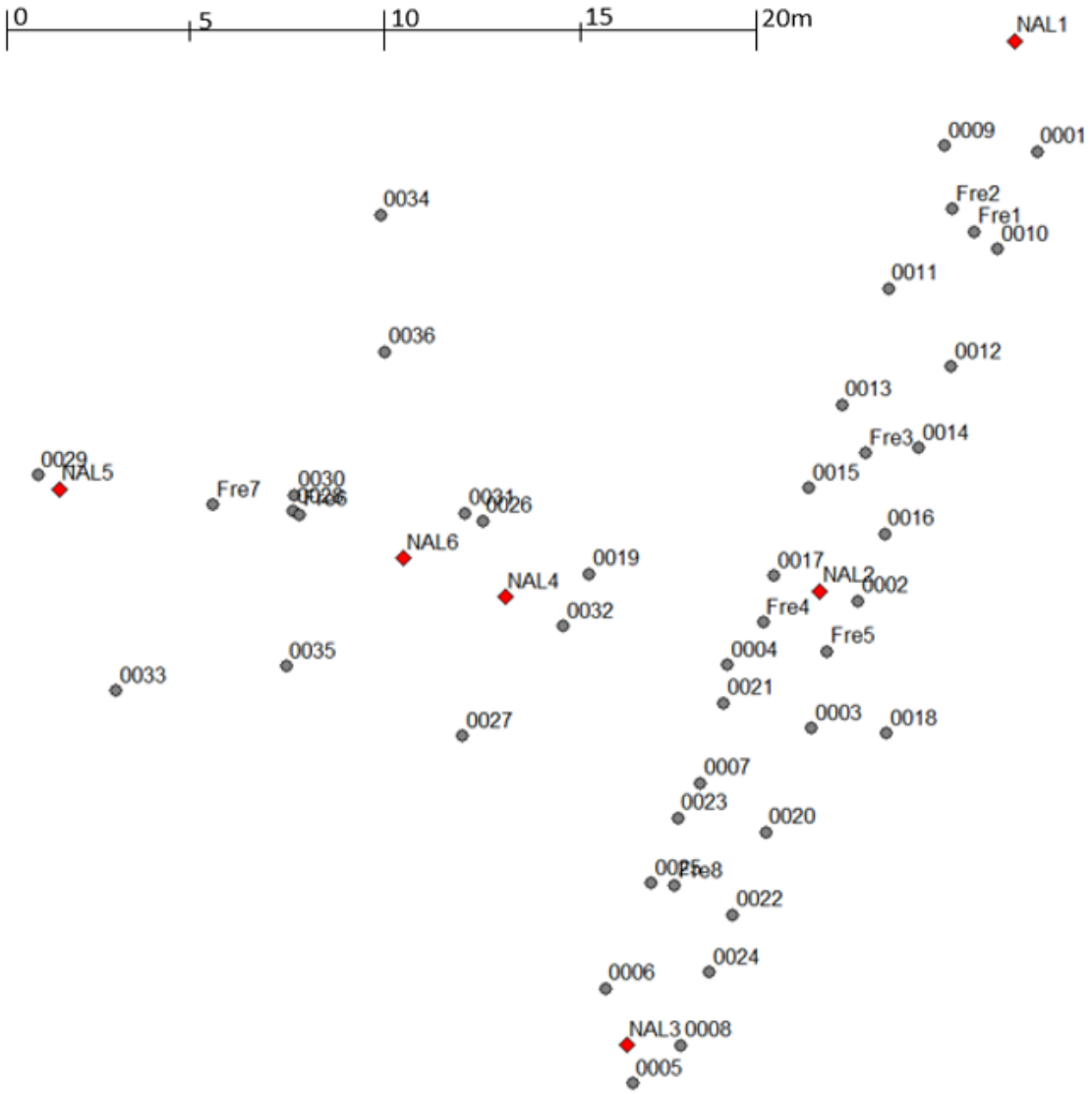

Figure 3.2. Placement of ground markers with *NAL* corresponding to spheres and numbers corresponding to photogrammetric checkered targets, respectively. ****Fre were free stations used to coordinate targets and have not been used to undertake the TLS survey.*

3.1.3 TLS survey

A TLS survey was performed using the Trimble TX5 laser scanner; a phase based laser scanning instrument. A total of 22 scans were completed of the interior of the SoS building (Figure 3.4). The instrument resolution was set at 12 mm at 30 m, with most surfaces being scanned closer than 10 m. Distances between scan station positions were kept short due to the registration technique implemented, surface to surface, which requires adequate overlap for a successful registration to occur (Bornaz *et al.,* 2003). The position of each scan station was considered, whereby the incidence angle was mitigated as literature has shown this to have a significant effect on the quality of the point cloud data (Soudarissanane *et al.*, 2011; Soudarissanane, 2016).

Figure 3.3. Point cloud data of scanned corridor, showing GCPs and CPs in the form of spheres and checkered targets.

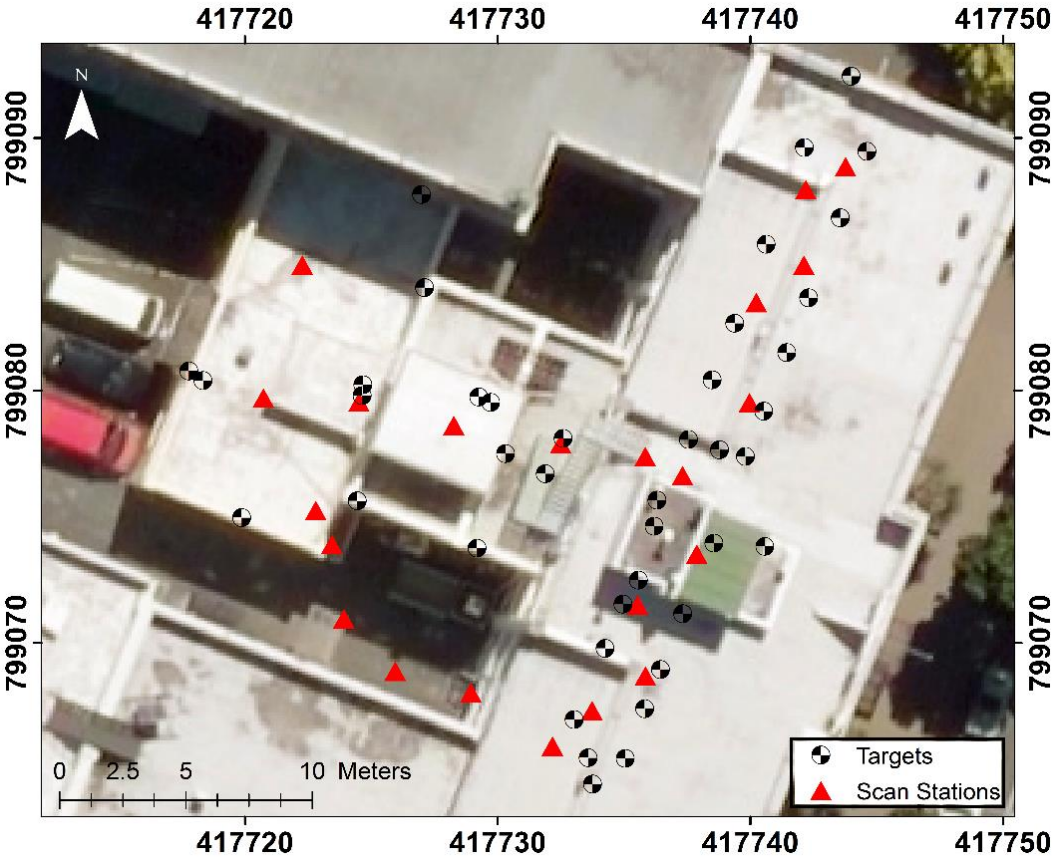

Figure 3.4. Test area at the SoS, showing scan stations (triangles) and the horizontal positions of the targets used for each accuracy assessment. Positions of the scan stations and targets are on the ground floor of the SoS building. Axes represent planimetric coordinates in metres.

3.1.4 Registration

Trimble RealWorks v10.0 was used for the processing of the scan data. The data was registered using automatic surface to surface registration techniques. Several reasons for this include; the lack of targets on the outside of the SoS building where three scans did not register correctly using the target-based registration method, and the placement of targets in the network of

underground tunnels in France would have been time intensive (~1,000 scans were completed). With loose gravel surfaces in the tunnels, the quality of the registration process might have been compromised should the position of a sphere move due to surface instability. For consistency when undertaking the SoS accuracy assessment of various georeferencing scenarios, as well as this being the registration technique applicable to the LiDARRAS project, the data was registered using automatic surface to surface registration techniques (Becerik-Gerber *et al.*, 2011; Pfiefer and Briese, 2007b). A registration report is produced by Trimble RealWorks, stating the overall fit of registration process. The report outlines the overlap of each point cloud with respect to other point cloud data in the scan scene and gives a confidence, in percentage, to the overall fit with these point clouds (*See Appendix A*).

3.1.5 Georeferencing

The point cloud data was georeferenced after visually inspecting the outcome of the registration process. Georeferencing point cloud data is the process of transforming point cloud data coordinates from the IRS to a GRS (Alba and Scaioni, 2007), providing absolute coordinates. Chapter 2 outlines the georeferencing process in more detail. To assess the quality of various GCP scenarios, particularly as some may result in large error propagation/systematic distortion of the final point cloud model, a reference scenario was chosen for each ensuing scenario to be tested. T1 was chosen as the reference scenario as it covered most of the scan scene compared to the scenarios tested (Figure 3.6 and Table 3.1). T2 and T3 have three GCPs in common with T1 that cover the extents of the scan scene. T4 and T5 are variations of three GCPs, which assessed the placement of GCPs. T6, T7, and T8 tested additional GCPs to see if more control, in spatially weaker configurations, were comparable to scenarios with less control. T9 has 10 less scans than the other scenarios, testing the influence of less scans on the accuracy of the point cloud data (Bornaz *et al.*, 2003).

Table 3.1. Summary of the tested GCP scenarios.

Scenario	Scenario Description
T1 (Reference)	8 GCPs evenly distributed around scan scene
T2	5 GCPs evenly distributed around scan scene
T3	3 GCPs evenly distributed around scan scene
T4	3 GCPs distributed as a baseline on one side of the scan scene
T5	3 GCPs clustered in a single corner of the scan scene
T6	8 GCPs distributed as a baseline on one side of the scan scene
T7	5 GCPs distributed as a baseline through the centre of the scan scene
T8	5 GCPs clustered on one side of the scan scene
T9	3 GCPs (T3) with 12 scans instead of 22

Subsequent to georeferencing, a report is produced for each scan station that provides information about the 6-parameter transformation applied to the station as a result of the adjustment. The transformation is reported by means of a translation vector, Euler rotation vector, and corresponding angle of rotation is reported by RealWorks relative to the software coordinate system (Figure 3.5).

```
# Station name : Ss_test000
# RMX creation date : Mon Apr 18 13:11:35 2016

# translation vector (millimeters)
417743775.678427 799088857.685613 6499.796926

# rotation axis direction
0.000658 0.005020 -0.999987

# rotation angle (radians)
0.376608
```

Figure 3.5. Typical station translation and Euler rotation output from Trimble RealWorks with respect to the software coordinate system.

The software coordinate system common in each scan is used to determine the relative translations and rotations of subsequent scans with respect to a reference scan station. This was done for each GCP scenario shown in Table 3.1, with the purpose of assessing how each scenario provoked a change in the subsequent scan stations positions relative to the reference scan. The departure (translation and rotation) from the origin was transformed to a single reference station that was used to compare each adjustment and TLS survey under various GCP scenarios. This was done prior to assessing the accuracy of each of the CPs, to assess whether the software applied a bundle block adjustment to the entire point cloud, or if the software allowed each station to transform independently and apply a best fit solution based on the GCPs being fixed. Each remaining target was used as a CP to assess the accuracy of the point cloud data under the tested georeferencing scenarios.

The following matrix and equations define the transformations applied to each station adjustment parameters (Figure 3.5) to determine a translation and rotation relative to a single reference station and thus to compare the various scenarios. A rotation matrix $\boldsymbol{R}$ that describes the 3D orientation of each scan with respect to the software coordinate system can be obtained as,

$$\boldsymbol{R}_{=}\begin{bmatrix} \cos\theta + u_x^2(1-\cos\theta) & u_x u_y(1-\cos\theta) - u_z\sin\theta & u_x u_z(1-\cos\theta) + u_y\sin\theta \\ u_y u_x(1-\cos\theta) + u_z\sin\theta & \cos\theta + u_y^2(1-\cos\theta) & u_y u_z(1-\cos\theta) - u_x\sin\theta \\ u_z u_x(1-\cos\theta) - u_y\sin\theta & u_z u_y(1-\cos\theta) + u_x\sin\theta & \cos\theta + u_z^2(1-\cos\theta) \end{bmatrix}, \quad (5)$$

where, $\boldsymbol{R}$ is the rotation matrix for a scan station with respect to the software coordinate system origin. u_x , u_y, and u_z represent the rotation axis direction and θ the Euler rotation vector reported by RealWorks.

The translation vector between the reference scan station and each subsequent scan station is computed as,

$$\boldsymbol{t_{rel}} = \boldsymbol{R_1}(\boldsymbol{t_2} - \boldsymbol{t_1}), \tag{6}$$

where, $\boldsymbol{t_{rel}}$ is the translation vector between scan station 2 relative to the reference scan station 1, $\boldsymbol{R_1}$ is the rotation matrix of the reference scan station, $\boldsymbol{t_1}$ and $\boldsymbol{t_2}$ are the translation vectors of the reference scan station and succeeding scan station, respectively.

Equation 7 relates the orientation of station 2 relative to the reference scan station 1,

$$\boldsymbol{R_{rel}} = \left(\boldsymbol{R_1}\boldsymbol{R_2^{-1}}\right)^{-1}, \tag{7}$$

where $\boldsymbol{R_{rel}}$ is the orientation between scan station 2 with respect to the reference scan station 1, $\boldsymbol{R_1}$ is the rotation matrix for the reference scan station 1 and $\boldsymbol{R_2}$ is the scan station 2 rotation matrix (Growcott *et al.*, 2012).

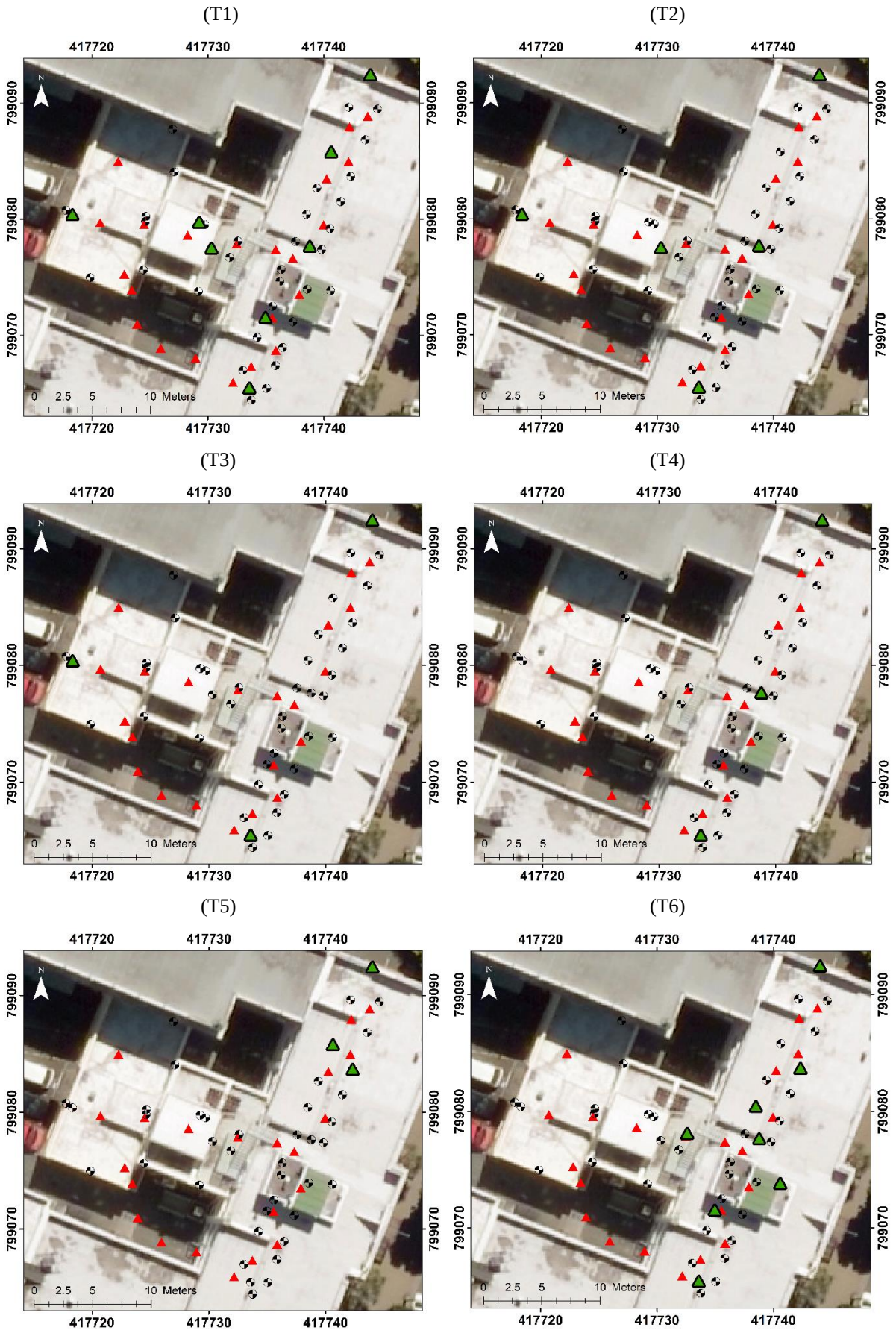

Figure 3.6. Various GCP scenarios tested.

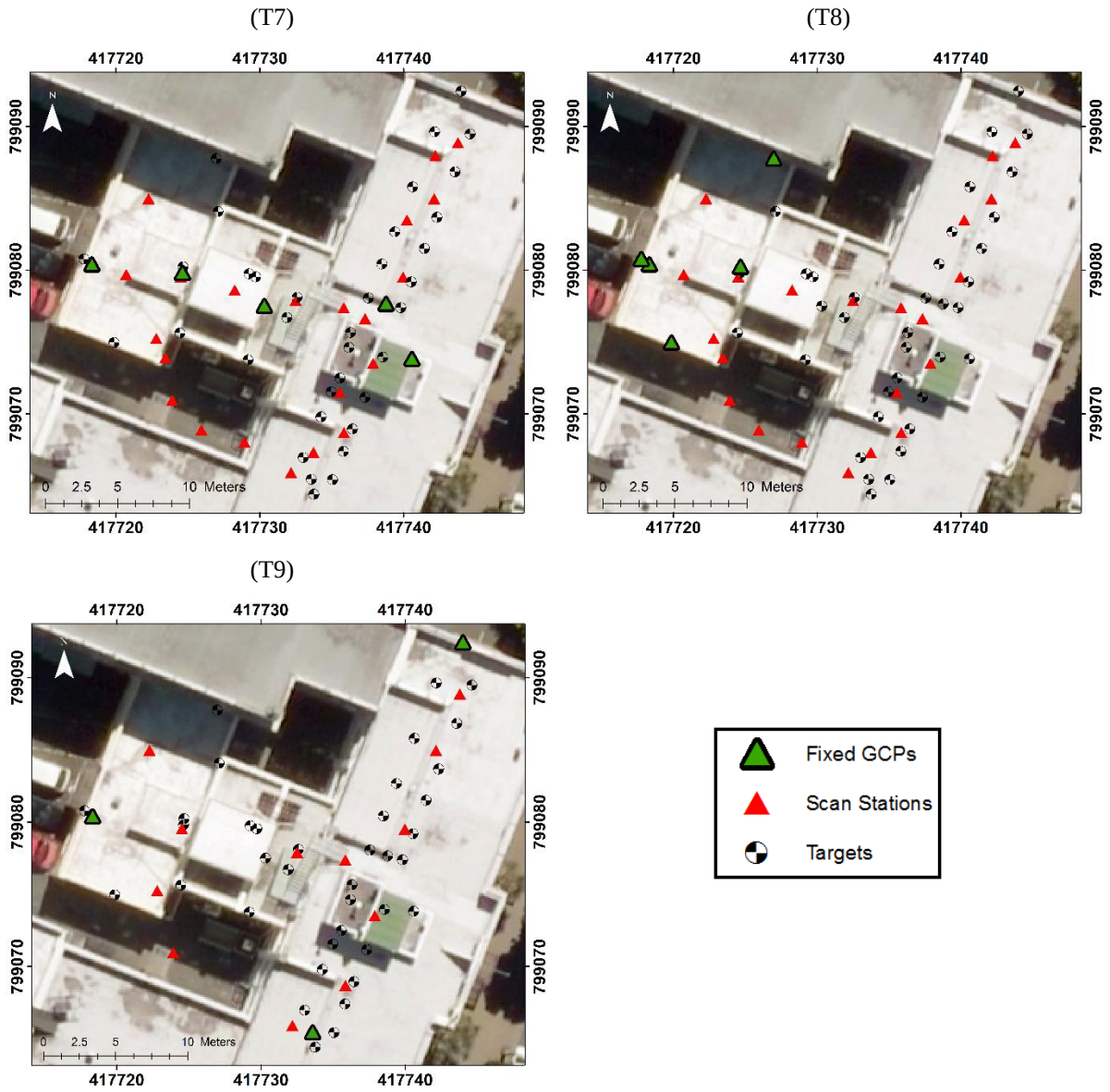

Figure 3.6 (Cont.). Various GCP scenarios tested.

3.2 Results

3.2.1 Control network

The existing control coordinates (Figure 3.1) that were used to establish the control network (Figure 3.2) were accessed from the LINZ geodetic database. The control point BYKH was held fixed and a closed loop traverse performed. The misclose of 8 mm was distributed using the Bowditch method, which distributes error proportionately to the length of each observation.

The control network point coordinates and error ellipses are seen Figure 3.7 and Table 3.2. The error ellipses are shown at a 95% confidence interval, with the largest horizontal errors being

associated with the two check points, 0001 and 0034, of 11 and 8 mm respectively. The maximum vertical error of a single position was 2 mm, at point 0034.

Because of the short distances between the CPs, the a priori estimate was increased to 10 seconds for the horizontal and vertical angle measurements. The a priori distance measurement was set at 2 mm + 0 ppm. The 0 ppm was set due to the short distances. The a posteriori values showed that the observations were poorer than the a priori estimate, and increased to 22 seconds for the angular measurements and 4.4 m for the distance measurements. No outliers were removed due to the practical effect each removal had on the outcome of the coordinates for a given point. The removal of an observation due to an angular outlier over a distance of a few metres had practically no effect and hence no observations were removed.

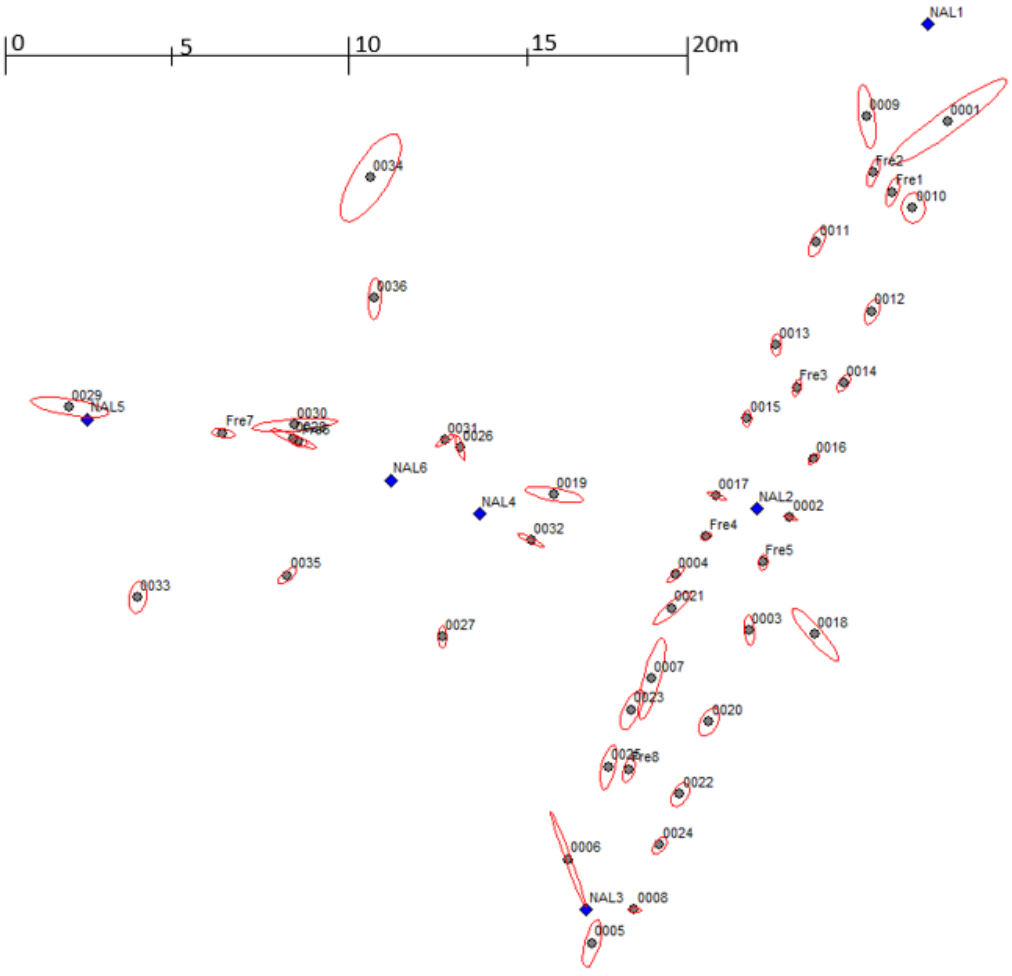

Figure 3.7. Control point error ellipses shown at 95% confidence interval. Error values shown in Table 3.2. Blue points are coordinated from the survey control network. These control points were used to coordinate the check points for the TLS assessment. Each grey point with an associated error ellipse represents a TLS CP. *FRE points denote total station resection setups that were used to make distance and angle measurements to each CP.

Table 3.2. Control network point list showing easting, northing, and height as well as the 95% confidence intervals. The easting and northing coordinates are in terms of NZGD2000 North Taieri circuit with the height of each point in terms of NZVD 2016. NAL 1 – 6 are control points that were held fixed for the LSE adjustment and therefore have no horizontal or vertical LSE adjustment errors.

Point ID	Easting (m)	Northing (m)	Height (m)	Hor.Err (m) @ 95% C.I	Vrt.Err (m) @ 95% C.I
0001	417744.616	799089.470	6.872	0.011	0.001
0002	417739.803	799077.387	6.750	0.001	0.000
0003	417738.559	799073.954	5.567	0.002	0.001
0004	417736.304	799075.657	8.139	0.002	0.001
0005	417733.753	799064.409	7.628	0.004	0.001
0006	417733.023	799066.970	6.800	0.008	0.000
0007	417735.572	799072.488	7.748	0.006	0.002
0008	417735.052	799065.428	5.545	0.001	0.001
0009	417742.143	799089.624	7.337	0.005	0.001
0010	417743.565	799086.837	7.246	0.002	0.001
0011	417740.624	799085.792	5.827	0.002	0.001
0012	417742.309	799083.676	5.766	0.002	0.001
0013	417739.380	799082.664	7.967	0.002	0.001
0014	417741.441	799081.501	7.935	0.002	0.001
0015	417738.485	799080.418	6.825	0.001	0.000
0016	417740.526	799079.184	5.794	0.001	0.000
0017	417737.554	799078.063	8.002	0.002	0.001
0018	417740.573	799073.823	7.679	0.005	0.001
0019	417732.594	799078.098	7.934	0.005	0.001
0020	417737.327	799071.156	7.225	0.002	0.001
0021	417736.198	799074.626	6.647	0.004	0.001
0022	417736.446	799068.949	5.661	0.002	0.001
0023	417734.960	799071.537	5.825	0.003	0.001
0024	417735.820	799067.399	7.722	0.002	0.001
0025	417734.253	799069.789	7.702	0.004	0.001
0026	417729.720	799079.530	7.567	0.002	0.001
0027	417729.186	799073.753	7.947	0.002	0.001
0028	417724.626	799079.799	7.698	0.004	0.001
0029	417717.772	799080.770	7.819	0.006	0.001
0030	417724.665	799080.229	7.149	0.007	0.001
0031	417729.252	799079.741	6.972	0.002	0.000
0032	417731.886	799076.698	7.655	0.002	0.001
0033	417719.865	799074.963	7.930	0.002	0.001
0034	417726.977	799087.756	7.663	0.008	0.002
0035	417724.444	799075.627	7.045	0.002	0.000
0036	417727.101	799084.076	7.884	0.003	0.001
FRE1	417742.935	799087.319	5.223	0.002	0.001

FRE2	417742.345	799087.915	5.229	0.002	0.001
FRE3	417740.022	799081.356	5.238	0.001	0.000
FRE4	417737.256	799076.812	5.250	0.001	0.000
FRE5	417738.979	799076.030	5.225	0.001	0.000
FRE6	417724.799	799079.703	5.234	0.001	0.000
FRE7	417722.471	799079.971	5.224	0.002	0.000
FRE8	417734.870	799069.718	5.242	0.002	0.000
NAL1	417743.993	799092.451	5.200	Fixed	Fixed
NAL2	417738.776	799077.653	5.230	Fixed	Fixed
NAL3	417733.579	799065.450	5.220	Fixed	Fixed
NAL4	417730.314	799077.502	5.233	Fixed	Fixed
NAL5	417718.334	799080.392	5.252	Fixed	Fixed
NAL6	417727.590	799078.538	5.223	Fixed	Fixed

3.2.2 Registration

The surface to surface registration results showed an 'overall cloud-to-cloud error' of 2.68 mm using the surface to surface registration method in RealWorks. The report shows results from each scan station position with respect to each other scan station. A 'cloud-to-cloud error', 'coincident points', and 'confidence' are reported on. See Appendix A for the SoS registration report.

3.2.3 Georeferencing

Table 3.3 shows the mean and standard deviation of the difference in transformation parameters (translation and rotation) for each scenario with respect to T1. Results from the assessment show that deviations from the reference scenario (T1) occur more so when there is a shift in GCP location compared to the amount of GCPs used (Table 3.3). The table shows scenarios T2 and T3 involve marginal departure compared to reference scenario T1 with a mean translation of stations in the order of 1 mm and mean rotation of up to 5 mrad. However, scenarios T4-T9 exhibit much greater departure in horizontal and/or elevation direction, as well as substantial rotation. This demonstrates a distortion of the final model caused by poor configuration of the GCPs network.

Table 3.4 shows the Root Mean Square Errors (RMSE's) of all CPs, showing little difference between T1, T2, T3, and T9. Each of these test scenarios share three GCPs that cover the extent of the scan scene. This suggests placing the minimum number of GCPs (three) around the scan scene may render similar results to scenarios with more control. This also highlights that it is possible to achieve similar accuracies when there is a reduction in the number of scans

captured, as revealed by reference scenario T9. Comparing scenarios T4 - T8 shows an increase in RMSE for the scenarios with GCPs placed in unfavourable positions.

Table 3.5 shows the five largest individual residuals of a CP. All worst values originate from scenarios T4 and T5 thus supporting the significant distortion in the georeferenced models, due to unsuitable placement of GCPs.

Table 3.3. Mean (μ) and standard error (2σ) associated with translation vector (rX, rY, rZ) and rotation angles (rω, rφ, rκ) associated with each scenario. All translation values are in mm, angles are in mrad.

	rX		rY		rZ		rω		rφ		rκ	
Scenario	μ	σ	μ	σ	μ	σ	μ	σ	μ	σ	μ	σ
T2	0	1	1	1	0	1	-1	2	-1	5	-1	3
T3	0	1	1	1	-1	1	0	0	1	1	-2	3
T4	-1	1	2	2	19	24	-23	15	16	16	4	3
T5	-8	15	9	11	-1	8	5	3	-6	5	36	31
T6	-2	1	3	2	-5	3	3	20	60	26	6	4
T7	2	3	-5	4	18	17	-6	20	40	21	5	3
T8	1	2	-3	3	5	7	-2	18	52	24	4	3
T9	-4	5	5	5	4	1	-41	1	66	0	13	17

Table 3.4. Root mean square error on the set of 31 checkpoints from each scenario. Values in mm.

Scenario	**T1**	**T2**	**T3**	**T4**	**T5**	**T6**	**T7**	**T8**	**T9**
rX	4	4	4	4	9	3	4	3	4
rY	3	3	4	7	3	10	6	11	4
rZ	4	4	4	14	6	5	7	5	4

Table 3.5. The five largest residuals for an individual checkpoint. Values in mm.

Scenario	**T4**	**T4**	**T5**	**T5**	**T4**
rX	1	4	33	32	2
rY	11	14	1	6	16
rZ	38	34	16	13	27
rXYZ	23	22	21	20	18

A graphical representation of CP differences for the various scenarios is seen in Figure 3.8. The figure shows apparent systematic errors for scenarios T4 - T8. T4 displays a shift in the horizontal plane of all CPs toward the GCP baseline, with the magnitude of these horizontal errors increasing with distance from the GCPs, a sign of increasing error propagation. The vertical plane shows a rotation from a positive to negative difference from west to east as the CPs approach the GCP baseline. T5 displays horizontal errors that rotate about the GCPs and increase in magnitude with an increase in distance from the GCPs. In the vertical plane, it

appears as though similar characteristics to T4 are seen, where there is a change from positive to negative differences. T6 and T7 display similar characteristics to T4, whereby the error of each CP appears to increase in size with an increase in distance from the GCP baseline. T8 has a cluster of GCPs like T5 and shows similar distortion of the final CPs. This supports the placement of GCPs over the quantity of GCPs used.

3.2.4 3D root mean square error as a function of range from GCP centroid

Figure 3.9 shows the 3D RMSE as a function of range from the GCP centroid. The centroid is defined here as the centre of the GCPs used in each georeferencing scenario and was calculated by taking an average of each fixed GCP. Scenarios T1, T2, T3, and T9 show consistent RMSE regardless of the range from the GCP centroid, supporting that the placement of GCPs are more relevant for accuracy than for the quantity of GCPs used. Scenarios T4-T8 show a significant correlation between the RMSE and range from the GCP centroid. An RMSE per metre increases from 0.3 mm in scenario T1 to a maximum of 4.8 mm per metre in scenario T5, highlighting a significant share of the error variance being attributed to the placement of GCPs in a scan scene. Considering error propagation over long distances, where no control is fixed, large uncertainties occur in the position of the point cloud. Thus, where hundreds of scans are registered together, it is recommended that distances are reduced between the placement of GCPs in order to increase point cloud accuracies. The results of T4-T8 suggest that without establishing a favourable GCP network, the point cloud "floats" similarly to a hanging traverse that may suffer from error propagation along a series of registered scans. With each additional scan from the fixed GCPs additional uncertainty is added to the point cloud model

Figure 3.10 is a depiction of the RMSE standard deviation as a function of range from the GCP centroid. The graphs show a strong correlation between the RMSE standard deviation and the range from the GCP centroid, particularly in scenarios T4, T5, and T6. Interestingly, T9 shows a high correlation between the RMSE standard deviation and the range from the GCP centroid. This result may be possible because there was a reduction in the number of scans for T9 and therefore the number of observations made to each target, i.e. redundancy, was reduced, therefore creating larger uncertainties in the accuracies.

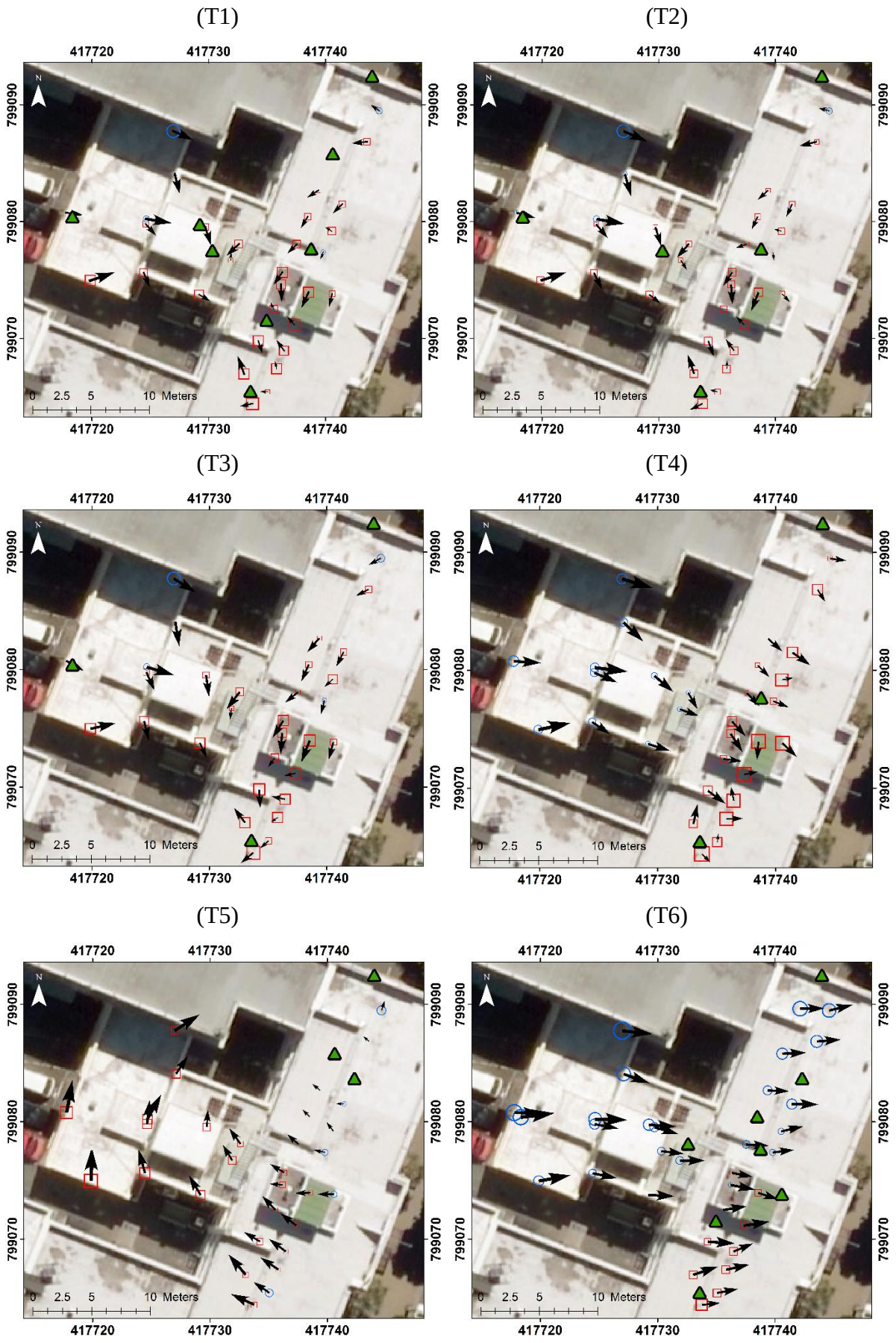

Figure 3.8. Checkpoint root mean square errors for tested GCP scenarios. Note the systematic distortion associated with scenarios T4-T8.

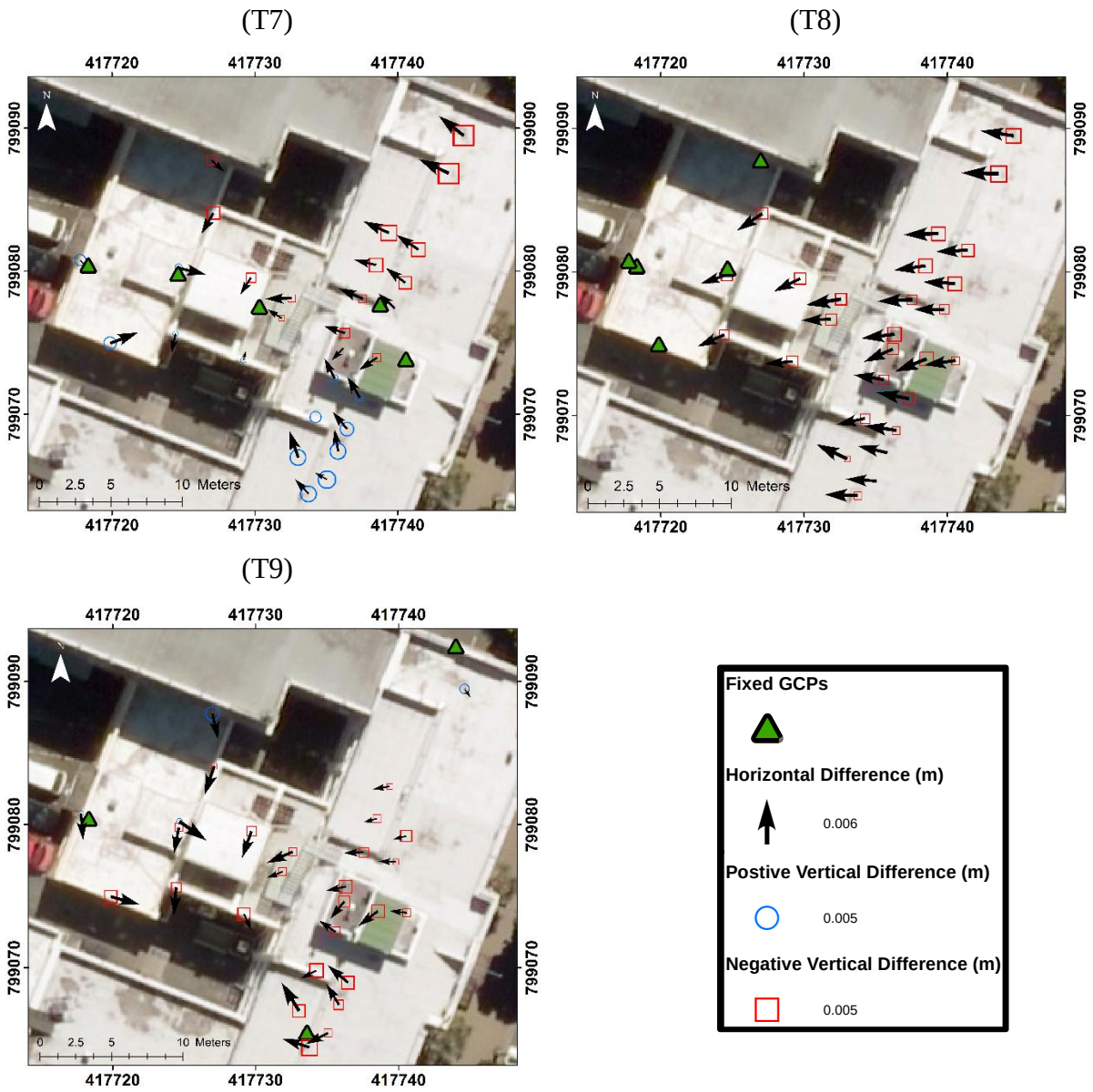

Figure 3.8. (Cont.). Checkpoint root mean square errors for tested GCP scenarios. Note the systematic distortion associated with scenarios T4-T8.

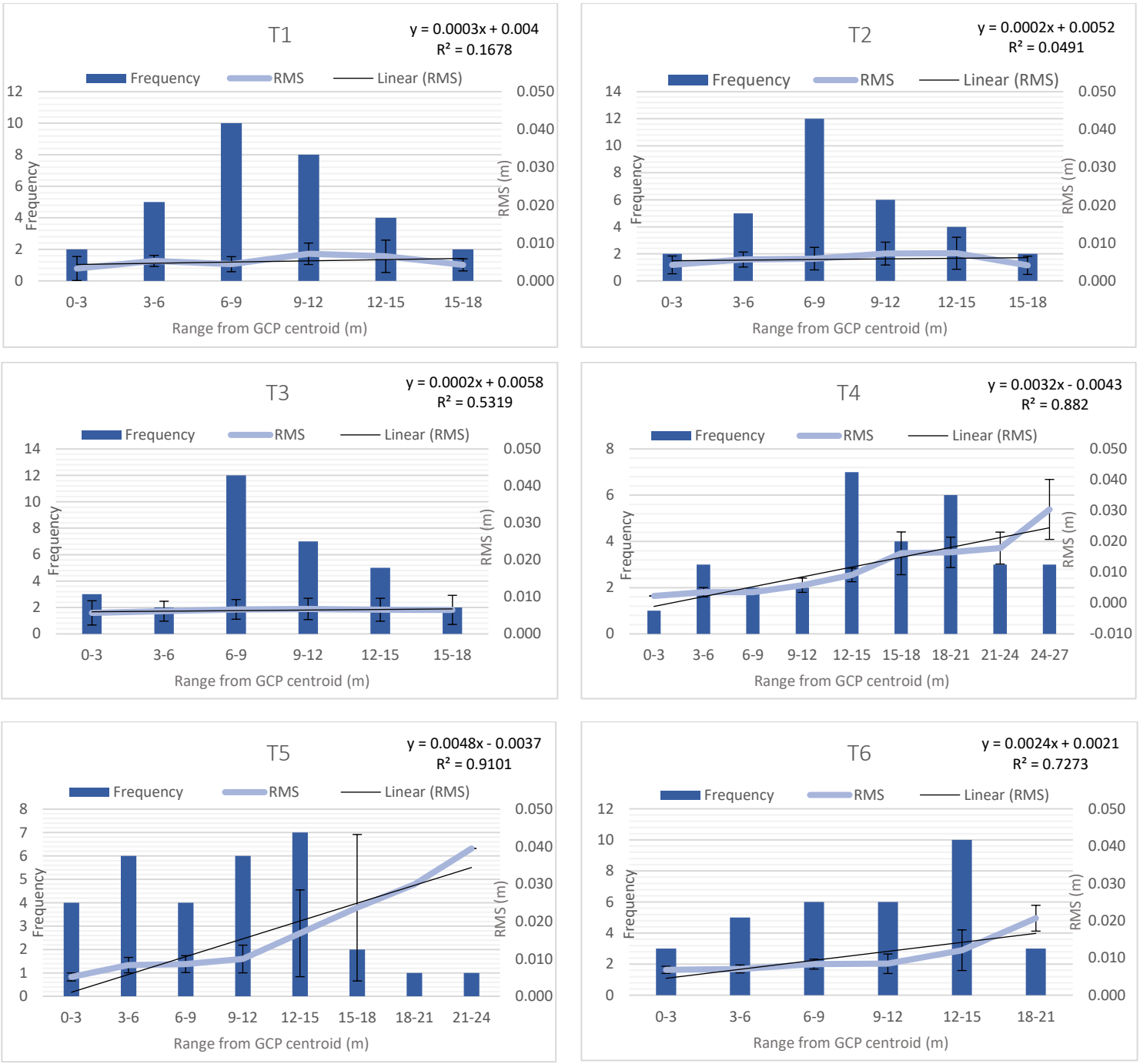

Figure 3.9. 3D RMS error as a function of range from GCP centroid for each scenario. Scenarios T4-T8 showing significant correlation between an increase in error with an increase in range from GCP centroid.

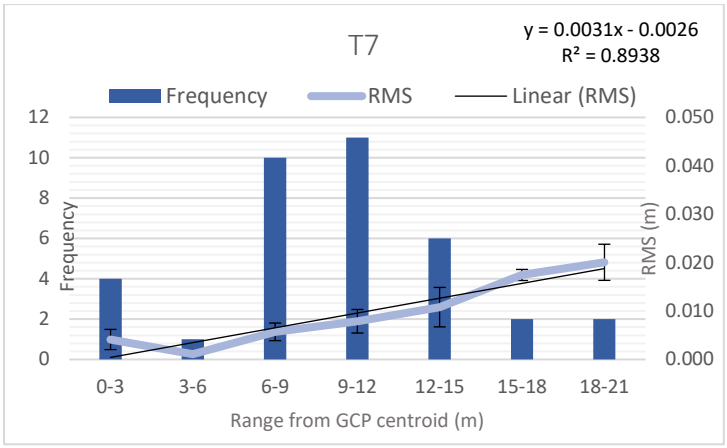

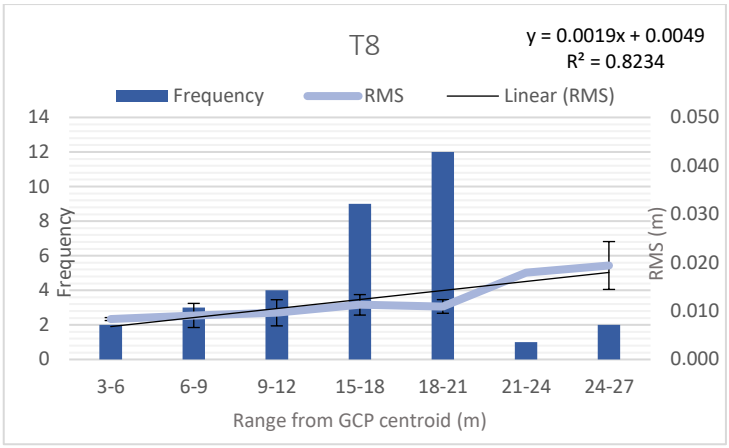

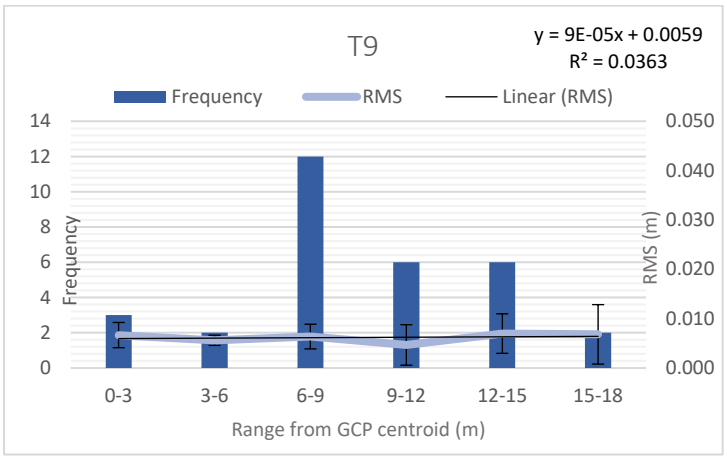

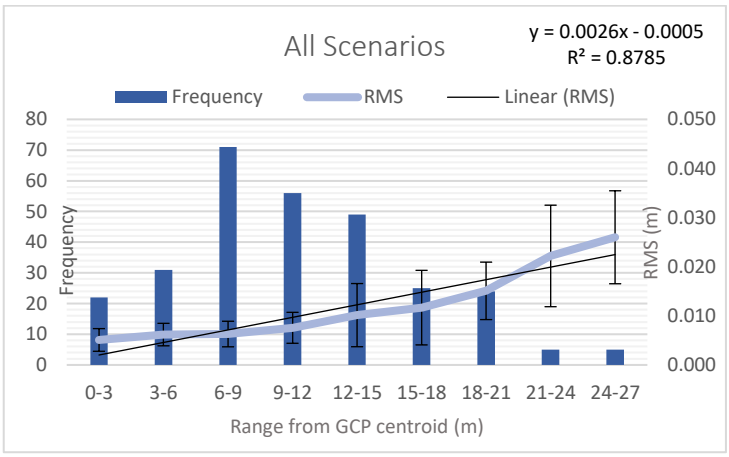

Figure 3.9. (Cont.). 3D RMS error as a function of range from GCP centroid for each scenario. Scenarios T4-T8 showing significant correlation between an increase in error with an increase in range from GCP centroid.

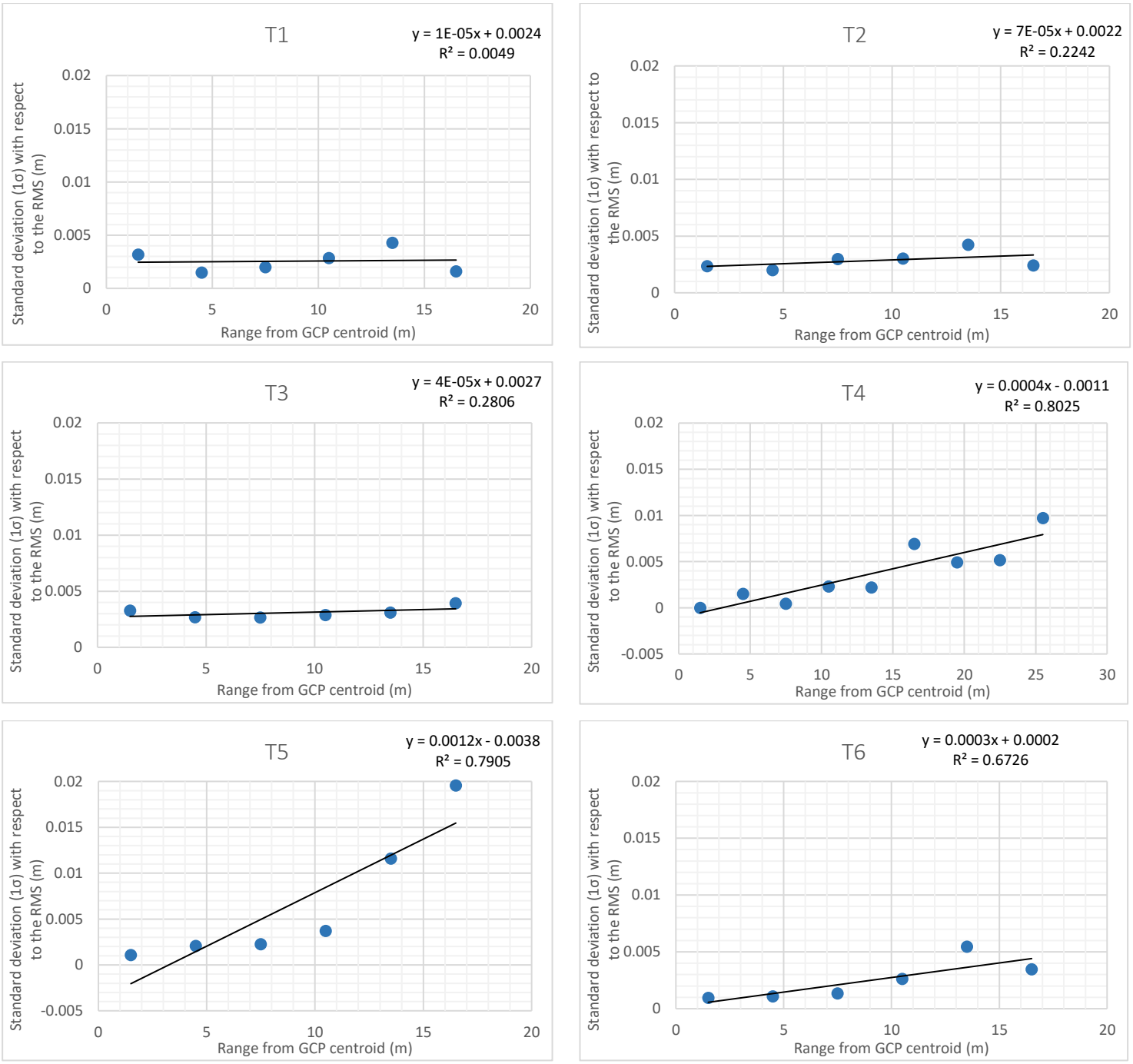

Figure 3.10. Standard deviation as a function of the range from GCP centroid.

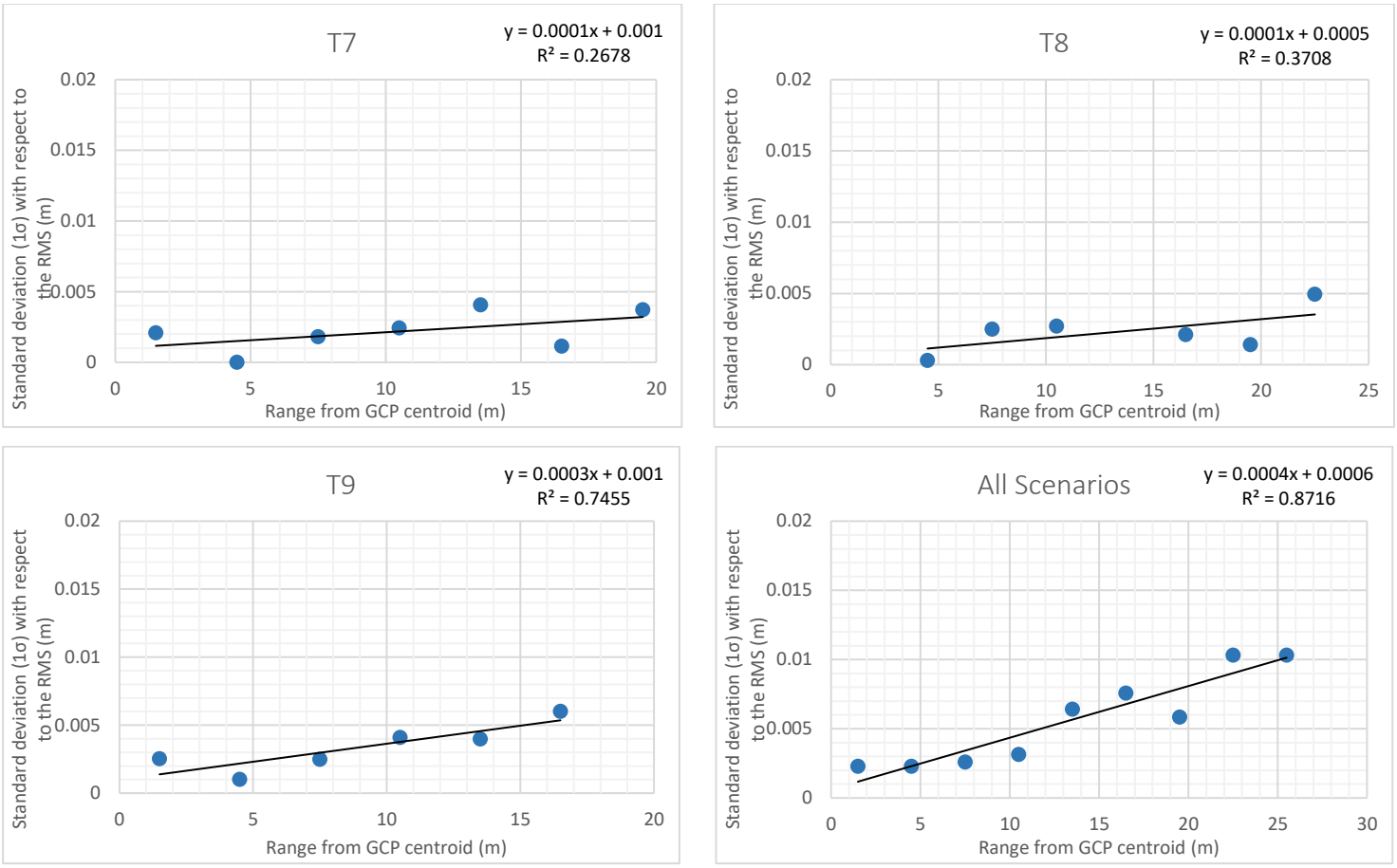

Figure 3.10. (Cont.). Standard deviation as a function of the range from GCP centroid.

Table 3.6 is a summary of the graphs shown in Figure 3.9 and Figure 3.10 where it is demonstrated that the RMSE error is mitigated when the spatial extent of the scan scene has adequate GCP coverage. The use of 3 GCPs shows no degradation to the overall accuracy of the point cloud data compared to 8 GCPs, when placed spatially around the scan scene. While the SoS results show little difference between T1, T2, and T3, it should be noted that it is possible for inaccurate georeferenced models to occur as a by-product of a low redundancy solution (Figure 4.11 and Figure 4.12). This is evidenced in Chapter 4 where the case study required considerably more GCPs to attain similar accuracies to the tests undertaken at the SoS (Figure 4.8). Test scenarios T4-T8 show an increase in RMSE between 1.9 mm to 4.8 mm for every metre increase in range from the GCP centroid. This reflects the importance of mitigating the range between GCPs where it is not possible to have a favourable network of GCPs, such as tunnelling situations. The RMSE standard deviation does appear to increase when there is a spatially poorer configuration of GCPs (T4-T8). Therefore, the placement of GCPs can mitigate the RMSE range dependent errors and standard deviations where there is an increase in distance from the GCP centroid.

Table 3.6. A summary of each scenarios maximum ranges from GCP centroid, maximum RMSE, the increase in RMSE per metre, maximum standard deviation, and the increase in standard deviation per metre.

Scenario	Max Range from GCP Centroid (m)	Max RMSE (m)	RMSE Increase per metre (m)	Max Std. Deviation (1σ) (m)	Std. Deviation Increase per metre (m)
T1	15-18	0.007	0.00030	0.0043	0.00001
T2	15-18	0.007	0.00020	0.0042	0.00007
T3	15-18	0.007	0.00020	0.0039	0.00004
T4	24-27	0.030	0.00320	0.0097	0.00040
T5	21-24	0.039	0.00480	0.0196	0.00120
T6	18-21	0.021	0.00240	0.0055	0.00030
T7	18-21	0.020	0.00310	0.0041	0.00010
T8	21-24	0.019	0.00190	0.0049	0.00010
T9	15-18	0.007	0.00009	0.0060	0.00030

3.3 Chapter summary

This chapter summarised the methodologies that were implemented in this study, where a control network was established using traditional surveying techniques (total station); a TLS survey was performed, considering various GCP scenarios that used more, less, and spatially variable control; and scenarios were tested with less scan data.

The tested scenarios signify the importance of GCP placement. Clear systematic errors are noted when GCP placement does not spatially cover the extent of the scan scene. There appears to be little difference associated with the number of GCPs used, if they are suitably placed around the scan scene. Significant errors can be generated due to unsuitable geometry of the GCP network. The correlation between an increase in RMSE and an increase in range from the GCP centroid becomes clearly apparent with unfavourable GCP placement. When GCPs are placed suitably, the correlation between the RMSE of each CP and an increase in range from the GCP centroid decreases, suggesting that the range between each GCP can be increased should the geometry of GCPs cover the extent of the scan scene.

The scan scene area should be considered when deciding the required amount of GCPs. The scan scene geometry and dataset size used in this research has shown favourable point cloud accuracies when georeferencing using three GCPs, scenario T3. For larger datasets, further GCPs may be required to achieve specific accuracies and limit error propagation. Consideration should also be given to the range between GCPs and, where possible, they should cover the exterior of the area being captured. Minimising this range and providing an even coverage of GCPs should allow the point cloud georeferencing errors to be mitigated. The test at the SoS

was necessary to better understand achievable accuracies when designing the LiDARRAS project control network and ways in which point cloud errors may be mitigated.

Chapter 5 is a case study where the results found from the research at the SoS were applied. The case study involved collecting 967 scans to document part of the Ronville Tunnels in Arras, France.

Chapter 4 Case study: LiDARRAS

4.1 Introduction

An existing series of 17th century underground quarries were linked together during the First World War by the New Zealand Engineering Tunnelling Company (NZETC). Known as the Ronville Sector, the underground network extended from the town square to the front line (Figure 4.1). This little-known and poorly mapped underground system of tunnels of Arras in Northern France represents a permanent but unseen memorial to the brave and industrious actions of the NZETC.

The tunnels presented an opportunity for soldiers to pass underground and approach the front line safely. The tunnel system included its own light rail system, kitchens, toilets, running water, electric lights – even its own hospital - and provided troops safe refuge from heavy German bombardment of the town and allied positions. The subterranean network was able to accommodate up to 24,000 soldiers in the lead up to the battle of Arras, in April 1917.

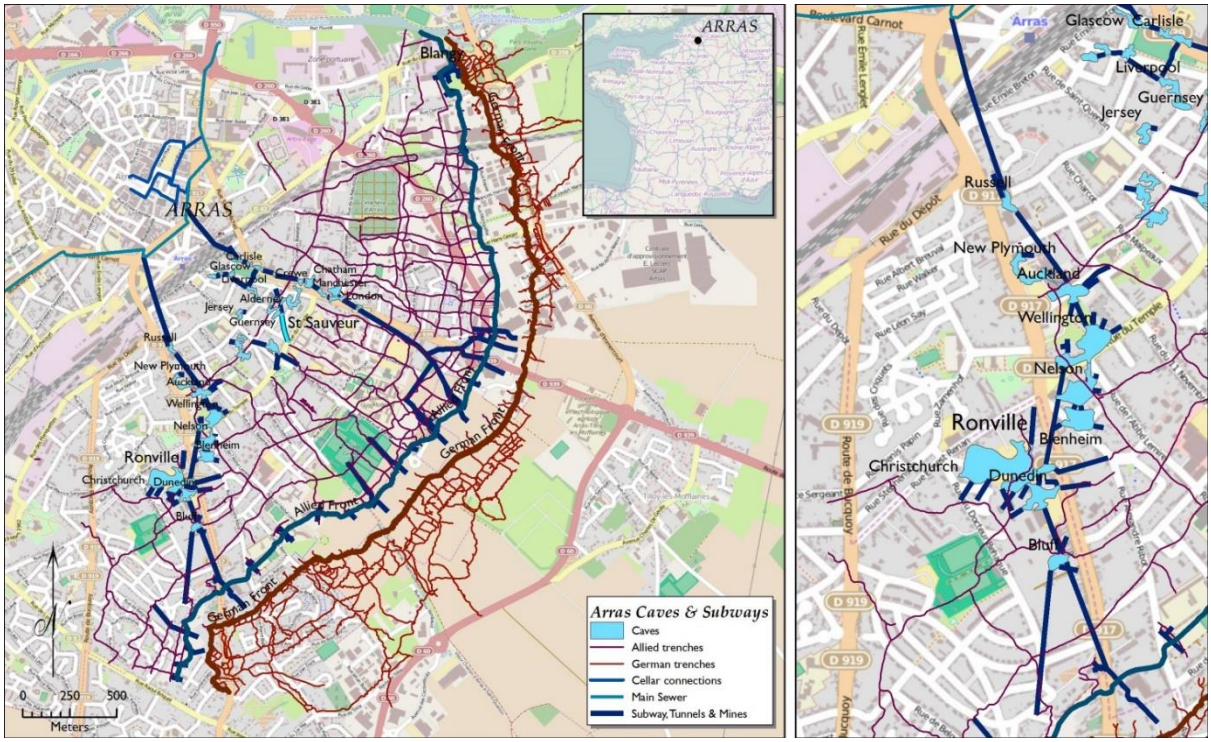

Figure 4.1. (left) Caves, subways, and trenches during World War 1 in Arras, France, (right) Connected quarries of the Ronville sector. Source: Sirguey, pers com.

For years after the World Wars the tunnels remained closed and largely forgotten. They were rediscovered in the 1990s and an underground museum built around the central Wellington quarry (Carrière Wellington). The Carrière Wellington museum opened in 2008 and welcomes nearly 50,000 visitors a year who can safely access the Wellington, Nelson, and Blenheim

Quarries. However, even now the remaining tunnels and quarries remain uncharted and largely inaccessible to the public.

The project's aim was to survey and accurately document these tunnels using modern surveying technologies and visualisation techniques in order to create a permanent record of this New Zealand contribution to the war in France, which would be accessible to a wider audience. These surveys were largely based around the Wellington, Nelson, and Blenheim Quarries. To carry out this TLS objective and accurately document in 3D, an established control network and set of Ground Control Points (GCPs) were used (Figure 4.4 and Figure 4.5).

Chapter 3 examined various georeferencing scenarios and their effects on point cloud accuracy. These scenarios allowed for appropriate implementation of GCPs throughout the Arras heritage site, which will be discussed in this chapter. The scope of the fieldwork in France made it necessary to determine suitable protocols and achievable accuracies prior to commencing the TLS survey.

The first section of this chapter discusses the methodologies of establishing the underground control network and conducting the TLS survey. The results of these are analysed with various TLS georeferencing scenarios being analysed.

4.2 Methods and data

4.2.1 Control network

The control network for the LiDARRAS project was established using various traditional surveying techniques and two different surveys. An initial pilot survey was completed in November 2015, with the first control network being established in the Wellington Quarry. The network was extended into the Nelson and Blenheim Quarries in June 2016, during the second fieldwork. The control network was coordinated in terms of a regional projection of the French Geodesic System RGF93; the Conformal Conic Zone 9 (CC50).

GNSS was used to coordinate the outside control marks, using the central pivot method. This method uses two receivers, one that is static for the entire observation session and the other taking measurements over 15-20 minute intervals. The data is post-processed in two steps; first the centre pivot position is calculated using a network of continuous GNSS stations with approximately 30-40 km baselines. For this control network the continuous stations Beauvois (BVOI), Doullens (DOUL), and Merignies (PEVL) were used. Secondly, the calculated centre pivot position is used to calculate the remaining GNSS positions. The GNSS computations

were made using the Leica LGO software suite. The final 3D accuracy of the calculated points was ±2 cm (Ferré, 2016).

The network was extended underground using a Leica TCR1201, having an angular precision of 1". This was initially extended into the Wellington Quarry during fieldwork 1, and then into the Nelson and Blenheim Quarries during fieldwork 2. A Least Squares Estimation (LSE) adjustment was completed using the survey software adjustment program COVADIS (Ferré, 2016). Each position's coordinates as well as horizontal and vertical uncertainties are shown in Table 4.1. The closed loop traverse for fieldwork 1 is seen in Figure 4.2. The position "WELL.1" involved descending 2.5 m down a manhole in the museum carpark, which gave access to an old tunnel leading to the Auckland Quarry. The emergency exit was used to traverse out of the quarry and back to the surface where the point "WELL.2" was intervisible with point "WELL.1", forming the closed loop traverse.

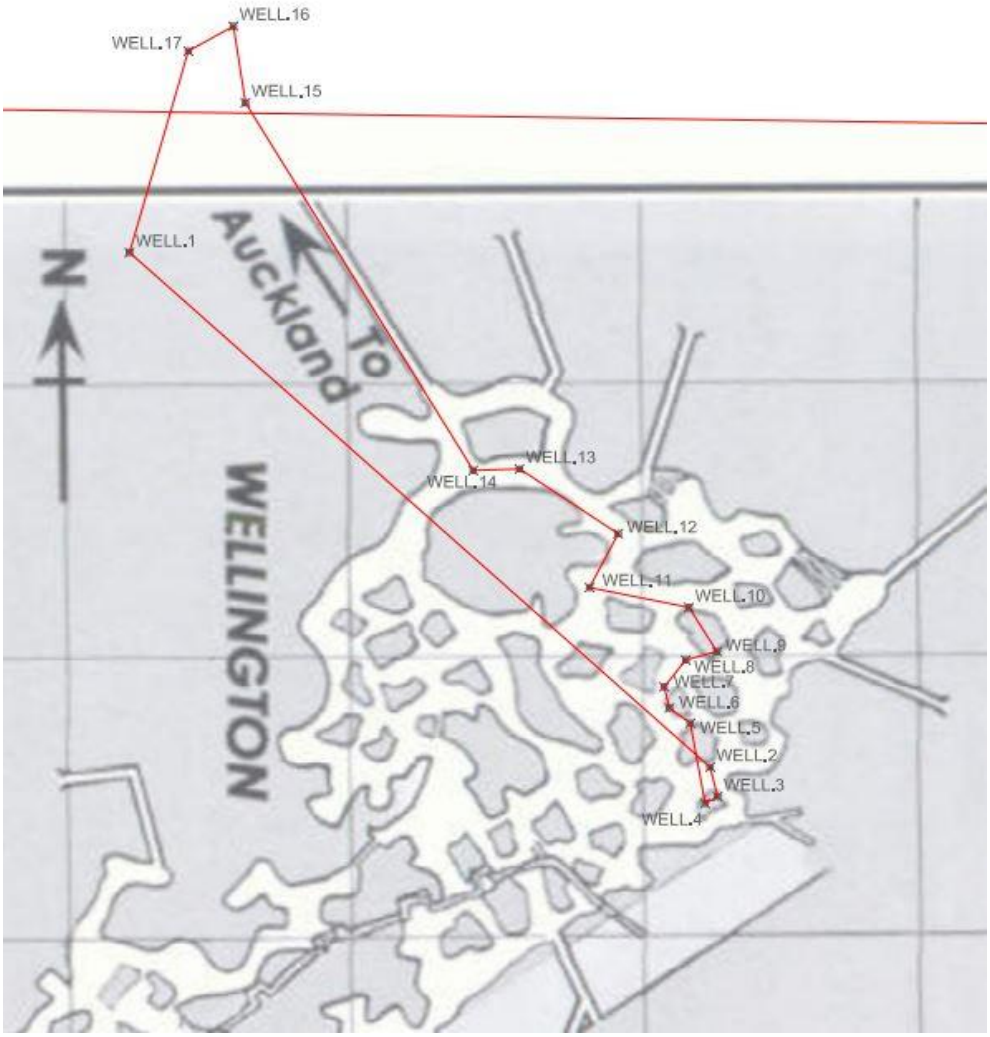

Figure 4.2. Closed loop traverse as completed during fieldwork 1. Source: Ferré, 2016.

The second fieldwork traverse extended through the Nelson and Blenheim quarries, closing on point “W320” (Figure 4.3). Point W320 involved descending approximately 15 m vertically down a manhole off the street. Hence, W320 is a point located on the surface. It was measured using GNSS and used the existing GNSS surface control to close on.

Figure 4.3. The extended traverse, which was completed during Fieldwork 2. Source: Ferré, 2016.

We encountered several difficulties during the establishment of the control network. Forming a closed loop for the traverse work required deep vertical plummets, short traverse legs, and working in the dark. Particular methodologies therefore had to be implemented. To overcome the issue relating to darkness, all total station observations were made using the method of forced centering. This method changes station positions without moving the tripod or tribrach. The instrument and prisms are moved to each tripod and tribrach position, mitigating any plumbing errors. Left and right face observations were made to reduce any systematic pointing errors. Nadir and zenith plummets were used for the vertical descents down each manhole.

Point W320 required particular effort, as a small rotation of the of the vertical axis on the surface had substantial deviations 15 m below.

Figure 4.4. Ground control points used to georeference the underground quarries.

Figure 4.5. Ground control points used to georeference the streetscape.

Table 4.1. The network point uncertainties at the 95% confidence interval. Positions shown as "fixed" were used to coordinate subsequent points and are assumed to have no error. Where points show "N/A" for the vertical uncertainties, no LSE adjustment was computed and the 4cm misclose distributed evenly between each mark.

Point ID	Hor.Err (m) @ 95% C.I	Vrt.Err (m) @ 95% C.I	Point ID	Hor.Err (m) @ 95% C.I	Vrt.Err (m) @ 95% C.I
WELL01	0.007	N/A	**N108**	0.020	0.006
WELL02	0.004	N/A	**N109**	0.018	0.006
WELL03	0.004	N/A	**B101**	0.014	0.006
WELL04	0.004	N/A	**B102**	0.013	0.006
WELL05	0.004	N/A	**W301**	0.002	0.002
WELL06	0.004	N/A	**W302**	0.008	0.004
WELL07	0.004	N/A	**W303**	0.008	0.005
WELL08	0.004	N/A	**W304**	0.010	0.005
WELL09	0.004	N/A	**W305**	0.013	0.006
WELL10	0.004	N/A	**W306**	0.013	0.006
WELL11	0.005	N/A	**W307**	0.014	0.006
WELL12	0.005	N/A	**W308**	0.014	0.006
WELL13	0.006	N/A	**W309**	0.016	0.006
WELL14	0.006	N/A	**W310**	0.017	0.006
WELL15	0.008	N/A	**W311**	0.019	0.006
WELL16	0.009	N/A	**W312**	0.018	0.006
WELL17	0.009	N/A	**W313**	0.018	0.006
WELLGPS1	Fixed	Fixed	**W314**	0.017	0.006
WELLGPS2	Fixed	Fixed	**W315**	0.016	0.005
WELLGPS3	Fixed	Fixed	**W316**	0.014	0.005
N102	0.017	0.006	**W317**	0.013	0.004
N103	0.018	0.006	**W318**	0.012	0.004
N104	0.017	0.006	**W319**	0.008	0.003
N105	0.021	0.007	**W320**	Fixed	Fixed
N106	0.022	0.007	**W102**	0.008	0.005
N107	0.020	0.007	**W106**	0.009	0.005

4.2.2 TLS data capture

Data was captured during two fieldwork stages; November/December 2015 and June/July 2016. Each of the fieldwork campaigns are discussed in the subsequent sections.

4.2.2.1 Fieldwork 1

The initial pilot survey, fieldwork 1, sought to establish the feasibility of completing the larger project objectives. The Wellington, Nelson, and Blenheim Quarries were explored and the initial control network established. The collection of TLS data began with scanning as much

of the Wellington Quarry as possible. This sequencing of the quarries was preferred, as the Wellington Quarry is open to the public, with guided tours happening throughout the day. During summer, tours occur every 15 minutes, providing little opportunity to scan uninterrupted. Given this, the Wellington Quarry was scanned predominantly during fieldwork 1, in winter. A summary of the collected scans is shown in Table 4.2.

Table 4.2. Number of completed scans from fieldwork 1.

Instrument	TX8	TX5	Combined
# of Scans	162	67	229

To summarise, fieldwork 1 was a success. The project objective to scan Wellington, Nelson, and Blenheim Quarries proved feasible with the majority of Wellington being scanned during this initial pilot survey.

4.2.2.2 Fieldwork 2

Fieldwork 2 was completed between June and July 2016. Scanning began in the Nelson Quarry and progressed systematically day-by-day towards the end of the Blenheim Quarry. Once these two quarries had been documented, other areas of the underground network were explored. The Auckland Quarry, which was not part of the project objectives, was also documented. Due to Auckland, not being part of the project objectives because of initial safety concerns, the control network was not extended into this particular quarry. The streetscape was also documented to provide context about where the quarries were in relation to surface features. Table 11 shows the amount of completed scans during fieldwork 2.

Table 4.3. Number of completed scans for fieldwork 2.

Instrument	TX8	TX5	Combined
# of Scans	652	86	738

A total of 967 scans were completed during the course of fieldwork 1 and 2. We were able to document more than the specified Wellington, Nelson, and Blenheim Quarry areas by scanning Auckland Quarry, the streetscape, and tunnels heading towards New Plymouth and Russell Quarries.

4.2.2.3 Instrumentation

The Trimble TX8 and TX5 laser scanners were used to perform the TLS survey. The instrument specification sheets are included in Appendix B. The TX8 was the primary instrument used with the TX5 being used to scan in areas where distances from the scanner position to measured surfaces were less than a metre. This was done as it appeared as though the TX8 did not return a reliable signal for these short distances.

The resolution for the TX8 was set at 11.3 mm at 30 m, which resulted a scanning time of 3:00 minutes and a point cloud size of 128 million points. Unlike the TX5, the TX8 does not have an internal camera. To colourise the point cloud, a Nikon D7100 external camera with a fisheye lens was utilised to capture imagery at 90° intervals (Figure 4.6). A fish eye lens was used in order to create overlap between photos, forming a single panorama at each scan station. Three different exposures were captured from a particular orientation, with a total of 12 individual photos used to colourise a single scan station point cloud. Figure 4.7 shows an example of four individual photos at different orientations used to create a single panorama. Light was needed to illuminate the scan scene as all of the quarries, other than Wellington Quarry, were in complete darkness. Portable battery powered spotlights (Figure 4.7) were placed under each scan station tripod and out of sight in order to reduce the amount of clean up during post-processing. The TX5 had a resolution of 7 mm at 10 m, where most surfaces were close to 1 m away, as the TX5 was used in tunnels that joined the quarries together.

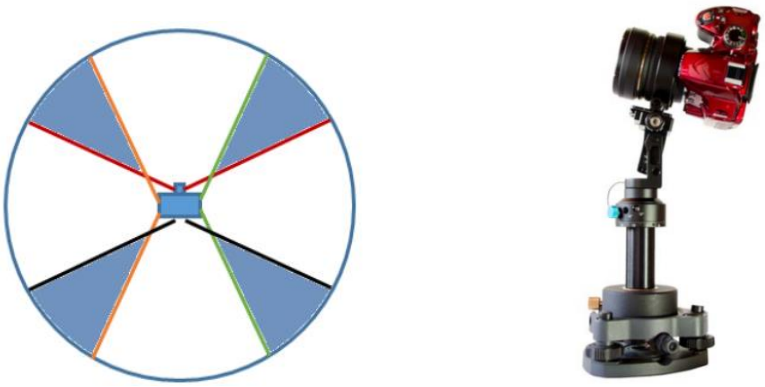

Figure 4.6. Left, Schematic showing 90° intervals of camera orientation. The shaded blue area depicts overlap required to stitch individual photos together. Right, an example of the camera setup used to colourise the TX8 point cloud data. Source: www.geotronics.sk

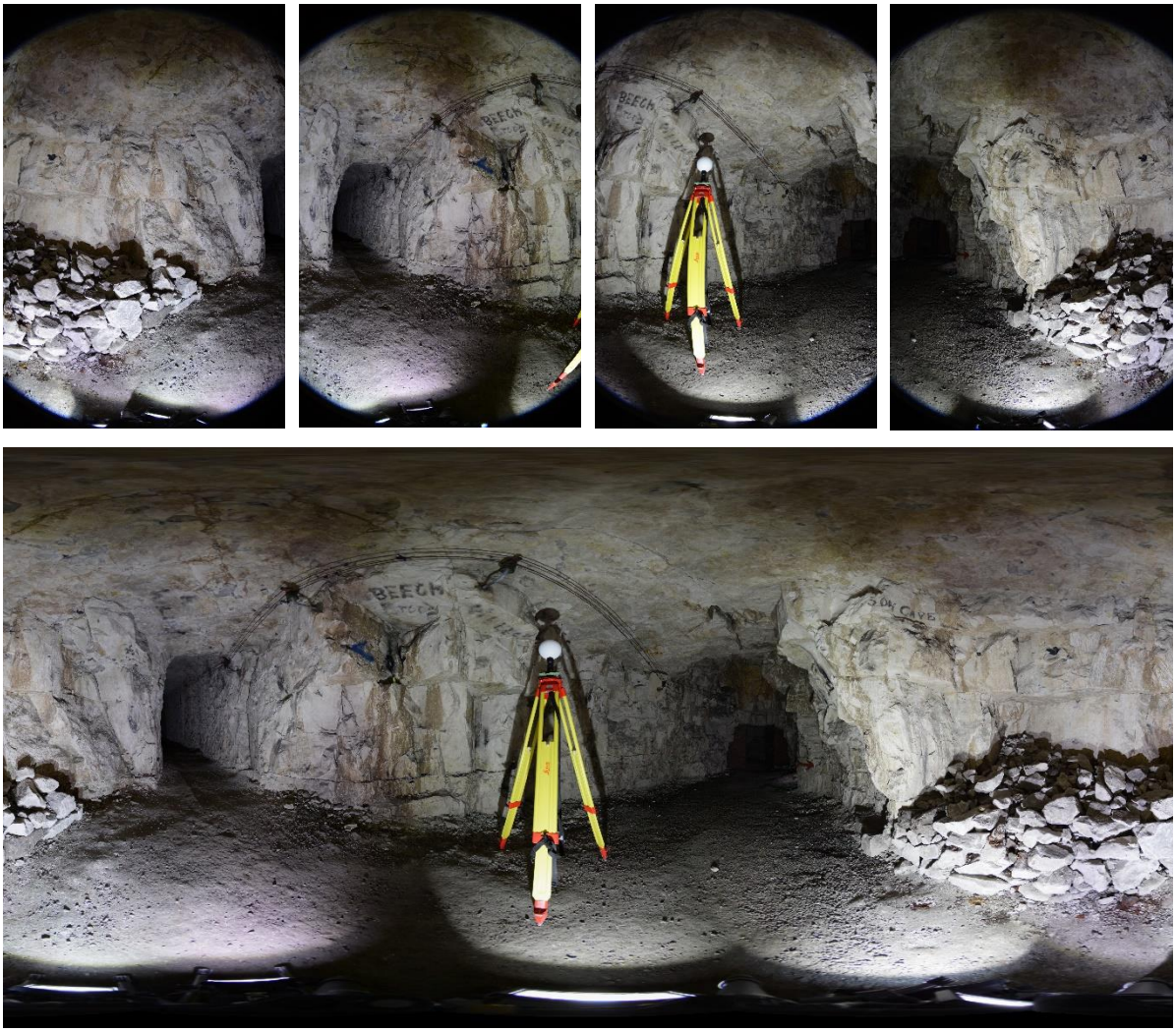

Figure 4.7. Individual photos (top) and a single panorama after stitching (bottom).

Targets were placed over a series of marks coordinated from the control network. Targets were in the form of spheres, as these have been shown to provide the highest accuracy in previous literature. 200 mm and 139 mm diameter spheres were used, and heights were recorded to the centre of the sphere. The purpose of placing targets over a series of known points is to coordinate the point cloud data in terms of a real world coordinate system. This is referred to as georeferencing, which allows data fusion with other techniques, and also allows the combination of temporally separate datasets. All marks used to georeference the point cloud data are seen in Figure 4.4 and Figure 4.5.

4.2.3 Data processing

After each day of fieldwork, the data were catalogued by date, with individual scan names indicating the quarry that they were created in. For example, if a scan occurred in Wellington Quarry the tzf file would be “01_07 Wellington Station 001 Scan 01.” Individual photos were

downloaded from the external camera and filed under the same folder as the tzf files from that day. The tzf file format is the standard Trimble proprietary scan file format.

4.2.3.1 Post processing scans

Trimble RealWorks v10.1 was used to process the scan data. The TX8 produces a tzf file that can be imported directly into the software, while the TX5 fls file must be converted to a tzf file before any processing can occur. The tzf scan files were registered using an automatic surface to surface registration process using point cloud overlap, the RealWorks function being "Auto-register using Planes" tool. The surface to surface registration function was employed due to time constraints and was based on the preliminary School of Surveying (SoS) results. The registration technique does not require users to place discrete targets throughout a scan scene, which would have been time intensive in the underground network of tunnels. The registration results from the School showing precise results where the overall fit of the scans using the surface to surface registration being 2.68 mm. Scans were initially registered after each day to ensure data quality. Should registration have failed, supplementary scans would have been collected.

4.2.3.2 Colourising TX8 scans

The imaging software, Kolor Autopano Giga, was used to create a panorama for each TX8 tzf scan. All photos can be individually imported with automatic rendering of panoramas created by the software package. This was found to produce errors when areas in the quarries did not have unique geometries. To reduce any error, each of the 12 photos associated with a scan station were imported as a group. The software would only use these 12 photos to render a panorama. This process was completed for all TX8 scans.

The RealColor function in RealWorks was used to colourise individual scans. The process was done automatically by importing every scan and panorama, with the software matching the two. Every scan was checked manually to ensure the process had worked correctly.

4.2.3.3 Registration

Upon completing both fieldwork campaigns, scans were registered by individual quarry. The automatic registration function was used in RealWorks. The registered point cloud data was inspected for any erroneously registered scans. Any incorrectly registered scans were corrected using the manual registration function, called "Cloud based Registration" in RealWorks. This function allows the user to pick common tie points in overlapping scans to register point clouds together. Once Wellington, Nelson, and Blenheim Quarries were registered, they were

registered together using the same manual registration function. This process worked by moving Wellington, Nelson, or Blenheim Quarry as a rigid point cloud and registering it with respect to the other quarries. Thus, none of the previous automatic registration is affected. The streetscape was automatically registered on its own and was not registered to the underground point cloud due to insufficient overlap.

4.2.3.4 Georeferencing

The fully registered point cloud was georeferenced using the GCPs shown in Figure 4.4 and Figure 4.5. This scenario, whereby all available surveyed points are used as control, is referred to as A1, and was used for the final georeferencing of the underground quarries. Targets were automatically "extracted" by RealWorks using the "Auto-extract Targets" tool. The software creates a target geometry for each sphere seen in every scan, meaning the software will create three targets for a given sphere if seen in three scans. Georeferencing in RealWorks allows the user to select one of the extracted targets created. A coordinate text file was imported to georeference the point cloud data. The final RMSE for each GCP is shown in Figure 4.8 and Table 4.5). The overall 3D RMSE for the combined georeferenced point cloud is 12 mm.

Other georeferencing scenarios were tested to make comparisons to the tests undertaken at the SoS and to characterise potential propagation of errors in the underground model (Table 4.4). These tests included:

- (A2) Georeferencing individual quarries separately to determine whether point cloud extents had an influence on accuracy,
- (A3) A final test with no control fixed in Wellington Quarry,
- (A4) Using three GCPs in Blenheim Quarry to highlight error propagation over large extents and,
- (A5) Using the same three GCPs with an additional GCP on the opposite end of the scan scene to determine if this would mitigate any errors cause by increasing range.

The reason for holding no fixed positions in Wellington Quarry was due to the fact that only a single side of the underground quarry had control points and by holding no control fixed inside the quarry, while fixing all other GCPs, this gave an indication of what error to expect in the areas of no control. As time was limited and this was not a test project, the luxury of establishing a similar network of check points to the SoS was not feasible. Because of this, various scenarios tested have evaluated the RMSE of fixed GCPs used in the LSE adjustment

when georeferencing. The evaluation of scenarios A3-A5 evaluate the RMSE of remaining unfixed positions, replicating CPs similarly to the previous chapter.

Table 4.4. Various georeferencing scenarios tested in the underground network of tunnels.

Scenario	Scenario Description
A1	Every GCP held fixed (Figure 4.4)
A2	Each quarry georeferenced individually using the same control as A1
A3	All GCPs fixed, as with A1, except for Wellington
A4	3 GCPs fixed in Blenheim
A5	3 GCPs fixed in Blenheim and 1 in Wellington tunnel to Auckland

4.3 Results

4.3.1 Registration

The registration report produced by RealWorks, as seen in Appendix A for the SoS, shows an overall fit of the registration. The report shows how each scan station relates to every other scan in the adjustment, reporting on the cloud-to-cloud error, coincident points, and the confidence that the scans match. For the underground registration adjustments, each had in excess of 150 scans, with the registration report being hundreds of pages long as a result. The registration reports have therefore not been included. The overall fit for each of the adjustments are as follows, Blenheim Quarry 3.90 mm, Nelson Quarry 4.60 mm, and Wellington Quarry 12.85 mm. The result for Wellington Quarry is due to scans not registering correctly in areas, where manual interaction was required to correct this result. Blenheim and Nelson Quarries show similar results to the automatic surface to surface registration of the SoS.

4.3.2 Georeferencing

Scenario A1 was used for the final deliverable accuracies, utilising each of the captured GCPs. The other scenarios were used to make judgements on the potential error outside of the area of fixed GCPs, i.e. in Auckland Quarry where it was not initially part of the anticipated deliverable due to safety concerns, and therefore the control network was not extended into the Auckland quarry.

Table 4.5 is the final residuals for each of the GCPs used in scenario A1, the overall RMSE being, 10 mm, 7 mm, and 9 mm in the X, Y, and Z components respectively. The largest 3D residual was 30 mm for point N109. This point had an uncertainty of 18 mm and 6 mm in the horizontal and vertical respectively, at the 95% C.I. for the control network adjustment (Table 4.1). The point was only captured in two scans, whereas other scans had more TLS

observations. These reasons may explain the larger residuals for point N109. Figure 4.8, which is a visual representation of the A1 georeferencing adjustment, shows no obvious outliers or systematic errors; an expected result based on the prior tests. Figure 4.13 shows that there is little evidence to support a correlation between RMSE and range from the GCP centroid. Similar to the tests at the SoS, where control was placed around the scan scene, errors related to range from the GCP centroid are mitigated. The standard deviation shown in Figure 4.14 shows a correlation to the range from the GCP centroid. The correlation shows however, that the standard deviation decreases with an increase in range from the centroid. This may be a result of the GCP centroid being calculated as the centre of the polygon, formed by the fixed GCPs being in the middle of the scan scene. In Blenheim Quarry, GCPs may be nearly 100 m away from the centroid, however, the GCPs are not far from control. A more realistic result would be to evaluate scenarios A4 and A5 where CPs are used instead of evaluating the residuals of fixed GCPs.

Table 4.5. Underground coordinate residuals after the georeferencing LSE adjustment. Results are for the final A1 scenario. Values in m.

Station	rX	rY	rZ
W320	0.004	-0.002	-0.006
B102	-0.001	0.001	0.007
W319	0.003	0.008	-0.005
B101	-0.006	-0.009	0.008
N103	0.001	0.009	-0.016
W318	-0.008	-0.003	-0.007
W317	-0.001	0.001	0.008
W316	-0.005	-0.012	-0.005
N102	0.017	0.010	-0.011
W313	-0.008	-0.008	-0.002
N105	-0.006	0.000	0.008
N109	-0.009	-0.003	0.028
N107	-0.008	0.000	0.003
W309	-0.004	0.003	-0.007
W308	0.013	0.003	0.000
W306	0.023	0.012	0.006
W305	-0.010	-0.002	-0.007
W302	-0.024	0.009	0.001
W102	-0.003	0.005	-0.001
W106	-0.002	-0.004	-0.003
W110	-0.004	-0.005	0.003
W113	0.003	-0.015	-0.006
RMSE	0.010	0.007	0.009

Figure 4.8. Scenario A1. Horizontal and vertical residuals between the total station and the TLS coordinates. The total station coordinates have been used as the known coordinates.

In Scenario A2, Blenheim, Nelson, and Wellington Quarries were georeferenced individually to assess whether additional scans propagated error into the final A1 deliverable point cloud. The results for A2 are shown in Table 4.6. The RMSE and horizontal residuals for each of the

A2 scenarios show comparable results to that of A1. Blenheim Quarry has slightly smaller residuals than the other quarries, and this may be due to the scan extent being smaller and the range from the GCP centroid is slightly shorter than the other quarries (Figure 4.13). Figure 4.9 shows the horizontal residuals comparison of scenario A1 and A2, where there are minor deviations between the two. The result of georeferencing 200 scans or 800 scans is minor, where the residuals and RMSE appears to stay the same (Table 4.5 and Table 4.6). A benefit of reducing the scans could be to reduce time spent processing, where smaller datasets are more manageable. As with scenario A1, A2 is also able to mitigate the range dependent errors; an expected result given the previous tests and the placement of GCPs.

Table 4.6. Underground coordinate residuals after the georeferencing LSE adjustment. Results shown are for the A2 scenario. Values in m.

Quarry	Station	rX	rY	rZ
Blenheim	**W320**	0.005	-0.002	-0.008
	B102	-0.001	0.001	0.005
	W319	0.004	0.008	-0.007
	B101	-0.005	-0.008	0.007
	N103	0.002	0.007	-0.012
	W318	-0.007	-0.003	-0.009
	W317	0.000	0.000	0.007
	W316	-0.004	-0.013	-0.006
	N102	0.011	0.002	0.000
	RMSE	0.005	0.006	0.007
Nelson	**W316**	-0.004	-0.013	-0.006
	N102	0.018	0.010	-0.012
	W313	-0.006	-0.008	-0.003
	N105	-0.004	0.001	0.001
	N109	-0.007	-0.003	0.027
	N107	-0.006	0.000	0.003
	W309	-0.004	0.004	-0.008
	W308	0.004	0.008	-0.008
	W306	0.017	0.016	-0.001
	W305	-0.014	0.002	-0.013
	RMSE	0.010	0.008	0.011
Wellington	**W309**	-0.002	0.003	-0.006
	W308	0.016	0.003	0.001
	W306	0.026	0.012	0.007
	W305	-0.007	-0.002	-0.006
	W302	-0.021	0.008	0.001
	W102	0.003	0.004	-0.001
	W106	0.002	-0.005	-0.001
	W110	0.001	-0.005	0.005
	W113	0.008	-0.015	-0.002
	RMSE	0.009	0.006	0.003

Figure 4.9. Scenario A2. A horizontal comparison between completing the georeferencing for the entire project point cloud against georeferencing each quarry individually.

The purpose of not fixing control in Wellington Quarry was to try and assess what may happen to the accuracies in areas where no control was established, i.e. Auckland Quarry (See Figure 4.10). The results in Table 4.7 show an increase in overall RMSE compared to A1 and A2,

which is not unexpected given that the RMSEs are with respect to CPs and not fixed GCPs. Figure 4.13 again shows that RMSE is decreasing with an increase in range from the GCP centroid. This could be due to most of the fixed control being in Nelson and Blenheim, meaning the GCP centroid would be between Nelson and Blenheim. If the test evaluated CPs from GCPs, the result could be explained as the fixed GCP to the north of Wellington Quarry mitigating the distance dependent error of the closest CPs.

Table 4.7. Underground coordinate residuals after the georeferencing LSE adjustment. Results shown are for the A3 scenario. Values in m.

Quarry	Station	rX	rY	rZ
Wellington CPs	**W308**	0.025	0.004	0.008
	W306	0.036	0.012	0.015
	W302	-0.009	0.006	0.010
	W102	0.015	0.002	0.009
	W106	0.016	-0.007	0.008
	W110	0.016	-0.005	0.015
	W305	0.004	-0.001	0.002
	RMSE	0.020	0.006	0.010

Scenario A4 removed a substantial amount of fixed GCPs, with the fixed control being in an unfavourable position (Figure 4.11). The results reflect the poor placement of GCPs where the overall RMSE of the adjustment being 0.095 m. This is considerably larger than previous scenarios, with the RMSE and standard deviation showing significant correlation to range from the GCP centroid (Figure 4.13 and Figure 4.14). The results support the tests at the SoS prior to the fieldwork in France.

Figure 4.10. Scenario A3. Where no control was fixed in Wellington to replicate no control in the Auckland Quarry and areas outside the extents of the GCP control network.

Table 4.8. Underground coordinate positional differences after the georeferencing LSE adjustment. Results shown are for the A4 scenario. Values in m.

Station	rX	rY	rZ
B102	-0.003	-0.002	0.001
W319	0.005	0.009	0.004
B101	-0.010	-0.012	0.006
W318	-0.007	-0.001	0.000
W316	-0.003	-0.011	0.006
N102	0.011	0.009	-0.005
W313	0.003	-0.086	-0.003
N105	0.011	0.052	0.012
N109	0.018	-0.054	0.005
N107	0.037	-0.014	0.000
W309	0.133	-0.025	0.001
W308	0.154	-0.026	0.000
W306	0.203	-0.021	0.006
W305	0.190	-0.016	0.000
W302	0.100	0.191	0.021
W102	-0.048	0.231	0.026
W106	-0.088	0.183	0.024
W110	-0.141	0.016	0.018
W113	-0.431	-0.150	0.016
RMSE	0.135	0.092	0.012

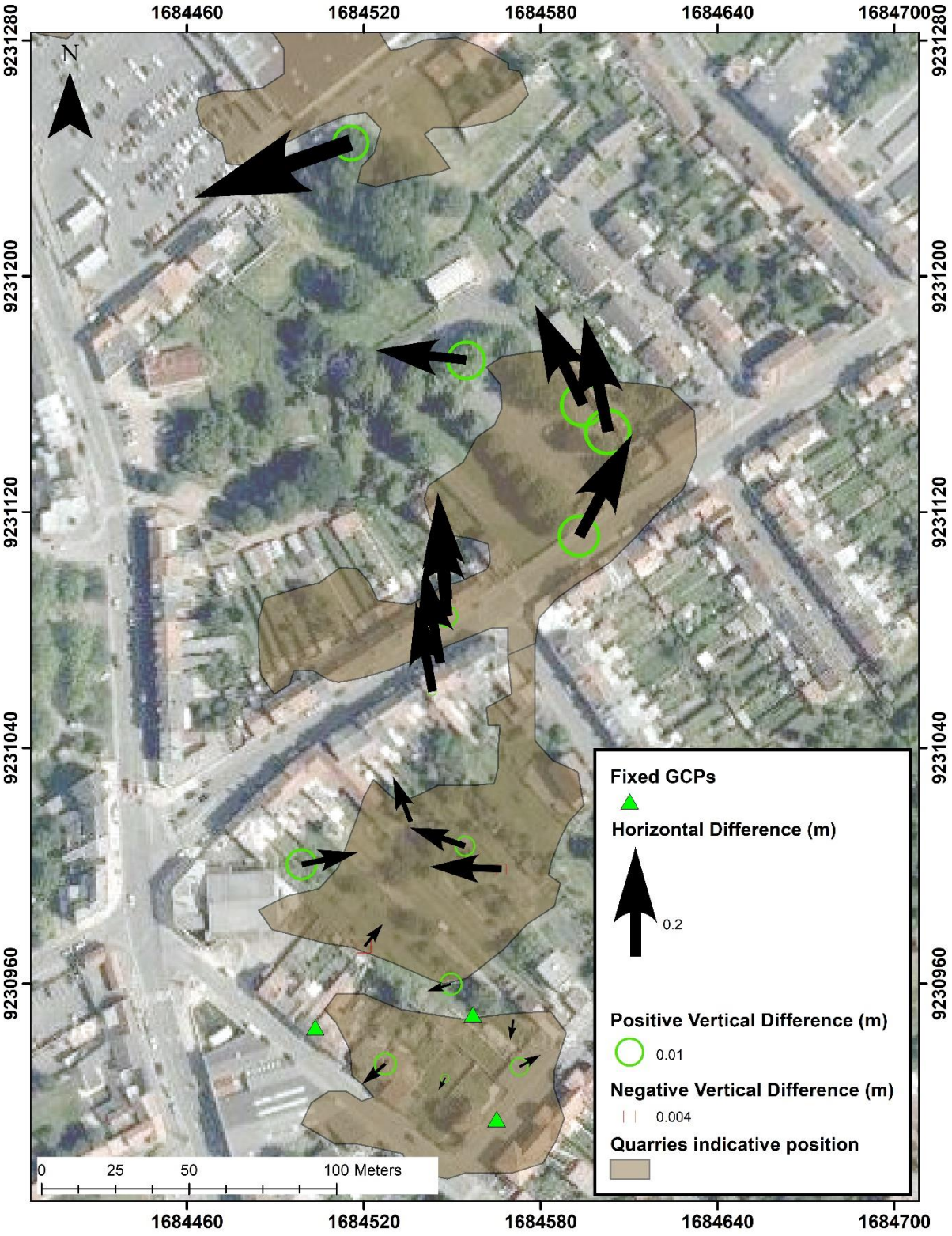

Figure 4.11. Scenario A4. Horizontal and vertical residuals when only three GCPs are held fixed, showing significant horizontal error with an increase in range from the fixed GCPs.

To determine whether an additional GCP on the other side of the scan scene could reduce the RMSE and CP residuals, scenario A5 was performed. A5 held the same three GCPs fixed as A4, however, it introduced an additional GCP (Figure 4.12). Interestingly the RMSE appears to increase with the additional GCP (Table 4.9), which is surprising, given the results from the tests at the SoS. The tests at the School suggested that the placement of control around a scan scene showed similar results to scenarios of increased control. What the tests did not show however, was a scenario where hundreds of scans were registered and georeferenced over large extents. Figure 4.13 (A5) shows the RMSE decrease at a range of 150-180 m from the GCP centroid. This is based on the additional fixed GCP. The GCP centroid for A5 is in the Nelson Quarry and therefore it is difficult to assess the RMSE as a function of range based on the GCP centroid. Alternatively, the CPs could be assessed on the range from a GCP, which represents the decline in RMSE at the range of 150-180 m. What this is also suggests is that over large extents, it is necessary to include more control, like A3, to mitigate the range dependent errors. The additional GCP did reduce the residuals for the CP that it was closest to, however, without accounting for a scale factor and the range to the other fixed GCPs, it appears to have rendered the network of A5 flexible and incompressible. This may explain the eastward bulge seen in Figure 4.12.

Table 4.9. Underground coordinate residuals after the georeferencing LSE adjustment. Results shown are for the A5 scenario. Values in m.

Station	rX	rY	rZ
B102	-0.007	0.024	-0.001
W319	0.000	0.020	0.004
B101	-0.013	0.026	0.006
W318	0.000	0.012	0.003
W316	0.005	0.019	0.008
N102	0.000	0.055	-0.007
W313	0.031	-0.067	-0.008
N105	0.040	0.106	0.010
N109	0.025	-0.016	0.001
N107	0.075	0.024	-0.007
W309	0.192	0.006	-0.006
W308	0.321	-0.013	-0.008
W306	0.420	-0.017	0.002
W305	0.416	-0.004	-0.008
W302	0.350	0.140	0.008
W102	0.251	0.167	0.015
W106	0.225	0.134	0.021
W110	0.099	0.006	0.004
RMSE	0.203	0.070	0.007

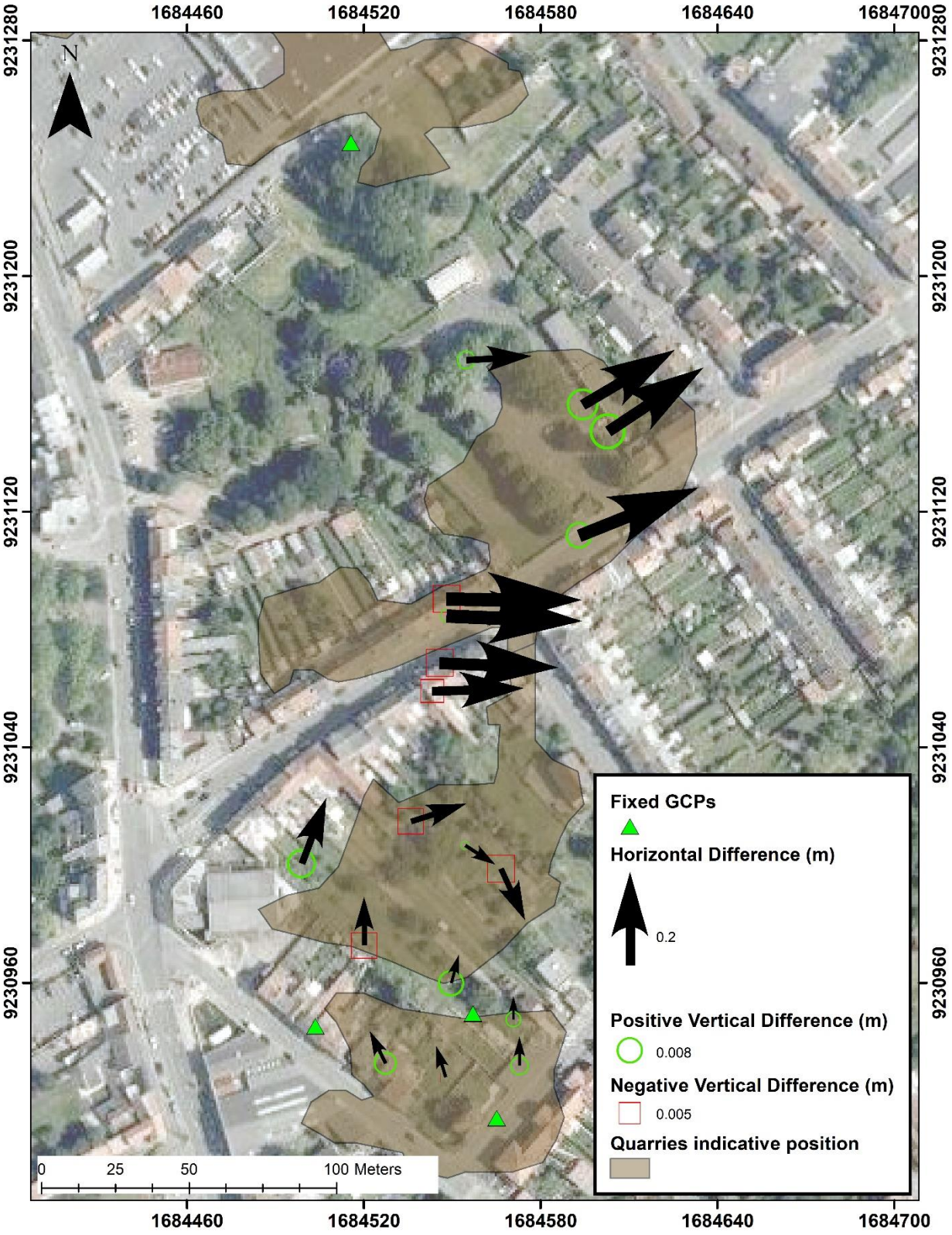

Figure 4.12. Scenario A5. Horizontal residuals when three GCPs are held fixed, showing significant horizontal error with an increase in range from the fixed GCPs. The additional GCP used has not reduced the RMSE seen in scenario A4.

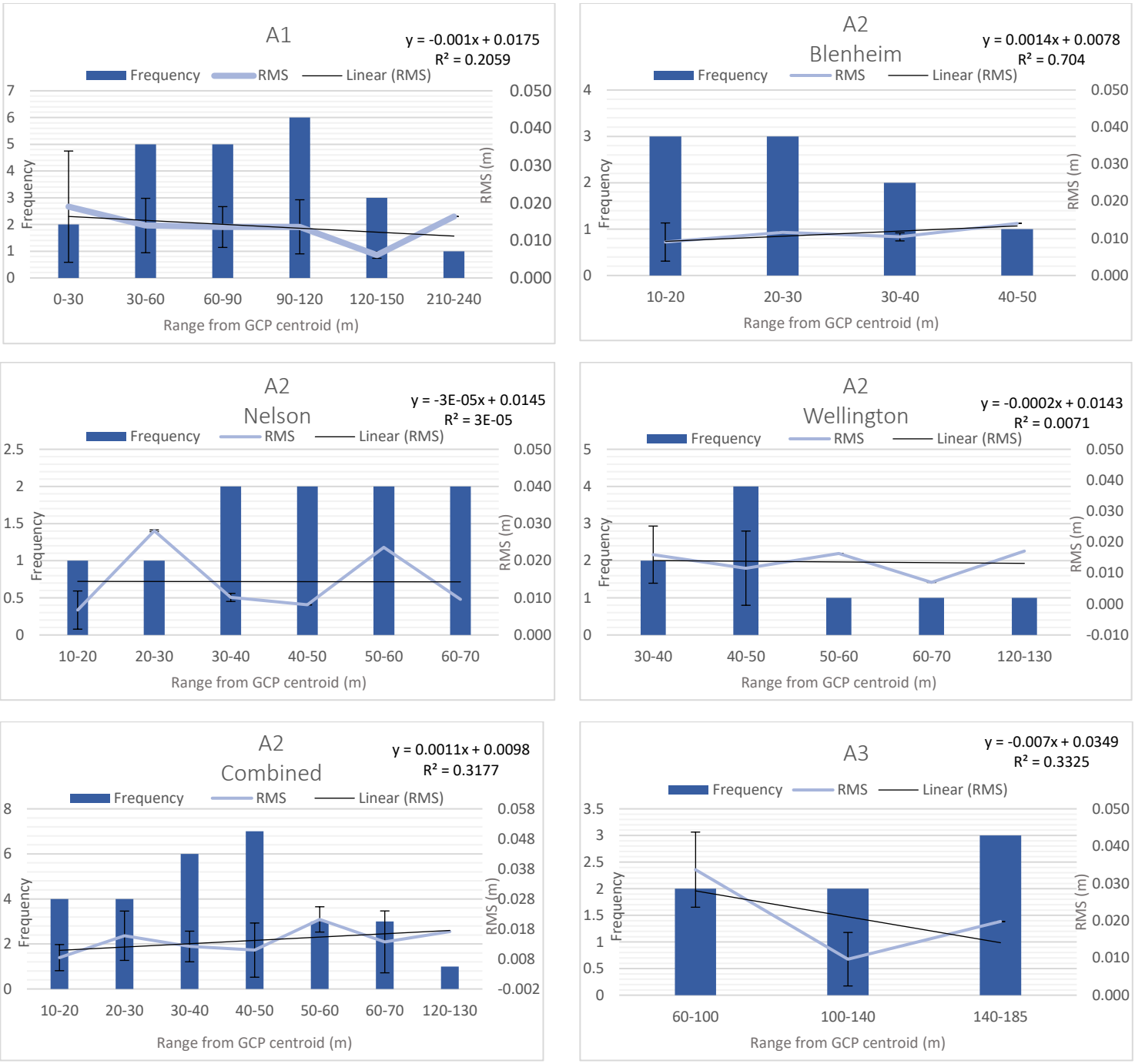

Figure 4.13. 3D RMS error as a function of range from GCP centroid for each scenario. Scenarios A1-A3 showing less correlation between range and RMSE compared to scenario A4, which held three GCPs fixed in the Blenheim quarry.

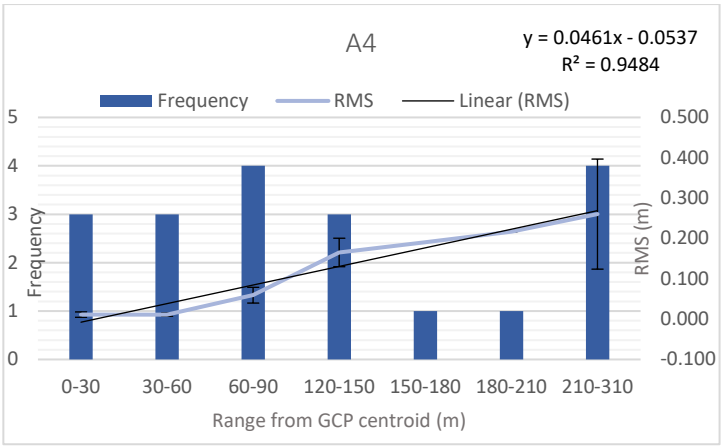

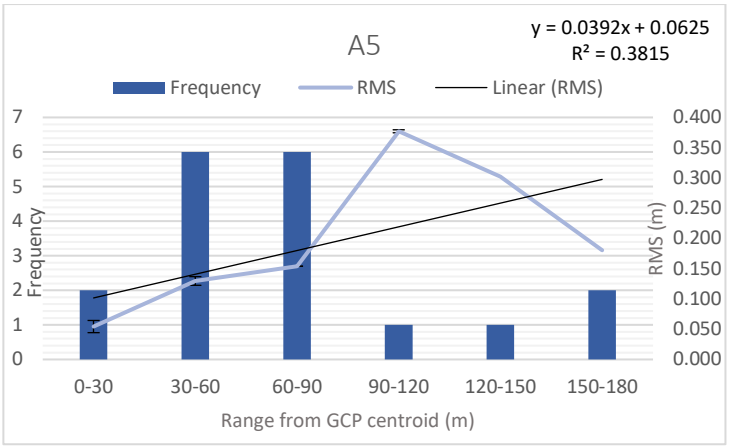

Figure 4.13 (Cont.). 3D RMS error as a function of range from GCP centroid for each scenario. Scenario A5 showing less of a correlation to RMSE and range from the GCP centroid compared to scenario A4 above. A2 Combined is a combination of the above A2 scenarios.

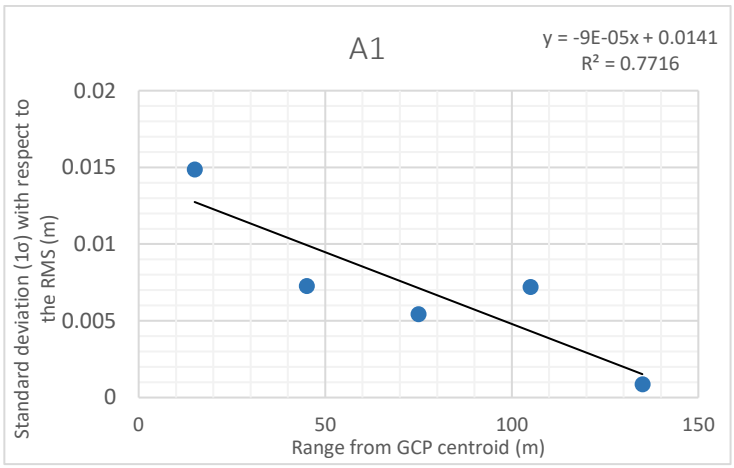

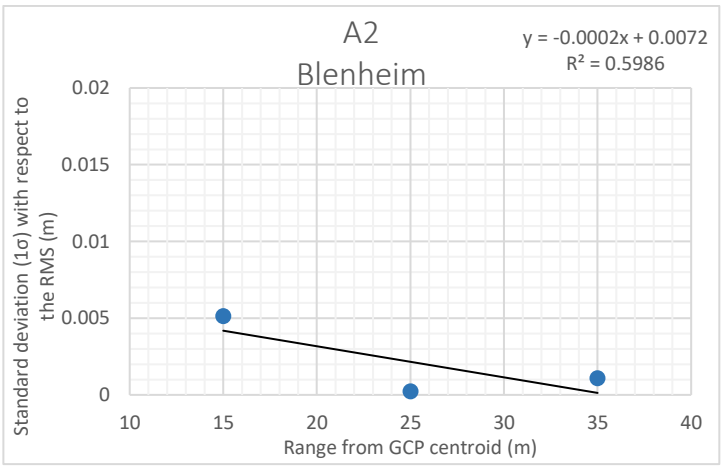

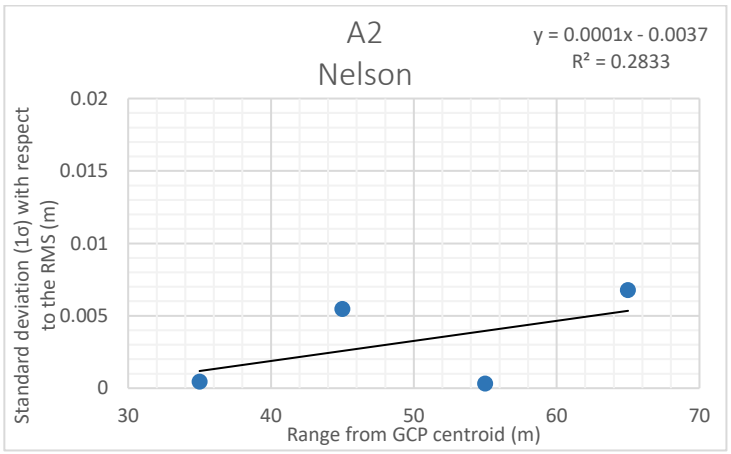

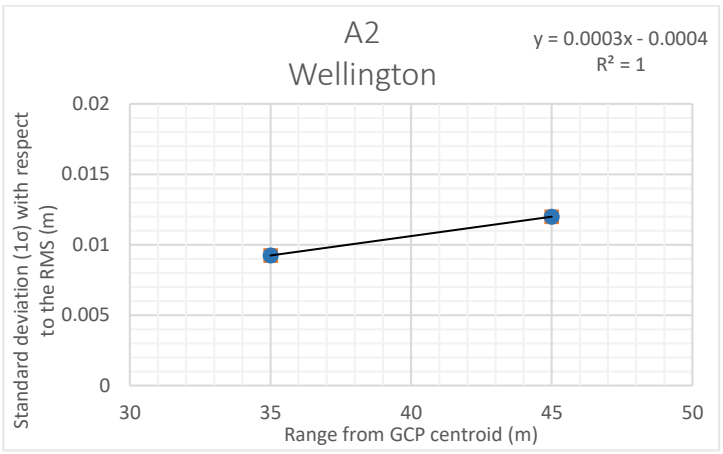

Figure 4.14. Standard deviation as a function of range from the GCP centroid.

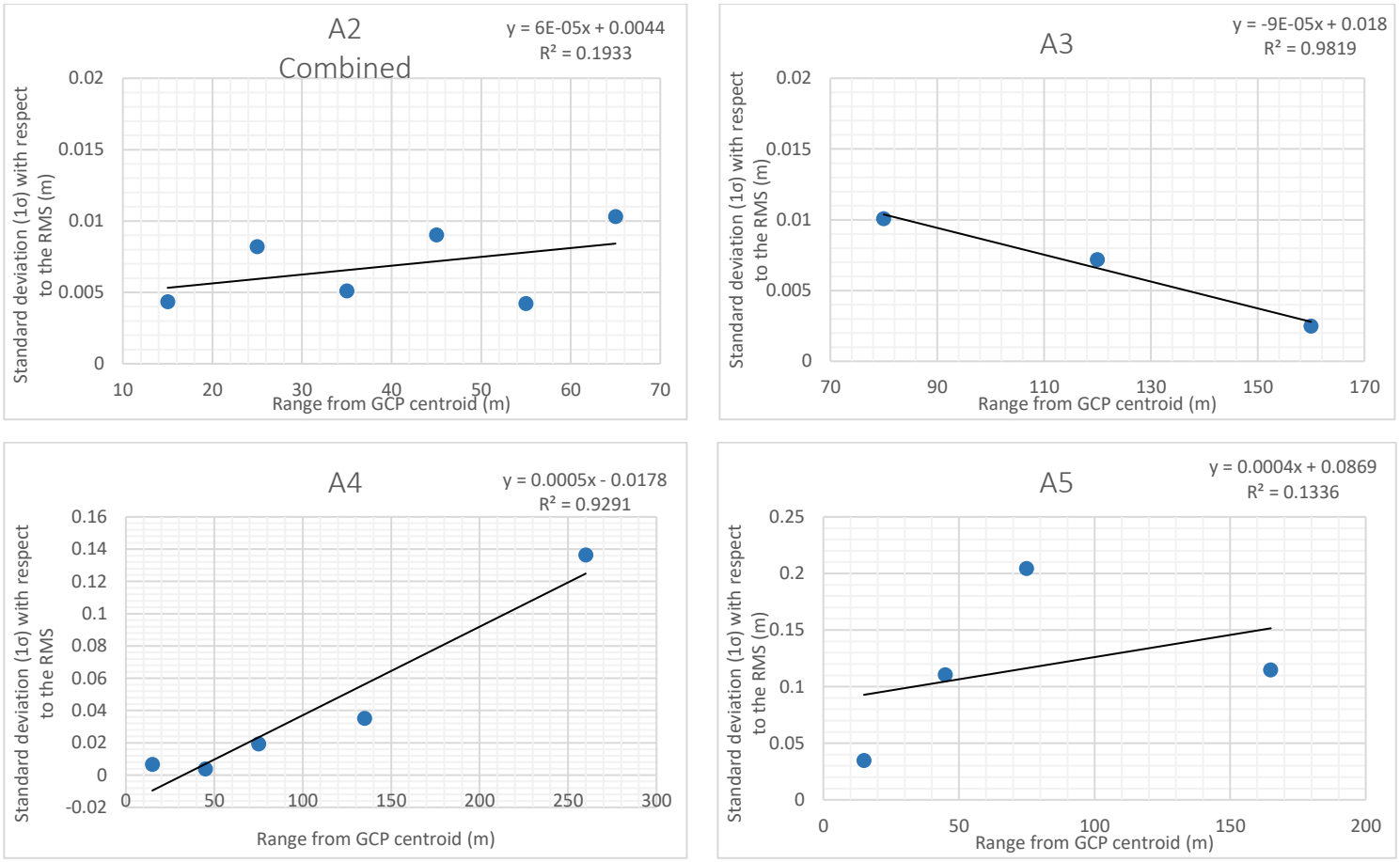

Figure 4.14 (Cont.). Standard deviation as a function of range from the GCP centroid.

The RMSE results for each scenario are shown in Table 4.10. There are no noticeable differences between the RMSE values for A1, A2, and A3. The horizontal positional differences for A1 and A2 are plotted and shown in Figure 4.9. Each scenario showed a similar magnitude and direction. Thus, georeferencing each quarry individually shows no immediate benefit although Blenheim Quarry did render slightly better in the horizontal component (Figure 4.9). As mentioned previously, Wellington Quarry lacks spatial coverage of GCPs, therefore to quantify the expected accuracy for this particular area of the underground network, a mock scenario was tested using Blenheim, Nelson, and a tunnel between Auckland and Wellington Quarries. The results show that A3 deteriorates slightly in the horizontal component, with the vertical component showing comparable results to A1 and A2. Mentioned previously was that A1 and A2 analysed the RMSE and residuals for the fixed GCPs, which is not the case for scenario A3, which analysed the RMSE and residuals for CPs. It is expected that a fixed point would yield more accurate results, thus the result for A3 is not surprising. What is noticeable is the substantial increase in RMSE for scenarios A4 and A5. Based on the tests at the SoS, these results were expected, given the significant increase in range from the GCP centroid. The propagation of error, without the necessary constraints of fixing control,

results in large deviations from the *known* coordinates. The additional GCP in A5 did not appear to reduce the RMSE even though the initial tests suggested that GCPs placed around the extents of the scan scene should mitigate the range dependent errors. What was noticeable was the CP closest to the additional GCP in A5 did reduce in magnitude. It can be concluded that the range and lack of estimated scale parameter was too substantial for the additional GCP to mitigate these errors, with additional GCPs being required over large extents (Scenario A3). The areas in Auckland Quarry without control should expect errors to increase with an increase in range from the fixed point W113 (Figure 4.4). Scenario A4 shows a significant correlation between the RMSE and range (Figure 4.13) where at 250 m CP residual of 260 mm occurs. Therefore, it is expected, errors of up to 100 mm per 100 m be expected for areas of Auckland Quarry in the horizontal component, while the overall vertical errors for scenario A4 and A5 were 12 mm and 7 mm respectively. The dual axis compensator accounts for any deviations of the vertical and levels the instrument with slight imbalances in instrument plumbing.

Table 4.10. Root mean square errors for the various georeferencing scenarios. Where A1 and A2 are the RMSE on the GCPs and A3, A4, and A5 are the RMSE for stations that were not fixed for the georeferencing. Values in mm.

Scenario	A1	Blenheim (A2)	Nelson (A2)	Wellington (A2)	A3	A4	A5
rX	10	5	10	13	20	135	203
rY	7	6	8	8	6	92	70
rZ	9	7	11	4	10	12	7
rXYZ	9	6	10	9	13	95	124

4.3.3 Sampling, segmentation, and exporting

The registration parameters from scenario A1 (i.e. using all points seen in Figure 4.4 as control) were exported to the tzf files once the final point cloud was georeferenced. By doing this, the files can be reimported to RealWorks and registration is no longer required. The user can define a sample resolution and the same registration and georeferenced parameters as computed and defined previously will remain. A 2 mm sample resolution was chosen, rendering a point cloud of 24 billion points. It was decided, given the size of the dataset, that each quarry would be sampled as an individual project. Having exported the registration parameters to each tzf file, registration was not required and theoretically all points align when exported to third party software. Each quarry's point cloud size was ~7 billion points and therefore they were segmented further. This option was chosen as a test done with the entire Nelson Quarry point cloud, exported at 2mm, rendered a 278 GB .pts file. The size of the individual files creates issues when importing to third party software. It was found to be more manageable with each

quarry segmented into smaller point clouds. Each quarry was “cleaned” for point artefacts. The removal of these artefacts is done manually and requires users to make subjective decisions. The cleaned individual point clouds have been exported in an open source compatible file format, las. Table 4.11 shows the how many point cloud segments there are for each quarry, the file size and respective points in each quarry point cloud.

Table 4.11. Point segments and las file size per quarry and point cloud size.

Quarry	Point Cloud Segments	File Space (las format in GB)	Points in Point Cloud (billion pts)
Wellington	7	165	7.1
Nelson	4	130	5.4
Blenheim	6	175	7.3
Auckland	1	35	1.3
Streetscape	3	70	3.1

4.3.4 Deliverables

Fieldwork 1 and fieldwork 2 data were separated into individual folders. The TX8 scan data was catalogued into folders by day, including the raw tzf file, every individual photo captured, and the rendered panorama. The TX5 data was catalogued similarly, however in the fls file format. The raw data is considered to be the level 0 data, for which the file size amounted to 517 GB.

All registered, georeferenced, and colourised scans were catalogued separate from the level 0 data. This data is considered the level 1 data and only requires users to sample the data. When resampling, the software will extract every point from the tzf file, at the specified resolution, and therefore, no erroneous data points will have been removed. The combined file size for the level 2 data was 355 GB.

The level 2 data is the final cleaned, exported las point cloud files. As explained previously, due to file size, each quarry had several las files. The combined las files had a combined size of 570 GB. Table 4.12 is a summary of each of the data levels.

Table 4.12. Data level summary.

Data Level	Product	File count
Level 0	Raw scan files (tzf and fls), individual photos, and panoramas	814 tzf scan files and 153 fls scan files.
Level 1	All colourised, registered, and georeferenced point cloud data	967 tzf scans
Level 2	Cleaned las point cloud files	21 las files

The segmented las quarry shapes are shown in Figure C.1 - Figure C.13, in the Appendix C. The order of the figures shown start with the underground quarry network. Each quarry is highlighted from north to south, in the order of Auckland, Wellington, Nelson, and Blenheim. Each subsequent quarry segmented las files are shown and labelled accordingly. The streetscape is presented last.

4.4 Chapter summary

The objective for this project was to accurately document, in 3D, a section of the Ronville Tunnels in Arras, France. 967 scans were collected and then georeferenced using 22 GCPs in the underground quarries, bearing a final 3D RMSE of 9 mm. Several georeferencing scenarios were tested. They showed that georeferencing individual quarries made no improvement to the overall accuracy of the point cloud data, while fixing the three GCPs on a single side of the underground network resulted in significant error. The results were comparable to those in Chapter 3 where an increase in range from the GCP centroid had negative effects on the point cloud accuracies (Figure 4.13 and Figure 4.14). Including an additional GCP on the other side of the underground network (A5) did not reduce the overall RMSE. Based on the SoS results, it was expected that the inclusion of an additional GCP would have mitigated the range dependent errors. However, the long range, no estimable scale parameter, and propagation of error with the additional scans means that the inclusion of an extra GCP is not enough to mitigate these errors. This suggests that, where possible, it is best to keep the range short between GCPs throughout the scan scene. The outcome of this research is important for all TLS users, particularly for non-spatial measurement experts. This contribution provides a template for documenting and recording heritage sites in a universal coordinate system and the accuracies that can be anticipated. The evolution of spatial measurement technology and its ease of use now allows for data capture by inexperienced users, which can lead to unfavourable results, therefore highlighting the importance of the conducted research.

The final chapter, 5, will summarise the findings in this study and make recommendations on future research that may be valuable in this field. There are possibilities of creating animations, meshed models, and interactive online models made available to the public. The limiting factor remains the dataset size, given that previous literature has suggested hardware capabilities are currently restricting these possibilities.

Chapter 5 Conclusion, and future research

Terrestrial laser scanning has proven advantageous for the mapping and documentation of heritage sites. Fast acquisition of precise data recreates intricate details of unique surfaces. Often the acquired point cloud data is to be amalgamated with other data sources; photogrammetry or temporal TLS data. A way of combining these datasets is to assign real world coordinates to the point cloud data; a process known as georeferencing. The indirect georeferencing process was investigated in this thesis; specifically, the quantity of GCPs used and their relative position throughout a scan scene.

5.1 Conclusion

The research conducted at the SoS was an investigation into the quantity and spatial coverage of GCPs in a scan scene (Figure 3.4). It was undertaken as a preamble to the LiDARRAS heritage site project, where time was a limiting factor for the data capture. The tunnels, located below the town of Arras, were required to be captured accurately and in a time efficient manner. The results of the tests prior to the case study highlighted the importance of considering the placement of GCPs over the quantity used (Figure 3.8 - Figure 3.10, Table 3.4 and Table 3.6). "*What is the effect of the quantity and spatial variability of GCPs used on the accuracy of TLS surveys?*" The result of the research suggesting that an increase in point cloud error being highly correlated to an increase in range from the GCP centroid. The centroid is the average of the fixed GCPs. The extent of the heritage site is hundreds of metres long compared to the SoS, within which the scan scene extends several tens of metres. The results from the SoS suggested that holding control fixed around the extents of the scan scene is more important than the quantity held fixed. The heritage site however, proved that where there are many scans, additional control is required to mitigate the increase of error in the point cloud (Figure 4.8 - Figure 4.10). This is not an unexpected result when considering error propagation. When hundreds of scans are aligned to each other, every deviation from the "truth" will propagate uncertainty into the subsequent scans. As the range increases from fixed control, so does the uncertainty of the known position. The hypothesis of fixing more control is comparable to an LSE adjustment, proven to be more apparent in the case of the LiDARRAS investigations.

A framework for TLS heritage site documentation has been presented, with specific attention given to the indirect georeferencing technique. This method of georeferencing uses precoordinated positions. Artificial targets are then positioned over these marks, which are captured during the TLS survey. The heritage site case study provided various GCP scenarios

that may be used as a template for which others may choose to replicate. The scenarios were investigated to potentially provide insight into the accuracies that may be expected where control is limited with the unique nature of heritage sites. These accuracies are important to understand when combining TLS data with data obtained from other sources.

5.2 Future work

This research presented a framework for georeferencing TLS data and applied it to a heritage site case study. This is a beneficial contribution to the existing literature with respect to TLS practitioners; geospatial specialists and non-specialists alike. The thesis also presented the results of unfavourable spatial placement of GCPs, which may be common when undertaking a TLS survey of a heritage site. The following are areas that were not considered in this research and may be areas of interest for future research:

1. The research was primarily conducted using Trimble RealWorks software. The interface of the software does not allow for an in-depth analysis of the algorithms being applied to the registration and georeferencing processes. For testing different surface to surface registration matching algorithms, MATLAB could provide a more flexible platform. Alternately, the Leica software Cyclone may provide slightly different results based on the coded algorithms.
2. Heritage sites are unique, and provide individual challenges for data collection. What was not investigated in this research was the use of control in the vertical plane. The control was predominantly established considering only the horizontal placement of each GCP position. With heritage sites varying in spatial complexity, structures and monuments may appear to meet certain accuracies horizontally without fulfilling the same accuracies vertically. Increased range and incident angle reduces the accuracy of the final point cloud data, which may occur with steadily inclined measurements. An investigation into the vertical accuracies of GCPs may therefore be worthwhile.
3. Reshetyuk (2010) has previously combined TLS instruments with GNSS receivers to directly georeference point cloud data. Schumacher and Böhm (2005) presented their findings whereby a low-cost GPS receiver was mounted above a TLS instrument to directly georeference the point cloud data. The result was accuracies of 4.7m using low-cost GPS and tie points. Currently, research is presenting the feasibility of low-cost GNSS receivers to provide survey grade (centimetre-level) accuracies, with high success rates (Odolinski and Teunissen, 2016; Odolinski and Teunissen, 2017). The advancement of low-cost receivers mean that they now track multi-constellation

satellites allowing increased redundancy in determining positions, with improved accuracies. An investigation into the amalgamation of the improved low-cost GNSS technology and TLS may be worthwhile. With improved accuracies, it may allow for a reduction in fieldwork by mitigating the need to establish a control network prior to undertaking a TLS.

4. The SoS tests suggested that additional GCPs around the extent of a scan scene may reduce the magnitude of expected check point residuals, however, scenarios A4 and A5 contradict this finding (Table 4.10). It can be hypothesised that the lack of an estimated scale parameter has rendered the network very flexible but incompressible for scenario A5. The additional fixed GCP in A5 may be a result of a southward compression being applied to the network, causing a large transverse distortion. Hence, the eastward bulge apparent in scenario A5 (Figure 4.12) may be relieved with an appropriately estimated scale factor. Such research may be beneficial where long linear networks (such as tunnel surveys) are controlled for georeferencing at its terminals.

5.3 Closing remarks

TLS, as a technique for the documentation of heritage sites, has proven popular over the last decade, with its fast and precise acquisition of data. This thesis has provided an analysis of the indirect georeferencing accuracies under various GCP scenarios. To the best of our knowledge previous literature had not quantified this issue, which may save time when undertaking a TLS survey. TLS operators should consider, where possible, the placement of GCPs, and reduce the range between GCPs in scan scenes with large extents. In the case of the SoS research, a reduced number (three) of evenly distributed GCPs showed similar results to a reference scenario where more GCPs were fixed (Table 3.4 and Table 3.6). The LiDARRAS case study achieved a final overall RMSE of 17mm when 22 GCPs were distributed evenly around the underground network of tunnels. Noted differences between the test area at the SoS and the LiDARRAS project are the size of the scan scenes and the number of scans collected. Therefore, these differences should be considered by TLS operators when undertaking TLS surveys to meet required accuracies.

References

Alba, M., and Scaioni, M. (2007). Comparison of techniques for terrestrial laser scanning data georeferencing applied to 3-D modelling of cultural heritage. *The International Archives of the Photogrammetry, Remote Sensing and Spatial Information Sciences*, 36(5/W47): 8.

Argüelles-Fraga, R., Ordóñez, C., García-Cortés, S., and Roca-Pardiñas, J. (2013). Measurement planning for circular cross-section tunnels using terrestrial laser scanning. *Automation in Construction*, 31: 1-9.

Bae, K, H., and Lichti, D, D. (2008). A method for automated registration of unorganised point clouds. *ISPRS Journal of Photogrammetry and Remote Sensing* 63(1): 36-54.

Barsanti, S.G., Remondino, F., and Visintini, D. (2012). Photogrammetry and Laser Scanning for Archaeological Site 3D Modeling—Some Critical Issues. *In Proceedings of the 2nd Workshop on the New Technologies for Aquileia*, Italy 2012; pp. B1–B10.

Becerik-Gerber, B., Jazizadeh, F., Kavulya, G., and Calis, G. (2011). Assessment of target types and layouts in 3D laser scanning for registration accuracy. *Automation in Construction* 20(5): 649-65

Besl, P. J., and McKay, N. D. (1992). A method for registration of 3-D shapes. *IEEE Transactions on Pattern Analysis and Machine Intelligence* 14(2): 239-256.

Blais, F., Beraldin, J. A., and El-Hakim, S. F. (2000). Range error analysis of an integrated time of flight, triangulation, and photogrammetric 3D laser scanning system. *Proceedings of the SPIE: AeroSense*, Kamerman, G. W., Singh, U. N., Werner, C., and Molebny, V. V. Vol 4035, Orlando, Florida. April 2000, pp 236-247.

Boehler, W., and Marbs, A. (2002). 3D scanning instruments. *Proceedings of the CIPA WG* 6: 9-18.

Boehler, W., Bordas, V, M., and Andreas, M. (2003). Investigating laser scanner accuracy. *The International Archives of Photogrammetry, Remote Sensing and Spatial Information Sciences*, 34(5): 696-701.

Bornaz, L., Lingua, A., and Rinaudo, F. (2003). Multiple scanner registration in LIDAR close-range applications. *International Archives of Photogrammetry, Remote Sensing and Spatial Information Sciences* 34(5/W12): 72-77.

Chen, Y., and Medioni, G. (1992). Object modelling by registration of multiple range images. *Image and vision computing* 10(3): 145-155.

Delaloye, D., Hutchinson, J., and Diederichs, M. (2011). Accuracy issues associated with Lidar scanning for tunnel deformation monitoring. *Paper presented at the Proceedings of the 2011 Pan-AM CGS Geotechnical Conference.*

Dos Santos, D. R., Dal Poz, A. P., Khoshelham, K. (2013). Indirect Georeferencing of Terrestrial Laser Scanning Data using Control Lines. *The Photogrammetric Record* 28(143): 276-292.

El-Hakim, S. F., Beraldin, J.-A., Picard, A., and Vettore, A. (2003). Effective 3D modeling of heritage sites. *Fourth International Conference on 3-D Digital Imaging and Modeling, 2003 (3DIM03)*. Proceedings.

El-Hakim, S.F., Fryer, J.G., and Picard, M. (2004). Modelling and visualization of aboriginal rock art in the Baiame cave. *International Archives of Photogrammetry and Remote Sensing.* 35, 5, 990-995.

Fan, L., Smethurst, J, A., Atkinson, P, M., and Powrie, W. (2015). Error in target-based georeferencing and registration in terrestrial laser scanning. *Computers & Geosciences.* 83: 54-64.

Fekete, S., and Diederichs. M., (2013). Integration of three-dimensional laser scanning with discontinuum modelling for stability analysis of tunnels in blocky rockmasses. *International Journal of Rock Mechanics and Mining Sciences*. 57: 11-23.

Ferré, G. (2016). Projet LiDARRAS: Réseau de points géoréférencés. *Unpublished report.*

Ge, X., and Wunderlich, T., (2015). Target identification in terrestrial laser scanning. *Survey Review* 47(341): 129-140.

Geymen, A., (2009). Development of an information and management system for recording, analysis, protection and revitalization of cultural heritage application case study of Istanbul. *Lasers in Engineering,* 19(1): 93.

Ghilani, C, D. (2010). Constraint equations In *Adjustment Computations Spatial Data Analysis, Fifth Edition* (pp. 416-434). John Wiley & Sons, Inc., Hoboken, NJ, USA.

Gordon, S. J., Lichti, D. D., Stewart. M. P., and Tsakiri. M. (2001). Metric performance of a high-resolution laser scanner. *Videometrics and Optical Methods for 3D Shape Measurement,* 22-23 January 2001, 49-56.

Growcott, A., Sirguey, P., and Dawson, S. M. (2012). Development and assessment of a digital stereo photogrammetric system to measure cetaceans at sea. *Photogrammetric Engineering & Remote Sensing,* 78(3), 237-246.

Gruen, A., and Akca, D. (2005). Least squares 3D surface and curve matching. *ISPRS Journal of Photogrammetry and Remote Sensing* 59(3): 151-174.

Grussenmeyer, P., Landes, T., Voegtle, T., and Ringle, K. (2008). Comparison methods of terrestrial laser scanning, photogrammetry and tacheometry data for recording of cultural heritage buildings. *International Archives of Photogrammetry, Remote Sensing and Spatial Information Sciences* 37(B5): 213-218.

Grussenmeyer, P., Alby, E., Landes, T., Koehl, M., Guillemin, S., Hullo, J. F., Assali, P., and Smigiel, E. (2012) Recording approach of heritage sites based on merging point clouds from high resolution photogrammetry and terrestrial laser scanning. *International Archives of Photogrammetry, Remote Sensing, and Spatial Information Sciences. XXXIX-B5,* 553-558, doi:10.5194/isprsarchives-XXXIX-B5-553-2012.

Guidi, G., Tucci, G., Beraldin, J.-A., Ciofi, S., Ostuni, D., Costantini, F., and El-Hakim, S. (2002). Multiscale archaeological survey based on the integration of 3D scanning and photogrammetry. *Proceedings: International Workshop on Scanning for Cultural Heritage Recording, Corfu, Greece*. Sept 2002. pp. 58-64.

Jafaar, H. A., Meng, X., and Sowter, A. (2017). Terrestrial laser scanner error quantification for the purpose of monitoring. *Survey Review* 1-17.

Kersten, T. P., Sternberg, H., and Mechelke, K. (2005). Investigations into the accuracy behaviour of the terrestrial laser scanning system Mensi GS100. *Proceedings of 7th Conference in Optical 3D Measurement Techniques.* Vienna 2005.

Laefer, D.F., Fitzgerald, M., Maloney, E. M., Coyne, D., Lennon, D., and Morrish, S. (2009). Lateral image degradation in terrestrial laser scanning. *Structural engineering international, 19, 184–189.*

Lai, L., and Sordini, M. (2013). 3D documentation of a megalithic building in Sardinia. *Proceedings of the 18th International Conference on Cultural Heritage and New Technologies.* CHNT 2013.

Lai, L., Sordini, M., Campana, S., Usai, L., and Condò, F. (2015). 4D recording and analysis: The case study of Nuraghe Oes (Giave, Sardina). *Digital Applications in Archaeology and Cultural Heritage*. 2(4): 233-239.

Lambers, K., Eisenbeiss, H., Sauerbier, M., Kupferschmidt, D., Gaisecker, T., Sotoodeh, S., and Hanusch T. (2007). Combining photogrammetry and laser scanning for the recording and modelling of the Late Intermediate Period site of Pinchango Alto, Palpa, Peru. *Journal of Archaeological Science* 34(10): 1702-1712.

Lemmens, M. (2011). Terrestrial Laser Scanning. *Geo-information: Technologies, Applications and the Environment*. Dordrecht, Springer Netherlands**:** 101-121.

Lichti, D. D., and Harvey, B. R. (2002a). The Effects of Reflecting Surface Material Properties on Time of flight Laser Scanner Measurements. *Symposium on Geospatial Theory, Processing and Application.* Ottawa 2002.

Lichti, D. D., and Harvey, B. R. (2002b). An investigation into the effects of reflecting surface material properties on terrestrial laser scanner measurements. *Geomatics Research Australia.* 76: 1-22.

Lichti, D., and Gordon, S. (2004). Error Propagation in Directly Georeferenced Terrestrial Laser Scanner Point Clouds for Cultural Heritage Recording. *Proceedings of the FIG Working Week, Athens, Greece.* pp 1-16.

Lichti, D. D., Gordon, S., and Tipdecho, T. (2005). Error Models and Propagation in Directly Georeferenced Terrestrial Laser Scanner Networks. *Journal of Surveying Engineering* 131(4): 135-142.

Lichti, D. D., and Jamtsho, S. (2006). Angular resolution of terrestrial laser scanners. *The Photogrammetric Record* 21(114): 141-160.

Lichti, D. D., and Skaloud, J. (2010). Registration and Calibration. In *Airborne and Terrestrial Laser Scanning*, G. Vosselman and H.-G. Maas (Eds.). Whittles Publishing: Caithness, UK, 83-133.

Masuda, T., and Yokoya, N. (1995). A Robust Method for Registration and Segmentation of Multiple Range Images. *Computer Vision and Image Understanding* 61(3): 295-307.

Nettley, A., Anderson, K., DeSilvey, C., and Caseldine, C. (2011). "Using Terrestrial Laser Scanning and LiDAR Data for Photo-realistic Visualization of Climate Impacts at Heritage Sites." *International Archives of Photogrammetry, Remote Sensing and Spatial Information Sciences* 38: 5.

O'Grady, K. F., and Antonyshyn, M. (1999). Facial asymmetry: three-dimensional analysis using laser surface scanning. *Plastic and reconstructive surgery*, 104(4): 928-937.

Odolinski, R., and Teunissen, P, J, B. (2016). Single-frequency, dual-GNSS versus dual-frequency, single-GNSS: a low-cost and high-grade receivers GPS-BDS RTK analysis. *Journal of Geodesy* 90(11): 1255-1278.

Odolinski, R., and Teunissen, P, J, B. (2017). Low-cost, high-precision, single-frequency GPS–BDS RTK positioning. *GPS Solutions*. 1-16.

Paffenholz, J. A., Alkhatib, H., and Kutterer, H. (2010). Direct geo-referencing of a static terrestrial laser scanner. *Journal of Applied Geodesy*, 4(3): 115-126.

Pejić, M. (2013). Design and optimisation of laser scanning for tunnels geometry inspection. *Tunnelling and Underground Space Technology*, 37: 199-206.

Pfeifer, N., and Briese, C. (2007a). Geometrical aspects of airborne laser scanning and terrestrial laser scanning. *International Archives of Photogrammetry, Remote Sensing and Spatial Information Sciences*, 36(3/W52), 311-319.

Pfeifer, N., and Briese, C. (2007b). Laser scanning — principles and applications. *3rd International Exhibition & Scientific Congress on Geodesy, Mapping, Geology, Geophysics, and Cadastre* GEO-SIBERIA 2007, Novosibirsk, Russia.

Rees, W. G., (2013). *Physical principles of remote sensing*: Cambridge University Press.

Remondino, F. (2011). Heritage recording and 3D Modelling with Photogrammetry and 3D Scanning. *Remote Sensing* 3(6): 1104-1138.

Reshetyuk, Y. (2009). Self-calibration and direct georeferencing in terrestrial laser scanning. Doctoral Thesis, KTH.

Reshetyuk, Y. (2010). Direct georeferencing with GPS in terrestrial laser scanning. *Z f V-Zeitschrift für Geodäsie, Geoinformation und Landmanagement* 135(3): 151-159.

Rodríguez-Gonzálvez, P., Nocerino, E., Menna, F., Minto, S., and Remondinob, F. (2015). 3D Surveying & Modelling of Underground Passages in WWI Fortifications. *ISPRS-International Archives of the Photogrammetry, Remote Sensing and Spatial Information Sciences* 1: 17-24.

Rüther, H., Held, C., Bhurtha, R., Schröder, R., and Wessels, S. (2011). Challenges in heritage documentation with terrestrial laser scanning. *Proceedings of the 1st AfricaGEO Conference*.

Scaioni, M. (2012). On the estimation of rigid-body transformation for TLS registration. *International Archives of Photogrammetry, Remote Sensing and Spatial Information Sciences,* XXXIX-B5: 601-606.

Schuhmacher, S., and Böhm, J. (2005). Georeferencing of terrestrial lasers canner data for applications in architectural modelling. *International Society for Photogrammetry and Remote Sensing Archives,* XXXVI-5/W17.

Schulz, T. (2007). Calibration of a Terrestrial Laser Scanner for Engineering Geodesy. Doctoral Thesis, ETH Zurich.

Shan, J. and Toth C. K. (2008). Topographic laser ranging and scanning: principles and processing, CRC press.

Sheng, Y. (2008). Quantifying the Size of a Lidar Footprint: A Set of Generalized Equations. *IEEE Geoscience and Remote Sensing Letters.* **5**(3): 419-422.

Soudarissanane, S., Lindenbergh, R., Menenti, M., and Teunissen, P. (2011). Scanning geometry: Influencing factor on the quality of terrestrial laser scanning points. *ISPRS Journal of Photogrammetry and Remote Sensing.* 66(4): 389-399.

Soudarissanane, S. (2016). The Geometry of Terrestrial Laser Scanning Identification of Errors, Modeling and Mitigation of Scanning Geometry. Doctoral Thesis, TU Delft. doi:10.4233/uuid:b7ae0bd3-23b8-4a8a-9b7d-5e494ebb54e5

Theiler, P. W., and Schindler, K. (2012). Automatic Registration of Terrestrial Laser Scanner Point Clouds Using Natural Planar Surfaces. *ISPRS Annals of the Photogrammetry, Remote Sensing and Spatial Information Sciences.* I-3: 173-178.

Theiler, P. W., Wegner, J., and Schindler, K. (2014). Fast registration of laser scans with 4-points congruent sets–what works and what doesn't. *ISPRS annals of the photogrammetry, remote sensing and spatial information sciences*, 2, 149–157.

Theiler, P. W. (2015). Automated Registration of Terrestrial Laser Scanner Point Clouds. ETH-Zürich 2015.http://dx.doi.org/10.3929/ethz-a-010540618

Van Genechten, B., Caner, H., Heine, E., Garcia, J. L. L., Poelman, R., Quintero, S. Q., *et al*. (2008). Theory and practice on terrestrial laser scanning: training material based on practical applications. Valencia, Spain: Universidad Politecnica de Valencia Editorial.

Voegtle, T., and Schwab, I. (2008). Influences of different materials on the measurements of a terrestrial laser scanner (TLS).

Vosselman, G., and Maas, H. G. (2010). Airborne and terrestrial laser scanning, Whittles Publishing.

Watt, P. J., and Donoghue, D. N. M. (2005). Measuring forest structure with terrestrial laser scanning. *International Journal of Remote Sensing*. 26(7): 1437-1446.

Zámečníková, M., Wieser, A., Woschitz, H., and Ressl, C. (2014). Influence of surface reflectivity on reflectorless electronic distance measurement and terrestrial laser scanning. *Journal of Applied Geodesy*. **8**(4): 311-326.

Appendix A

Registration Report (using TZF Scans)

User Name: Chris.Page
Date: Wed Jun 07 08:02:35 2017
Project Name: SS Registration
Length Measurement Units: Millimeters
Coordinate System: X, Y, Z

Overall Cloud-to-Cloud Error: 2.68 mm

Ss_test000 - 22 Station(s) with Points in Common -

Object Name	Cloud-to-Cloud Error	Coincident Points (%)	Confidence (%)
Ss_test001	1.45 mm	68%	100%
Ss_test002	1.41 mm	65%	100%
Ss_test003	1.63 mm	64%	100%
Ss_test004	1.48 mm	66%	100%
Ss_test005	2.25 mm	48%	100%
Ss_test006	2.86 mm	56%	100%
Ss_test007	2.64 mm	57%	100%
Ss_test008	3.48 mm	63%	100%
Ss_test009	4.41 mm	63%	100%
Ss_test010	4.72 mm	58%	100%
Ss_test011	4.87 mm	18%	100%
Ss_test012	5.72 mm	5%	49%
Ss_test014	4.23 mm	13%	100%
Ss_test015	2.66 mm	6%	100%
Ss_test016	5.66 mm	3%	74%
Ss_test017	8.46 mm	2%	66%
Ss_test018	16.00 mm	2%	92%
Ss_test019	47.16 mm	1%	4%
Ss_test020	56.55 mm	1%	4%
Ss_test021	78.66 mm	1%	5%
Ss_test022	16.29 mm	2%	95%
Ss_test023	10.94 mm	3%	49%

Ss_test001 - 22 Station(s) with Points in Common -

Object Name	Cloud-to-Cloud Error	Coincident Points (%)	Confidence (%)
Ss_test000	1.45 mm	68%	100%
Ss_test002	0.89 mm	79%	100%
Ss_test003	0.94 mm	82%	100%
Ss_test004	1.36 mm	77%	100%
Ss_test005	1.71 mm	58%	100%
Ss_test006	2.42 mm	61%	100%
Ss_test007	2.07 mm	62%	100%
Ss_test008	2.17 mm	67%	100%
Ss_test009	3.07 mm	66%	100%
Ss_test010	2.96 mm	62%	100%
Ss_test011	1.77 mm	16%	100%
Ss_test012	3.01 mm	7%	89%
Ss_test014	2.00 mm	15%	100%
Ss_test015	1.75 mm	7%	100%
Ss_test016	5.91 mm	5%	88%
Ss_test017	11.62 mm	4%	100%
Ss_test018	19.89 mm	3%	100%
Ss_test019	54.62 mm	2%	11%
Ss_test020	66.64 mm	2%	11%
Ss_test021	81.67 mm	3%	15%
Ss_test022	18.93 mm	4%	83%
Ss_test023	11.05 mm	4%	100%

Ss_test002 - 22 Station(s) with Points in Common -

Object Name	Cloud-to-Cloud Error	Coincident Points (%)	Confidence (%)
Ss_test000	1.41 mm	65%	100%
Ss_test001	0.89 mm	79%	100%
Ss_test003	0.71 mm	84%	100%
Ss_test004	0.96 mm	84%	100%
Ss_test005	1.34 mm	61%	100%
Ss_test006	1.67 mm	67%	100%
Ss_test007	1.52 mm	67%	100%
Ss_test008	1.87 mm	74%	100%
Ss_test009	2.47 mm	74%	100%
Ss_test010	2.68 mm	71%	100%
Ss_test011	2.02 mm	18%	100%
Ss_test012	2.64 mm	6%	53%
Ss_test014	1.84 mm	16%	100%
Ss_test015	1.52 mm	7%	100%
Ss_test016	2.34 mm	4%	95%
Ss_test017	2.65 mm	2%	100%
Ss_test018	5.48 mm	2%	86%
Ss_test019	51.67 mm	1%	3%
Ss_test020	53.05 mm	1%	3%
Ss_test021	113.31 mm	1%	5%
Ss_test022	7.35 mm	2%	49%
Ss_test023	7.37 mm	3%	62%

Ss_test003 - 22 Station(s) with Points in Common -

Object Name	Cloud-to-Cloud Error	Coincident Points (%)	Confidence (%)
Ss_test000	1.63 mm	64%	100%
Ss_test001	0.94 mm	82%	100%
Ss_test002	0.71 mm	84%	100%
Ss_test004	0.99 mm	87%	100%
Ss_test005	1.08 mm	64%	100%
Ss_test006	1.65 mm	68%	100%
Ss_test007	1.64 mm	68%	100%
Ss_test008	1.71 mm	76%	100%
Ss_test009	2.40 mm	75%	100%
Ss_test010	2.23 mm	72%	100%
Ss_test011	1.16 mm	18%	100%
Ss_test012	1.74 mm	6%	85%
Ss_test014	1.72 mm	19%	100%
Ss_test015	1.24 mm	8%	100%
Ss_test016	1.87 mm	5%	100%
Ss_test017	2.04 mm	4%	100%
Ss_test018	3.37 mm	3%	100%
Ss_test019	52.56 mm	1%	3%
Ss_test020	53.93 mm	1%	3%
Ss_test021	99.82 mm	1%	6%
Ss_test022	4.62 mm	2%	96%
Ss_test023	3.85 mm	3%	100%

Ss_test004 - 22 Station(s) with Points in Common -

Object Name	Cloud-to-Cloud Error	Coincident Points (%)	Confidence (%)
Ss_test000	1.48 mm	66%	100%
Ss_test001	1.36 mm	77%	100%
Ss_test002	0.96 mm	84%	100%
Ss_test003	0.99 mm	87%	100%
Ss_test005	0.95 mm	66%	100%
Ss_test006	1.21 mm	72%	100%
Ss_test007	1.00 mm	72%	100%
Ss_test008	1.34 mm	79%	100%
Ss_test009	1.77 mm	79%	100%
Ss_test010	2.06 mm	76%	100%
Ss_test011	1.44 mm	21%	100%
Ss_test012	1.93 mm	6%	100%
Ss_test014	1.63 mm	27%	100%
Ss_test015	1.20 mm	12%	100%
Ss_test016	2.12 mm	8%	100%
Ss_test017	2.26 mm	5%	100%
Ss_test018	4.00 mm	4%	100%
Ss_test019	65.68 mm	0%	2%
Ss_test020	52.21 mm	1%	4%
Ss_test021	100.60 mm	1%	6%
Ss_test022	6.35 mm	2%	100%
Ss_test023	5.86 mm	3%	100%

Ss_test005 - 22 Station(s) with Points in Common -

Object Name	Cloud-to-Cloud Error	Coincident Points (%)	Confidence (%)
Ss_test000	2.25 mm	48%	100%
Ss_test001	1.71 mm	58%	100%
Ss_test002	1.34 mm	61%	100%
Ss_test003	1.08 mm	64%	100%
Ss_test004	0.95 mm	66%	100%
Ss_test006	1.13 mm	69%	100%
Ss_test007	1.05 mm	69%	100%
Ss_test008	1.03 mm	66%	100%
Ss_test009	1.49 mm	61%	100%
Ss_test010	1.43 mm	59%	100%
Ss_test011	1.02 mm	19%	100%
Ss_test012	1.08 mm	6%	41%
Ss_test014	1.42 mm	63%	100%
Ss_test015	1.13 mm	43%	100%
Ss_test016	2.29 mm	32%	100%
Ss_test017	2.50 mm	23%	100%
Ss_test018	4.29 mm	15%	100%
Ss_test019	7.68 mm	4%	100%
Ss_test020	13.28 mm	3%	100%
Ss_test021	84.36 mm	2%	9%
Ss_test022	3.58 mm	2%	34%
Ss_test023	4.15 mm	3%	81%

Ss_test006 - 22 Station(s) with Points in Common -

Object Name	Cloud-to-Cloud Error	Coincident Points (%)	Confidence (%)
Ss_test000	2.86 mm	56%	100%
Ss_test001	2.42 mm	61%	100%
Ss_test002	1.67 mm	67%	100%
Ss_test003	1.65 mm	68%	100%
Ss_test004	1.21 mm	72%	100%
Ss_test005	1.13 mm	69%	100%
Ss_test007	0.51 mm	99%	100%
Ss_test008	1.18 mm	75%	100%
Ss_test009	1.29 mm	72%	100%
Ss_test010	1.45 mm	67%	100%
Ss_test011	1.57 mm	22%	100%
Ss_test012	2.41 mm	7%	53%
Ss_test014	1.67 mm	34%	100%
Ss_test015	1.14 mm	17%	100%
Ss_test016	2.94 mm	10%	100%
Ss_test017	3.37 mm	6%	100%
Ss_test018	4.96 mm	5%	100%
Ss_test019	55.35 mm	1%	3%
Ss_test020	60.57 mm	1%	6%
Ss_test021	59.73 mm	1%	6%
Ss_test022	5.20 mm	2%	14%
Ss_test023	4.58 mm	4%	26%

Ss_test007 - 22 Station(s) with Points in Common -

Object Name	Cloud-to-Cloud Error	Coincident Points (%)	Confidence (%)
Ss_test000	2.64 mm	57%	100%
Ss_test001	2.07 mm	62%	100%
Ss_test002	1.52 mm	67%	100%
Ss_test003	1.64 mm	68%	100%
Ss_test004	1.00 mm	72%	100%
Ss_test005	1.05 mm	69%	100%
Ss_test006	0.51 mm	99%	100%
Ss_test008	0.75 mm	75%	100%
Ss_test009	0.95 mm	73%	100%
Ss_test010	1.19 mm	68%	100%
Ss_test011	1.32 mm	22%	100%
Ss_test012	1.38 mm	7%	100%
Ss_test014	1.36 mm	34%	100%
Ss_test015	0.98 mm	17%	100%
Ss_test016	1.72 mm	10%	100%
Ss_test017	2.07 mm	6%	100%
Ss_test018	3.75 mm	5%	100%
Ss_test019	54.07 mm	0%	2%
Ss_test020	66.03 mm	1%	4%
Ss_test021	48.42 mm	1%	6%
Ss_test022	5.38 mm	2%	39%
Ss_test023	4.62 mm	4%	100%

Ss_test008 - 22 Station(s) with Points in Common -

Object Name	Cloud-to-Cloud Error	Coincident Points (%)	Confidence (%)
Ss_test000	3.48 mm	63%	100%
Ss_test001	2.17 mm	67%	100%
Ss_test002	1.87 mm	74%	100%
Ss_test003	1.71 mm	76%	100%
Ss_test004	1.34 mm	79%	100%
Ss_test005	1.03 mm	66%	100%
Ss_test006	1.18 mm	75%	100%
Ss_test007	0.75 mm	75%	100%
Ss_test009	0.81 mm	84%	100%
Ss_test010	0.88 mm	84%	100%
Ss_test011	1.04 mm	36%	100%
Ss_test012	1.21 mm	10%	100%
Ss_test014	1.42 mm	23%	100%
Ss_test015	1.01 mm	11%	100%
Ss_test016	1.51 mm	7%	100%
Ss_test017	1.67 mm	5%	100%
Ss_test018	3.06 mm	4%	100%
Ss_test019	57.93 mm	1%	3%
Ss_test020	56.26 mm	1%	4%
Ss_test021	77.49 mm	1%	6%
Ss_test022	3.43 mm	4%	91%
Ss_test023	2.81 mm	6%	100%

Ss_test009 - 22 Station(s) with Points in Common -

Object Name	Cloud-to-Cloud Error	Coincident Points (%)	Confidence (%)
Ss_test000	4.41 mm	63%	100%
Ss_test001	3.07 mm	66%	100%
Ss_test002	2.47 mm	74%	100%
Ss_test003	2.40 mm	75%	100%
Ss_test004	1.77 mm	79%	100%
Ss_test005	1.49 mm	61%	100%
Ss_test006	1.29 mm	72%	100%
Ss_test007	0.95 mm	73%	100%
Ss_test008	0.81 mm	84%	100%
Ss_test010	0.70 mm	85%	100%
Ss_test011	1.07 mm	41%	100%
Ss_test012	1.03 mm	14%	100%
Ss_test014	1.50 mm	16%	100%
Ss_test015	2.60 mm	7%	100%
Ss_test016	1.84 mm	4%	84%
Ss_test017	3.19 mm	3%	100%
Ss_test018	7.31 mm	3%	99%
Ss_test019	44.90 mm	1%	5%
Ss_test020	9.06 mm	1%	100%
Ss_test021	6.08 mm	2%	100%
Ss_test022	3.49 mm	4%	100%
Ss_test023	3.42 mm	8%	100%

Ss_test010 - 22 Station(s) with Points in Common -

Object Name	Cloud-to-Cloud Error	Coincident Points (%)	Confidence (%)
Ss_test000	4.72 mm	58%	100%
Ss_test001	2.96 mm	62%	100%
Ss_test002	2.68 mm	71%	100%
Ss_test003	2.23 mm	72%	100%
Ss_test004	2.06 mm	76%	100%
Ss_test005	1.43 mm	59%	100%
Ss_test006	1.45 mm	67%	100%
Ss_test007	1.19 mm	68%	100%
Ss_test008	0.88 mm	84%	100%
Ss_test009	0.70 mm	85%	100%
Ss_test011	0.87 mm	45%	100%
Ss_test012	1.20 mm	16%	100%
Ss_test014	1.24 mm	15%	100%
Ss_test015	2.41 mm	6%	100%
Ss_test016	1.73 mm	4%	73%
Ss_test017	3.52 mm	3%	100%
Ss_test018	9.16 mm	3%	100%
Ss_test019	45.45 mm	1%	6%
Ss_test020	23.24 mm	3%	100%
Ss_test021	16.24 mm	3%	100%
Ss_test022	3.75 mm	6%	100%
Ss_test023	4.16 mm	10%	100%

Ss_test011 - 22 Station(s) with Points in Common -

Object Name	Cloud-to-Cloud Error	Coincident Points (%)	Confidence (%)
Ss_test000	4.87 mm	18%	100%
Ss_test001	1.77 mm	16%	100%
Ss_test002	2.02 mm	18%	100%
Ss_test003	1.16 mm	18%	100%
Ss_test004	1.44 mm	21%	100%
Ss_test005	1.02 mm	19%	100%
Ss_test006	1.57 mm	22%	100%
Ss_test007	1.32 mm	22%	100%
Ss_test008	1.04 mm	36%	100%
Ss_test009	1.07 mm	41%	100%
Ss_test010	0.87 mm	45%	100%
Ss_test012	1.37 mm	55%	100%
Ss_test014	85.52 mm	1%	3%
Ss_test015	82.22 mm	1%	4%
Ss_test016	55.70 mm	0%	2%
Ss_test017	88.20 mm	1%	6%
Ss_test018	21.87 mm	3%	100%
Ss_test019	87.39 mm	2%	9%
Ss_test020	4.41 mm	15%	100%
Ss_test021	4.61 mm	21%	100%
Ss_test022	5.01 mm	33%	100%
Ss_test023	4.03 mm	37%	100%

Ss_test012 - 22 Station(s) with Points in Common -

Object Name	Cloud-to-Cloud Error	Coincident Points (%)	Confidence (%)
Ss_test000	5.72 mm	5%	49%
Ss_test001	3.01 mm	7%	89%
Ss_test002	2.64 mm	6%	53%
Ss_test003	1.74 mm	6%	85%
Ss_test004	1.93 mm	6%	100%
Ss_test005	1.08 mm	6%	41%
Ss_test006	2.41 mm	7%	53%
Ss_test007	1.38 mm	7%	100%
Ss_test008	1.21 mm	10%	100%
Ss_test009	1.03 mm	14%	100%
Ss_test010	1.20 mm	16%	100%
Ss_test011	1.37 mm	55%	100%
Ss_test014	86.02 mm	0%	2%
Ss_test015	74.00 mm	2%	9%
Ss_test016	61.60 mm	3%	13%
Ss_test017	71.67 mm	3%	17%
Ss_test018	13.38 mm	6%	40%
Ss_test019	59.11 mm	4%	8%
Ss_test020	2.87 mm	26%	100%
Ss_test021	2.29 mm	49%	100%
Ss_test022	2.40 mm	67%	100%
Ss_test023	2.09 mm	72%	100%

Ss_test014 - 22 Station(s) with Points in Common -

Object Name	Cloud-to-Cloud Error	Coincident Points (%)	Confidence (%)
Ss_test000	4.23 mm	13%	100%
Ss_test001	2.00 mm	15%	100%
Ss_test002	1.84 mm	16%	100%
Ss_test003	1.72 mm	19%	100%
Ss_test004	1.63 mm	27%	100%
Ss_test005	1.42 mm	63%	100%
Ss_test006	1.67 mm	34%	100%
Ss_test007	1.36 mm	34%	100%
Ss_test008	1.42 mm	23%	100%
Ss_test009	1.50 mm	16%	100%
Ss_test010	1.24 mm	15%	100%
Ss_test011	85.52 mm	1%	3%
Ss_test012	86.02 mm	0%	2%
Ss_test015	1.35 mm	58%	100%
Ss_test016	1.90 mm	44%	100%
Ss_test017	3.27 mm	31%	100%
Ss_test018	5.57 mm	18%	100%
Ss_test019	11.99 mm	6%	100%
Ss_test020	16.72 mm	5%	100%
Ss_test021	91.46 mm	3%	13%
Ss_test022	73.98 mm	1%	4%
Ss_test023	69.34 mm	1%	5%

Ss_test015 - 22 Station(s) with Points in Common -

Object Name	Cloud-to-Cloud Error	Coincident Points (%)	Confidence (%)
Ss_test000	2.66 mm	6%	100%
Ss_test001	1.75 mm	7%	100%
Ss_test002	1.52 mm	7%	100%
Ss_test003	1.24 mm	8%	100%
Ss_test004	1.20 mm	12%	100%
Ss_test005	1.13 mm	43%	100%
Ss_test006	1.14 mm	17%	100%
Ss_test007	0.98 mm	17%	100%
Ss_test008	1.01 mm	11%	100%
Ss_test009	2.60 mm	7%	100%
Ss_test010	2.41 mm	6%	100%
Ss_test011	82.22 mm	1%	4%
Ss_test012	74.00 mm	2%	9%
Ss_test014	1.35 mm	58%	100%
Ss_test016	1.06 mm	74%	100%
Ss_test017	1.73 mm	50%	100%
Ss_test018	3.95 mm	19%	100%
Ss_test019	4.64 mm	8%	100%
Ss_test020	22.98 mm	9%	100%
Ss_test021	51.98 mm	6%	32%
Ss_test022	48.87 mm	5%	27%
Ss_test023	47.00 mm	5%	26%

Ss_test016 - 22 Station(s) with Points in Common -

Object Name	Cloud-to-Cloud Error	Coincident Points (%)	Confidence (%)
Ss_test000	5.66 mm	3%	74%
Ss_test001	5.91 mm	5%	88%
Ss_test002	2.34 mm	4%	95%
Ss_test003	1.87 mm	5%	100%
Ss_test004	2.12 mm	8%	100%
Ss_test005	2.29 mm	32%	100%
Ss_test006	2.94 mm	10%	100%
Ss_test007	1.72 mm	10%	100%
Ss_test008	1.51 mm	7%	100%
Ss_test009	1.84 mm	4%	84%
Ss_test010	1.73 mm	4%	73%
Ss_test011	55.70 mm	0%	2%
Ss_test012	61.60 mm	3%	13%
Ss_test014	1.90 mm	44%	100%
Ss_test015	1.06 mm	74%	100%
Ss_test017	0.97 mm	57%	100%
Ss_test018	2.15 mm	21%	100%
Ss_test019	2.74 mm	12%	100%
Ss_test020	6.55 mm	10%	100%
Ss_test021	26.80 mm	4%	100%
Ss_test022	62.56 mm	4%	18%
Ss_test023	60.58 mm	3%	17%

Ss_test017 - 22 Station(s) with Points in Common -

Object Name	Cloud-to-Cloud Error	Coincident Points (%)	Confidence (%)
Ss_test000	8.46 mm	2%	66%
Ss_test001	11.62 mm	4%	100%
Ss_test002	2.65 mm	2%	100%
Ss_test003	2.04 mm	4%	100%
Ss_test004	2.26 mm	5%	100%
Ss_test005	2.50 mm	23%	100%
Ss_test006	3.37 mm	6%	100%
Ss_test007	2.07 mm	6%	100%
Ss_test008	1.67 mm	5%	100%
Ss_test009	3.19 mm	3%	100%
Ss_test010	3.52 mm	3%	100%
Ss_test011	88.20 mm	1%	6%
Ss_test012	71.67 mm	3%	17%
Ss_test014	3.27 mm	31%	100%
Ss_test015	1.73 mm	50%	100%
Ss_test016	0.97 mm	57%	100%
Ss_test018	1.13 mm	63%	100%
Ss_test019	1.45 mm	53%	100%
Ss_test020	1.27 mm	44%	100%
Ss_test021	3.45 mm	12%	100%
Ss_test022	14.79 mm	5%	100%
Ss_test023	10.46 mm	5%	100%

Ss_test018 - 22 Station(s) with Points in Common -

Object Name	Cloud-to-Cloud Error	Coincident Points (%)	Confidence (%)
Ss_test000	16.00 mm	2%	92%
Ss_test001	19.89 mm	3%	100%
Ss_test002	5.48 mm	2%	86%
Ss_test003	3.37 mm	3%	100%
Ss_test004	4.00 mm	4%	100%
Ss_test005	4.29 mm	15%	100%
Ss_test006	4.96 mm	5%	100%
Ss_test007	3.75 mm	5%	100%
Ss_test008	3.06 mm	4%	100%
Ss_test009	7.31 mm	3%	99%
Ss_test010	9.16 mm	3%	100%
Ss_test011	21.87 mm	3%	100%
Ss_test012	13.38 mm	6%	40%
Ss_test014	5.57 mm	18%	100%
Ss_test015	3.95 mm	19%	100%
Ss_test016	2.15 mm	21%	100%
Ss_test017	1.13 mm	63%	100%
Ss_test019	1.13 mm	75%	100%
Ss_test020	1.41 mm	61%	100%
Ss_test021	3.16 mm	16%	100%
Ss_test022	5.18 mm	7%	100%
Ss_test023	4.56 mm	8%	100%

Ss_test019 - 22 Station(s) with Points in Common -

Object Name	Cloud-to-Cloud Error	Coincident Points (%)	Confidence (%)
Ss_test000	47.16 mm	1%	4%
Ss_test001	54.62 mm	2%	11%
Ss_test002	51.67 mm	1%	3%
Ss_test003	52.56 mm	1%	3%
Ss_test004	65.68 mm	0%	2%
Ss_test005	7.68 mm	4%	100%
Ss_test006	55.35 mm	1%	3%
Ss_test007	54.07 mm	0%	2%
Ss_test008	57.93 mm	1%	3%
Ss_test009	44.90 mm	1%	5%
Ss_test010	45.45 mm	1%	6%
Ss_test011	87.39 mm	2%	9%
Ss_test012	59.11 mm	4%	8%
Ss_test014	11.99 mm	6%	100%
Ss_test015	4.64 mm	8%	100%
Ss_test016	2.74 mm	12%	100%
Ss_test017	1.45 mm	53%	100%
Ss_test018	1.13 mm	75%	100%
Ss_test020	1.91 mm	56%	100%
Ss_test021	3.79 mm	14%	100%
Ss_test022	10.30 mm	7%	100%
Ss_test023	9.66 mm	6%	100%

Ss_test020 - 22 Station(s) with Points in Common -

Object Name	Cloud-to-Cloud Error	Coincident Points (%)	Confidence (%)
Ss_test000	56.55 mm	1%	4%
Ss_test001	66.64 mm	2%	11%
Ss_test002	53.05 mm	1%	3%
Ss_test003	53.93 mm	1%	3%
Ss_test004	52.21 mm	1%	4%
Ss_test005	13.28 mm	3%	100%
Ss_test006	60.57 mm	1%	6%
Ss_test007	66.03 mm	1%	4%
Ss_test008	56.26 mm	1%	4%
Ss_test009	9.06 mm	1%	100%
Ss_test010	23.24 mm	3%	100%
Ss_test011	4.41 mm	15%	100%
Ss_test012	2.87 mm	26%	100%
Ss_test014	16.72 mm	5%	100%
Ss_test015	22.98 mm	9%	100%
Ss_test016	6.55 mm	10%	100%
Ss_test017	1.27 mm	44%	100%
Ss_test018	1.41 mm	61%	100%
Ss_test019	1.91 mm	56%	100%
Ss_test021	1.20 mm	44%	100%
Ss_test022	1.50 mm	30%	100%
Ss_test023	1.65 mm	31%	100%

Ss_test021 - 22 Station(s) with Points in Common -

Object Name	Cloud-to-Cloud Error	Coincident Points (%)	Confidence (%)
Ss_test000	78.66 mm	1%	5%
Ss_test001	81.67 mm	3%	15%
Ss_test002	113.31 mm	1%	5%
Ss_test003	99.82 mm	1%	6%
Ss_test004	100.60 mm	1%	6%
Ss_test005	84.36 mm	2%	9%
Ss_test006	59.73 mm	1%	6%
Ss_test007	48.42 mm	1%	6%
Ss_test008	77.49 mm	1%	6%
Ss_test009	6.08 mm	2%	100%
Ss_test010	16.24 mm	3%	100%
Ss_test011	4.61 mm	21%	100%
Ss_test012	2.29 mm	49%	100%
Ss_test014	91.46 mm	3%	13%
Ss_test015	51.98 mm	6%	32%
Ss_test016	26.80 mm	4%	100%
Ss_test017	3.45 mm	12%	100%
Ss_test018	3.16 mm	16%	100%
Ss_test019	3.79 mm	14%	100%
Ss_test020	1.20 mm	44%	100%
Ss_test022	1.04 mm	65%	100%
Ss_test023	1.35 mm	63%	100%

Ss_test022 - 22 Station(s) with Points in Common -

Object Name	Cloud-to-Cloud Error	Coincident Points (%)	Confidence (%)
Ss_test000	16.29 mm	2%	95%
Ss_test001	18.93 mm	4%	83%
Ss_test002	7.35 mm	2%	49%
Ss_test003	4.62 mm	2%	96%
Ss_test004	6.35 mm	2%	100%
Ss_test005	3.58 mm	2%	34%
Ss_test006	5.20 mm	2%	14%
Ss_test007	5.38 mm	2%	39%
Ss_test008	3.43 mm	4%	91%
Ss_test009	3.49 mm	4%	100%
Ss_test010	3.75 mm	6%	100%
Ss_test011	5.01 mm	33%	100%
Ss_test012	2.40 mm	67%	100%
Ss_test014	73.98 mm	1%	4%
Ss_test015	48.87 mm	5%	27%
Ss_test016	62.56 mm	4%	18%
Ss_test017	14.79 mm	5%	100%
Ss_test018	5.18 mm	7%	100%
Ss_test019	10.30 mm	7%	100%
Ss_test020	1.50 mm	30%	100%
Ss_test021	1.04 mm	65%	100%
Ss_test023	0.83 mm	80%	100%

Ss_test023 - 22 Station(s) with Points in Common -

Object Name	Cloud-to-Cloud Error	Coincident Points (%)	Confidence (%)
Ss_test000	10.94 mm	3%	49%
Ss_test001	11.05 mm	4%	100%
Ss_test002	7.37 mm	3%	62%
Ss_test003	3.85 mm	3%	100%
Ss_test004	5.86 mm	3%	100%
Ss_test005	4.15 mm	3%	81%
Ss_test006	4.58 mm	4%	26%
Ss_test007	4.62 mm	4%	100%
Ss_test008	2.81 mm	6%	100%
Ss_test009	3.42 mm	8%	100%
Ss_test010	4.16 mm	10%	100%
Ss_test011	4.03 mm	37%	100%
Ss_test012	2.09 mm	72%	100%
Ss_test014	69.34 mm	1%	5%
Ss_test015	47.00 mm	5%	26%
Ss_test016	60.58 mm	3%	17%
Ss_test017	10.46 mm	5%	100%
Ss_test018	4.56 mm	8%	100%
Ss_test019	9.66 mm	6%	100%
Ss_test020	1.65 mm	31%	100%
Ss_test021	1.35 mm	63%	100%
Ss_test022	0.83 mm	80%	100%

Appendix B

TRIMBLE TX5 SCANNER

PERFORMANCE

Ranging Unit

Unambiguity interval 153.49m (503.58ft)
Range[1] . . . . . 0.6 m–120 m indoor or outdoor with low ambient light and normal incidence to a 90% reflective surface
Measurement speed . . . 122,000 / 244,000 / 488,000 / 976,000 points/sec
Ranging error[2] . . . . . ±2 mm at 10 m and 25 m, each at 90% and 10% reflectivity

Ranging noise[3]	@10 m	@10 m noise compressed[4]	@25 m	@25 m noise compressed[4]
@ 90% reflectivity	0.6 mm	0.3 mm	0.95 mm	0.5 mm
@ 10% reflectivity	1.2 mm	0.6 mm	2.20 mm	1.1 mm

Color Unit

Resolution . . . . . Up to 70 megapixel color
Dynamic color feature . . . . . Automatic adaption of brightness

Deflection unit

Field of view (vertical/horizontal) . . . . . 300° / 360°
Step size (vertical/horizontal . . . . . 0.009° (40,960 3D pixels on 360°) / 0.009° (40,960 3D pixels on 360°)
Max. vertical scan speed . . . . . 5,820rpm or 97Hz

Laser (Optical transmitter)

Laser class 3R
Laser power (cw Ø) 20mW
Wavelength 905nm
Beam divergence . . . . . Typical 0.19mrad (0.011°)
Beam diameter at exit . . . . . 3.0mm, circular

Data handling and control

Data storage . . . . . SD, SDHC™, SDXC™; 32 GB card included
Scanner control . . . . . Via touch-screen display
WiFi (WLAN) access . . . . . Remote control, Scan visualization and download are possible on mobile devices with Flash®

Multi-Sensor

Dual axis compensator . . . . . Levels each scan with an accuracy of 0.015° and a range of ±5°
Height sensor . . . . . Detects the height relative to a fixed point via an electronic barometer and adds it to the scan
Compass . . . . . Electronic compass gives the scan an orientation. A calibration feature is included.

HARDWARE SPECIFICATIONS

Power supply voltage . . . . . 19 V (external supply), 14.4 V (internal battery)
Power consumption . . . . . 40 W and 80 W respectively (while battery charges)
Battery life . . . . . Up to 5 hours
Ambient temperature . . . . . 5 °C to 40 °C (41 °F to 104 °F)
Humidity . . . . . Non-condensing
Cable connector . . . . . Located in scanner mount
Weight 5.0kg
Size . . . . . 240 mm x 200 mm x 100 mm (9.5 in x 8 in x 4 in)

1 Depends on ambient light, which can act as a source of noise. Bright ambient light (e.g.; sunshine) may shorten the actual range of the scanner to lesser distances. In low ambient light, the range can be more than 120 m for normal incidence on high-reflective surfaces.
2 Ranging error is defined as the maximum error in the distance measured by the scanner from its origin point to a point on a planar target.
3 Ranging noise is defined as a standard deviation of values about the best-fit plane.
4 A noise-compression algorithm may be activated to average points in sets of 4 or 16, thereby compressing raw data noise by a factor of 2 or 4.

Figure B.1. Trimble TX5 instrument specification sheet.

DATASHEET

Trimble TX8 LASER SCANNER

PERFORMANCE

Overview

Scanning principle ..... Vertically rotating mirror on horizontally rotating base
Range principle ..... Ultra-high speed time-of-flight powered by Trimble Lightning technology
Scanning speed[7] ..... 1 million pts/sec
Maximum range ..... 120 m on most surfaces
340 m with optional upgrade
Range noise[5] ..... <2 mm on most surfaces with Standard scan modes
<1 mm with High Precision scan mode[2]

Range measurement

Laser class ..... 1, eye safe in accordance with IEC EN60825-1
Laser wavelength ..... 1.5 µm, invisible
Laser beam diameter ..... 6–10–34 mm @ 10–30–100m
Minimum range ..... 0.6 m
Max. standard range ..... 120 m on 18–90% reflectivity
100 m on very low reflectivity (5%)
Extended range[1] ..... 340 m
Range noise[5] ..... <2 mm from 2 m to 120 m on 18–90% reflectivity in Standard modes
<1 mm from 2 m to 80 m on 18–90% reflectivity in High Precision mode[2]
Range systematic error[5,6] ..... <2 mm

Scanning

Field of view ..... 360° x 317°
Angular accuracy[5] ..... 80 µrad

Scan Parameters	Preview	Level 1	Level 2	Level 3	Extended[1]
Max range	120 m	120 m	120 m	120 m	340 m
Scan duration (minutes)[3]	01:00	02:00	03:00	10:00	20:00
Point spacing at 10 m	15.1 mm	———	———	———	———
Point spacing at 30 m	———	22.6 mm	11.3 mm	5.7 mm	———
Point spacing at 300 m	———	———	———	———	75.4 mm
Number of points	8.7 Mpts	34 Mpts	138 Mpts	555 Mpts	312 Mpts

IMAGING

Integrated HDR camera ..... 10 megapixel resolution, full field of view
Image capture duration ..... 1 min for Standard, 2 min for HDR
External camera kits are available for higher resolution HDR images

OTHERS

Touchscreen display ..... TFT-LCD with 24-bit color
Size (mm) ..... 93 (H) x 55.8 (V), equivalent 4.3" diagonal
Resolution ..... 800 x 480 (WVGA)
Luminance resolution ..... 8 bits
Leveling ..... External bubble, onboard electronic bubble
Dual axis compensation ..... Selectable on/off
Resolution ..... 0.3"
Range ..... ±5'
Accuracy[6] ..... 1"
Data storage ..... USB 3.0 Flash Drive
Remote control ..... Operate with Trimble tablet or other mobile device via WLAN or with Windows 7 or higher PC or tablet via USB cable[4]

PHYSICAL

Dimensions ..... 335 mm W x 386 mm H x 242 mm D
(13.2 in W x 15.2 in H x 9.5 in D)
Weight ..... 10.7 kg (23.6 lb) with tribrach and no battery;
11.2 kg (24.7 lb) with tribrach and battery
Power supply ..... 76 mm W x 43 mm H x 130 mm D
(3.0 in W x 1.7 in H x 5.1 in D);
Weight: 0.66 kg (1.46 lb)
Battery dimensions ..... 89.2 mm W x 20.1 mm H x 149.1 mm D
(3.5 in W x 0.8 in H x 5.9 in D)
Battery weight ..... 0.46 kg (1 lb)
Power consumption ..... 72 W
Scan time per battery ..... >2 hours
Instrument case ..... 500 mm W x 366 mm H x 625 mm D
(19.7 in W x 14.4 in H x 24.6 in D)

ENVIRONMENTAL

Operating temperature range
(non-condensing atmosphere) ..... –0 °C to +40 °C (32 °F to 104 °F)
Storage temperature ..... –20 °C to +50 °C (–4 °F to 122 °F)
Operating humidity range ..... Non condensing
Lighting conditions ..... All indoor & outdoor conditions over entire range (no lighting limitations)
Protection class IP54

CLASS 1
LASER PRODUCT

1 Optional upgrade increases range from 120m to 340 m.
2 Scan duration time is longer with High Precision scan mode.
3 Scan duration times for Standard scan modes.
4 Wired remote control requires optional USB cable PN 23704034.
5 Specification given as 1 sigma.
6 At distance of 1.5 m to 100 m for albedo >20%.
7 Effective scan speed for optimum scan quality.

Specifications subject to change without notice.

Figure B.2. Trimble TX8 instrument specification sheet.

Appendix C

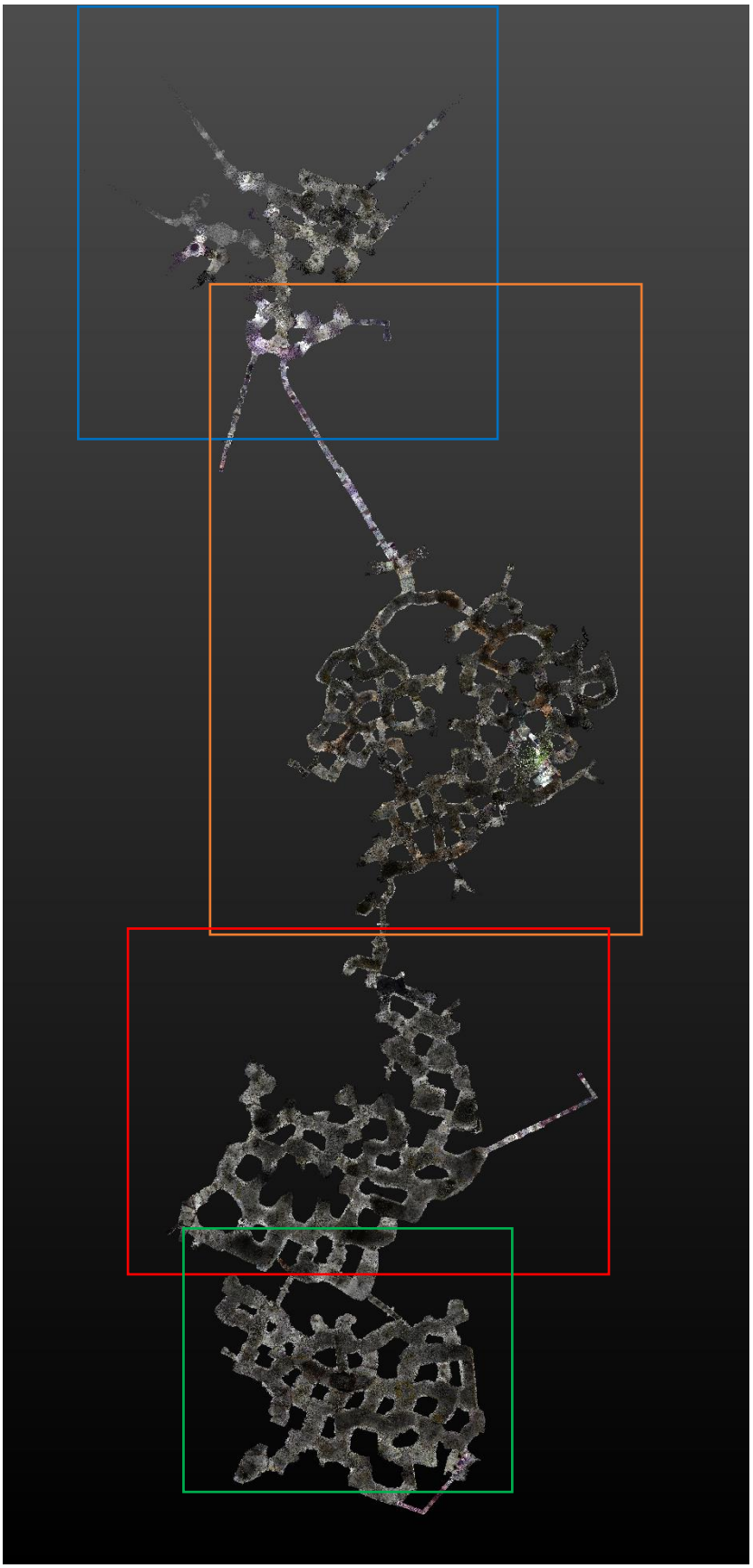

Figure C.1. Captured underground network. From top, Auckland, Wellington, Nelson, Blenheim.

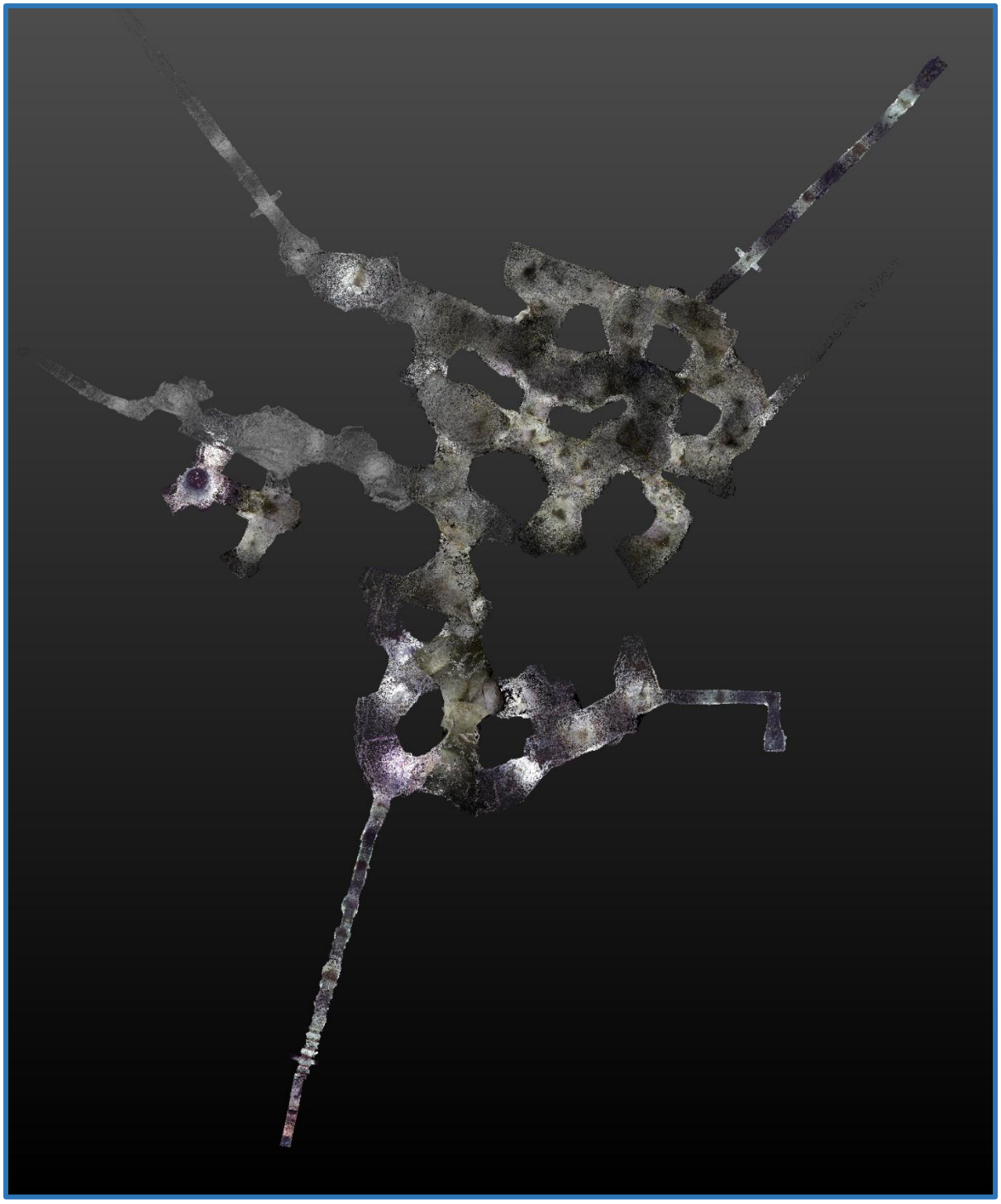

Figure C.2. Auckland Quarry, exported as a single las file.

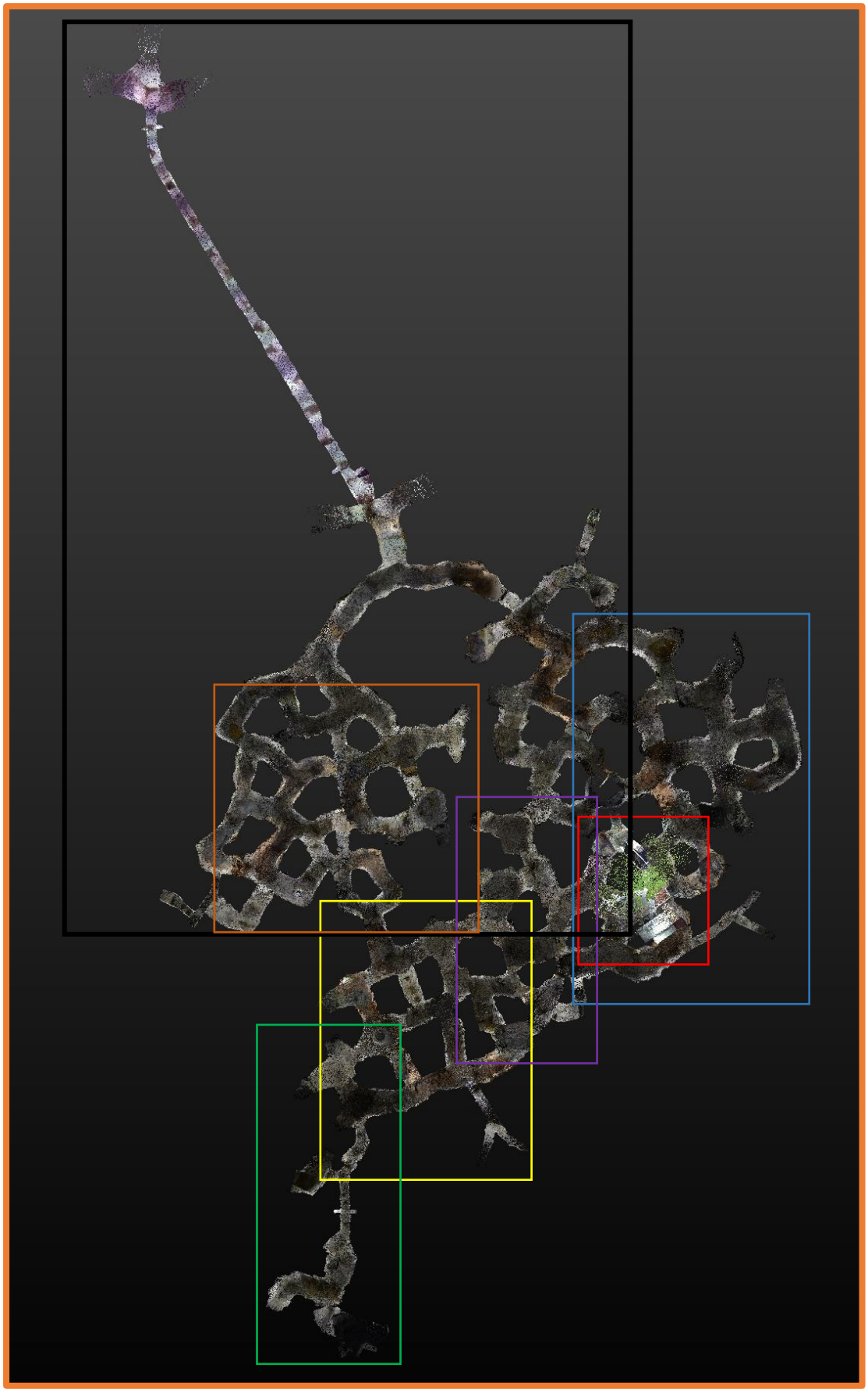

Figure C.3. Wellington Quarry showing each of the las file segments.

Wellington 1

Wellington 2

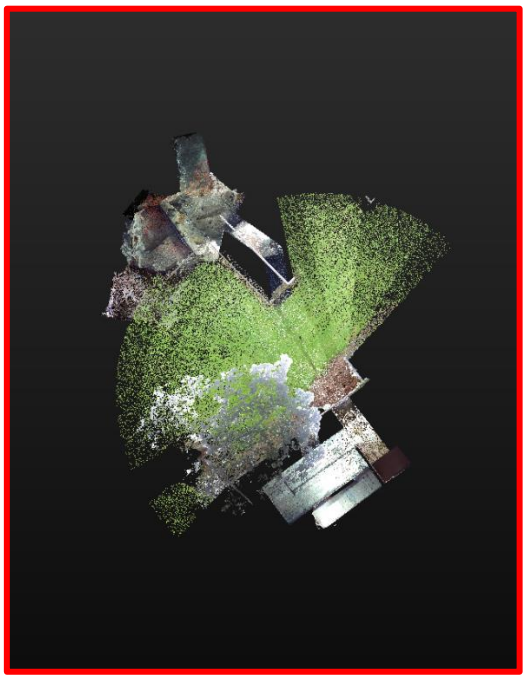

Wellington 3

Wellington 4

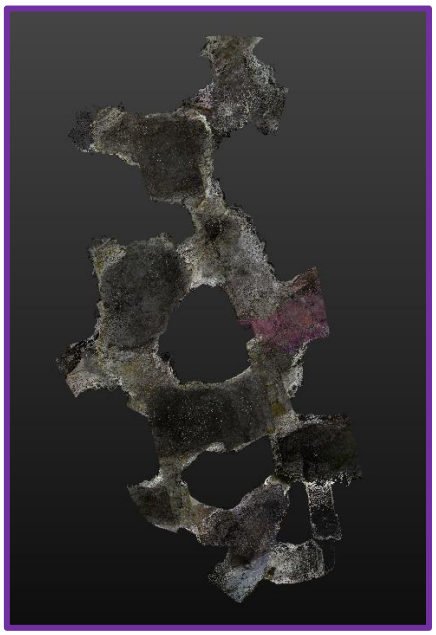

Figure C.4. Wellington Quarry 1-4 segmented las files.

Wellington 5

Wellington 7

Wellington 6

Figure C.5. Wellington Quarry 5-7 segmented las files.

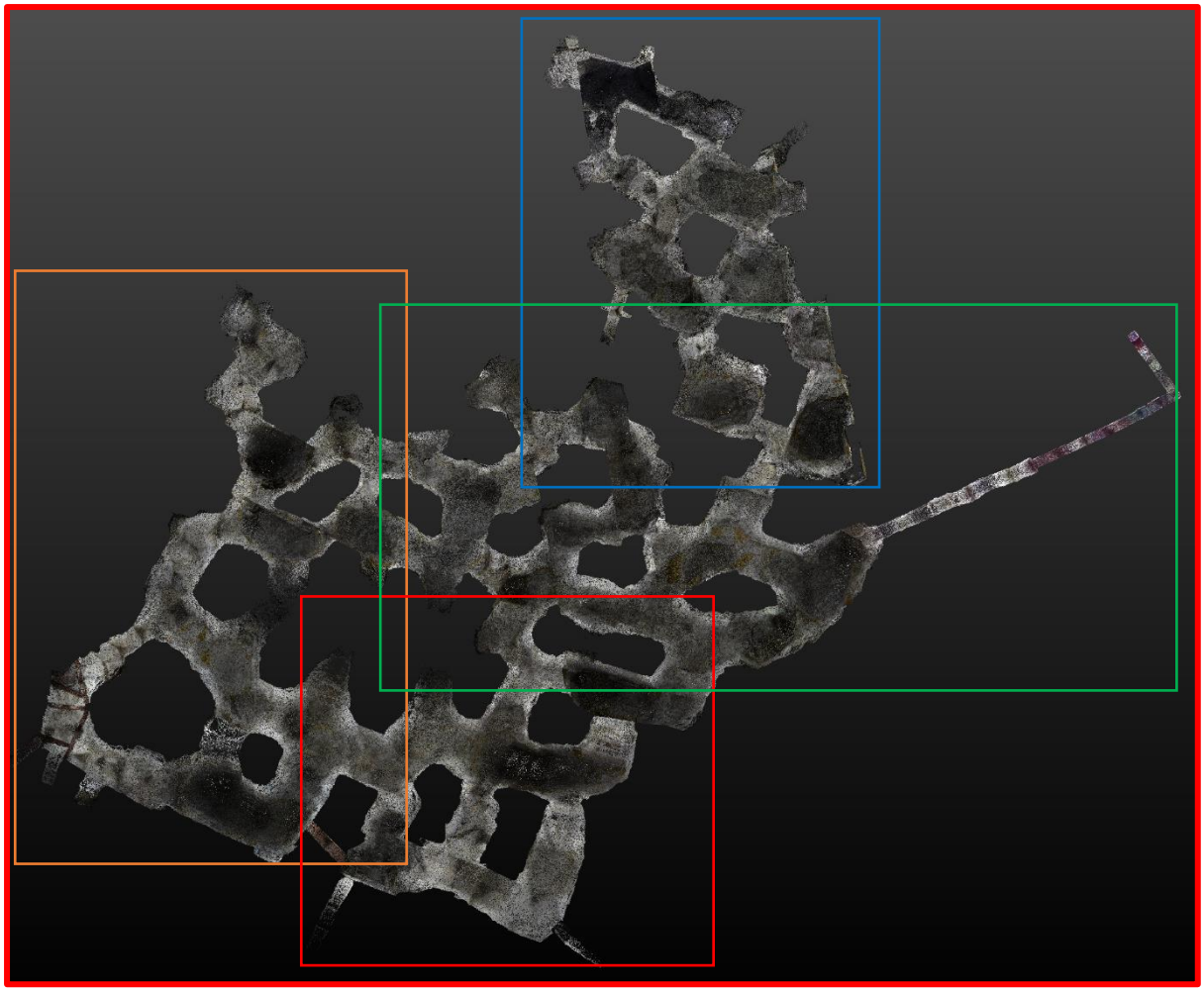

Figure C.6. Nelson Quarry showing each of the las file segments.

Nelson 1

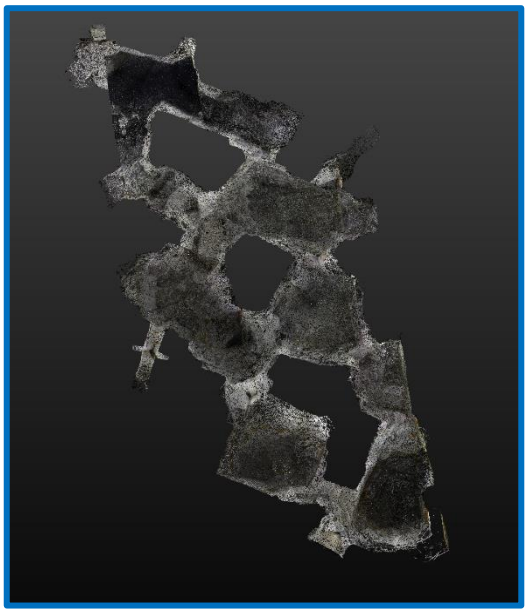

Nelson 2

Figure C.7. Nelson Quarry 1-2 segmented las files.

Nelson 3

Nelson 4

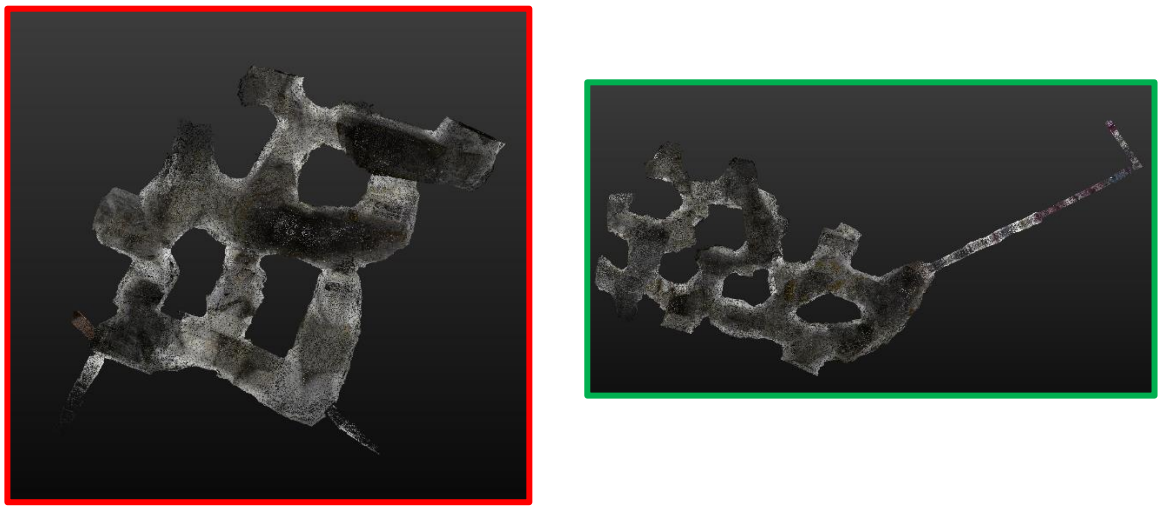

Figure C.8. Nelson Quarry 3-4 segmented las files.

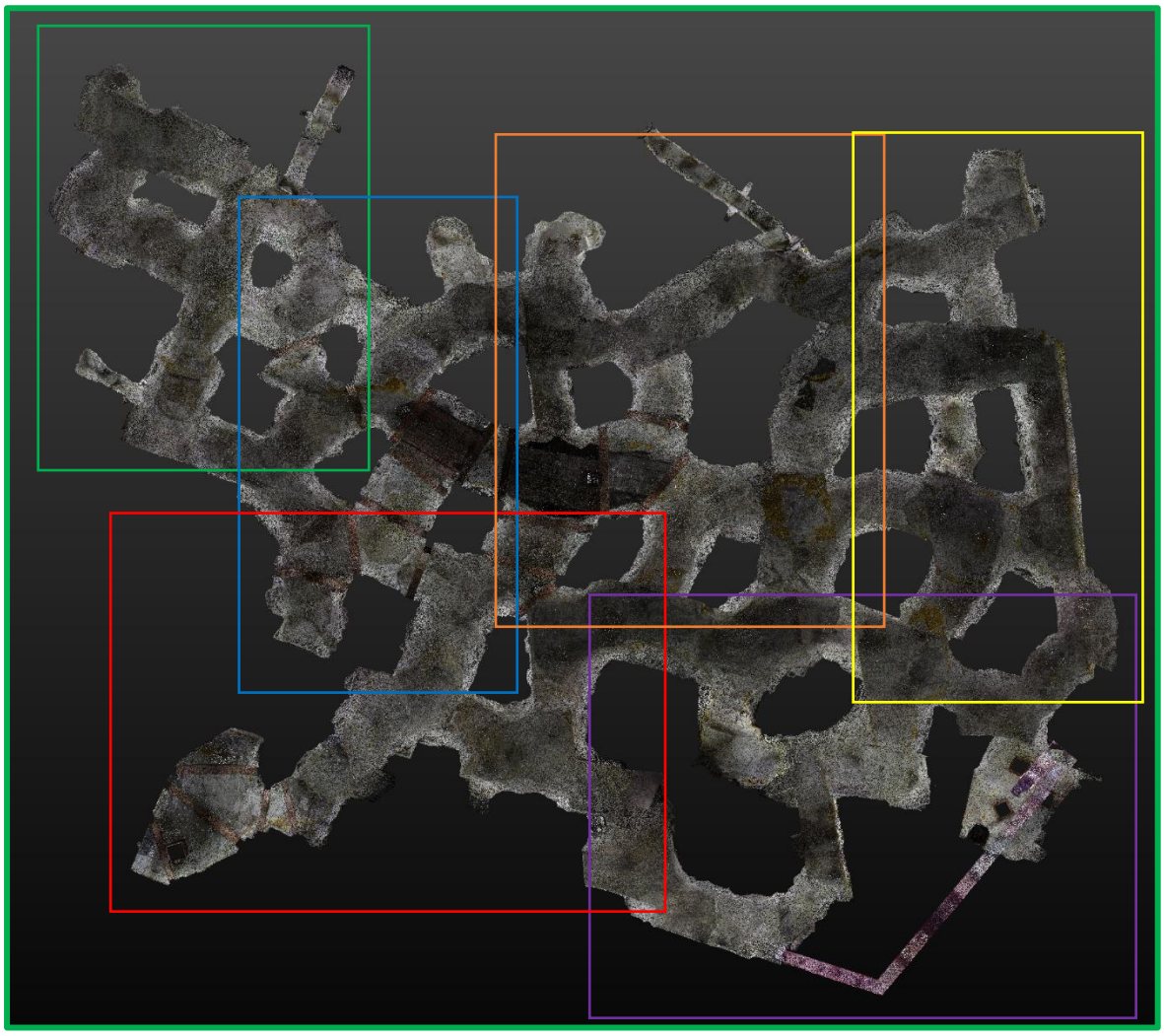

Figure C.9. Blenheim Quarry showing each of the las file segments.

Blenheim 1

Blenheim 2

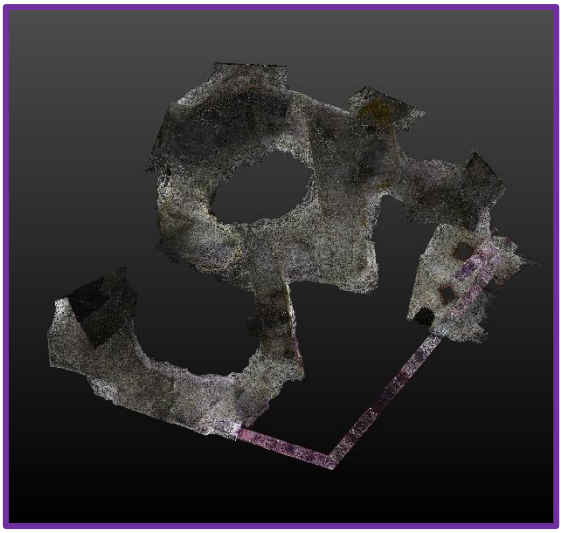

Blenheim 3

Blenheim 4

Figure C.10. Blenheim Quarry 1-4 segmented las files.

Blenheim 5

Blenheim 6

Figure C.11. Blenheim Quarry 5-6 segmented las files.

Figure C.12. Streetscape showing each of the las file segments.

Streetscape A

Streetscape B

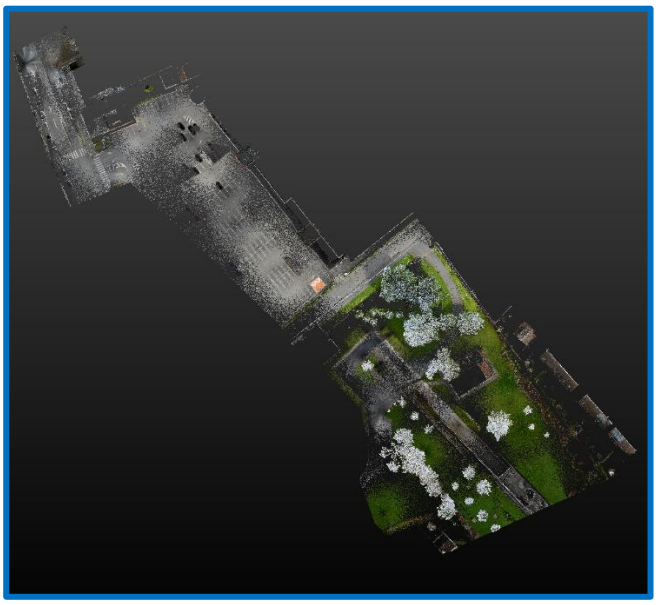

Museum

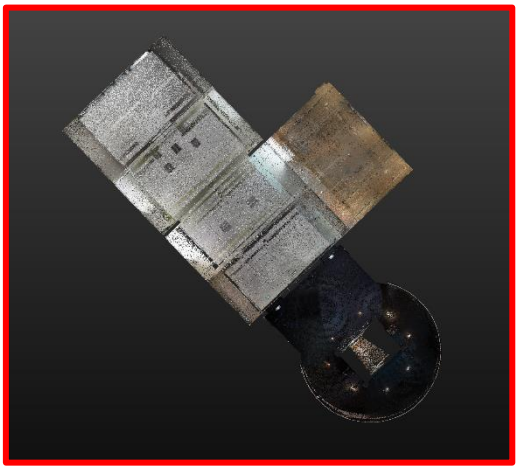

Figure C.13. Streetscape A and B, and Museum segmented las files.